Stethoscope Design for Auscultation in High Noise Environments

A DISSERTATION
SUBMITTED TO THE FACULTY OF
UNIVERSITY OF MINNESOTA
BY

Garrett Nelson

IN PARTIAL FULFILLMENT OF THE REQUIREMENTS
FOR THE DEGREE OF
DOCTOR OF PHILOSOPHY

Rajesh Rajamani, Adviser
Arthur Erdman, Co-Adviser

October, 2015

Acknowledgements

I chose to pursue my doctorate in order improve my understanding and nurture my passion for engineering. This experience has been a privilege, awarding me the opportunity to learn from the wisdom of professors and fellow students alike. As I enter the workforce, I am grateful for their guidance and the positive influence they have had on both my professional and personal life.

Above all others, I am grateful to my advisor, Dr. Rajesh Rajamani, for his commitment to my graduate education and development as a researcher. He maintained a steadfast commitment to my research and offered invaluable guidance, support, and enthusiasm throughout the entire five years of my program. I am proud to have had the opportunity to work with him and follow in the footsteps of the many great researchers he has helped lead through his research lab.

I would additionally like to express my gratitude towards Dr. Arthur Erdman who has served as my co-advisor over the years. With his years of experience in the field and knowledge in the area of design, he has helped broaden my understanding of engineering and ensure the success of my dissertation.

When I entered graduate school and began the pursuit of my doctorate, Lee Alexander provided the support and technical assistance necessary to give my project a running start. He has since served as a valuable resource for guidance on my research and has assisted with many fabrication needs. I owe him many thanks for his help along the way.

Throughout the course of my degree, I have had the privilege to work with a wide range of graduate students who have come before me and those who currently on their path to a graduate education. To those who graduated before me: Dr. Gridsada Phanomchoeng, Dr. Peng Peng, Dr. Shan Hu, Dr. Saber Taghvaeeyan, and Dr. Kalpesh Signal, I thank you for providing positive role models as I entered the program and for helping me learn what it means to be a researcher. Your support, both academically and personally, played a large role in helping me push my project and education forward. To those who I precede in

graduation: Mahdi Ahmadi, Song Zhang, Ye Zhang, Ryan Madson, Woongsun Jeon, and Corey Cruttenden, you too have helped immensely over the years. Similarly, I would like to thank Dr. Yan Wang for his guidance in the last year of my degree. It has been a pleasure to work alongside each and every one of you, and I hope that I have been able to provide the same positive influence on your lives as you have mine.

A portion of my work has been funded by the Department of the Army and 3M's Infection Prevention Division. I owe a special thanks to personnel from both groups for making available the resources necessary to accomplish these research objectives. The U.S. Army Medical Research Acquisition Activity, 820 Chandler Street, Fort Detrick, MD 21702-5014 is the awarding and administering acquisition office. This investigation was partially funded under a U.S. Army Medical Research Acquisition Activity; Cooperative Agreement W81XWH-10-1-1051. The content of the information herein does not necessarily reflect the position or the policy of the U.S. Government, the U.S. Army, or 3M, and no official endorsement should be inferred.

Lastly, I would like to thank my family and friends who have supported me throughout each and every stage of my degree. Providing me with a positive environment outside of school has helped ensure my success within school, and I am grateful for you all.

Abstract

The low signal-to-noise ratio encountered during auscultation in many high noise environments can impede a physician's successful examination and diagnosis of a patient's health. This thesis develops a vibro-acoustic model for an electronic stethoscope and investigates a number of techniques to improve the signal-to-noise ratio. The techniques explored are:

1. Redesign of stethoscope components for improved vibration isolation
2. Use of dual piezoelectric transducers and dynamic model inversion for elimination of physician handling noise
3. Implementation of active noise cancellation using either a reference microphone or a reference accelerometer

In a digital stethoscope, a piezoelectric transducer is used to convert chest sounds into electrical signals. Due to the larger chestpiece size needed to accommodate the electronics of a digital stethoscope, noise due to physician handling of the device is often greater. To characterize the effects of the device's construction on its sensitivity to handling disturbances, a theoretical stethoscope model is developed. The vibro-acoustic model relates force inputs acting on the body of the stethoscope to voltage signals created by its piezo-ceramic transducer.

Using the theoretical model, simulations are conducted to demonstrate that traditional vibration isolation applied between the chestpiece and the transducer results in poor coupling—loss in sensitivity—between the transducer and the patient's chest. By using a floating transducer housing, equally effective vibration isolation can be accomplished with far less loss in sensitivity to patient signals. The proposed isolation design was experimentally evaluated by redesigning the stethoscope's components. However, limitations in the damping and stiffness values of available isolation materials resulted in some loss of sensitivity over a narrow frequency range.

Next, as a superior alternative to physically isolating the stethoscope transducer from external disturbances a signal processing based approach to compensate for handling noise is developed. It is possible to use a redundant sensor and novel input estimation techniques to digitally remove the undesired noise measurement components. By adding a second piezo to the stethoscope assembly, it is shown that an inverse dynamic mapping can be used to relate the measured signals to original directional inputs acting on the stethoscope. An output feedback observer is developed to account for the unknown initial state of the system dynamics. In simulation, it is shown that the effects of the unknown and undesired disturbance input can be removed over the entire frequency range critical for auscultation. In physical experiments, the feasibility of the dual-piezo stethoscope approach to estimate and remove these disturbances is also demonstrated.

In many patient transport environments, the ambient noise can routinely exceed 75 dB with the most severe environments having noise sources more than 3000 times louder than a typical auscultation signal. For noise from the patient side of the stethoscope, passive isolation methods cannot be used as they will impede transmission of the desired chest sounds to the transducer. Based on helicopter field data acquired with an electronic stethoscope retrofitted with an array of microphones and accelerometers, it is demonstrated that primary noise corruption during auscultation in a helicopter can be attributed to vehicle vibrations. Using this information, it is shown that a reference accelerometer can be used in place of a conventional reference microphone to estimate the noise corruption. Using either the LMS or NLMS active noise cancellation algorithms, it is possible to extract the desired auscultation signal. This is confirmed experimentally by simulating the internal cabin noise levels of the harshest noise environment in which injured military personnel are routinely examined—a mobile Black Hawk helicopter.

Table of Contents

List of Tables

List of Figures

Citations of Published Work

Some portions of this thesis have appeared in the following publications:

1. G. Nelson, R. Rajamani, and A.G. Erdman, "Modeling, analysis, and vibration reduction in an electronic stethoscope," *Proceedings of the ASME 2014 Dynamic Systems and Control Conference*, San Antonio, 2014.
2. G. Nelson, R. Rajamani, and A.G. Erdman, "Noise control challenges for auscultation on medical evacuation helicopters," *Applied Acoustics*, vol. 80, no, 80, pp. 68-78, 2014.
3. G. Nelson, R. Rajamani, and A.G. Erdman, "Vibro-acoustic model of a piezoelectric-based stethoscope for chest sound measurements," *Measurement Science and Technology*, vol. 26, no. 9, pp. 095701, 2015.

CHAPTER 1:

INTRODUCTION

1.1 MOTIVATION

Auscultation refers generally to the practice of listening to sounds emanating from the body. Since the advent of the stethoscope in 1816 [1], it has quickly risen to obtain status as the ubiquitous sign of a doctor. This is due largely to the clinical relevance and versatility of the stethoscope as a diagnostic tool for preliminary patient assessment and triage.

Despite advances in stethoscope technology, auscultation is still not possible in many emergency medicine environments. This is due to the presence of high levels of ambient noise which can mask the clinical signals of interest. This problem is particularly severe when attempting to auscultate during patient transport in both ground and air vehicles.

By understanding the characteristics of these unwanted additive signals, it is possible to improve the design of stethoscope to mitigate the effects of noise and successfully enable auscultation in these harsh environments.

1.1.1 *Auscultation*

In a standard clinical setting, the stethoscope is routinely used for examination of a patient's cardiovascular, respiratory, and gastrointestinal systems.

During auscultation of the cardiovascular system, the stethoscope diaphragm is placed on the patient's chest over various positions of the heart while a clinician observes the cardiac rate and rhythm. A trained physician can use this method to detect both heart murmurs and gallop rhythms.

Similarly, for auscultation of the lung, the stethoscope is placed on an array of positions on both the posterior and anterior chest adjacent to the main lobes of the lung. In addition

to the traditional cadence of a healthy breath sound caused by air moving through the respiratory system, a physician is looking for pathological chest sounds such as wheezes, crackles, and stridor which are noted by their pitch and continuity. A brief introduction to the specific characteristics of these chest sounds and their analysis is provided by Dalmay and Reichert [2, 3].

A time recording of clean heart and lung sounds in a healthy patient can be seen in Figure 1-1 and Figure 1-2 respectively.

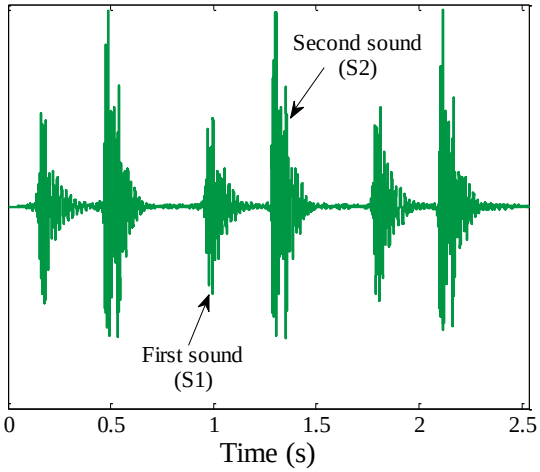

Figure 1-1: Normal and unsplit first and second heart sounds

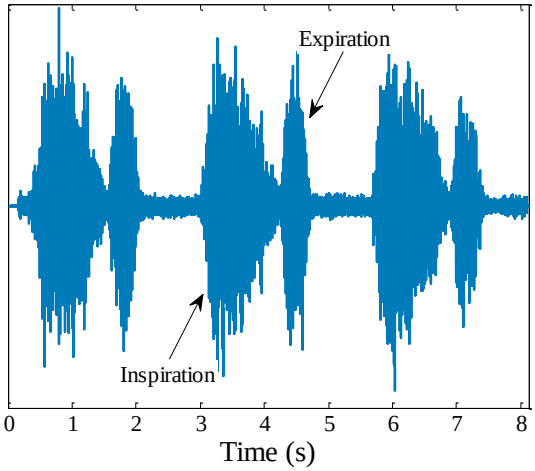

Figure 1-2: Normal vesicular lung sounds

There are many physiological factors which can affect the transmission of auscultation signals prior to reaching the stethoscope [4, 5]. However, there has been considerable research conducted to evaluate the standard spectral properties of both heart and lung sounds as they would appear at the surface of the body. In one of the earliest of such studies, Gavriely found that typical breath sounds contain frequency content between .5-1 kHz [6]. In future work, he has refined these results to indicate that inspiration and expiration lung sounds contain frequency components between 736-999 Hz and 426-796 Hz respectively [7]. In similar work conducted for the evaluation of heart sounds, Arnott has reported that heart sounds in healthy subjects are concentrated below 150 Hz [8]. Other investigations have focused on the frequency content of many cardiac irregularities. These reports suggest that many abnormal heart sounds may contain frequency components as high as 1000Hz [9]. A summary of the frequency content of healthy and abnormal chest sounds is provided in Figure 1-3.

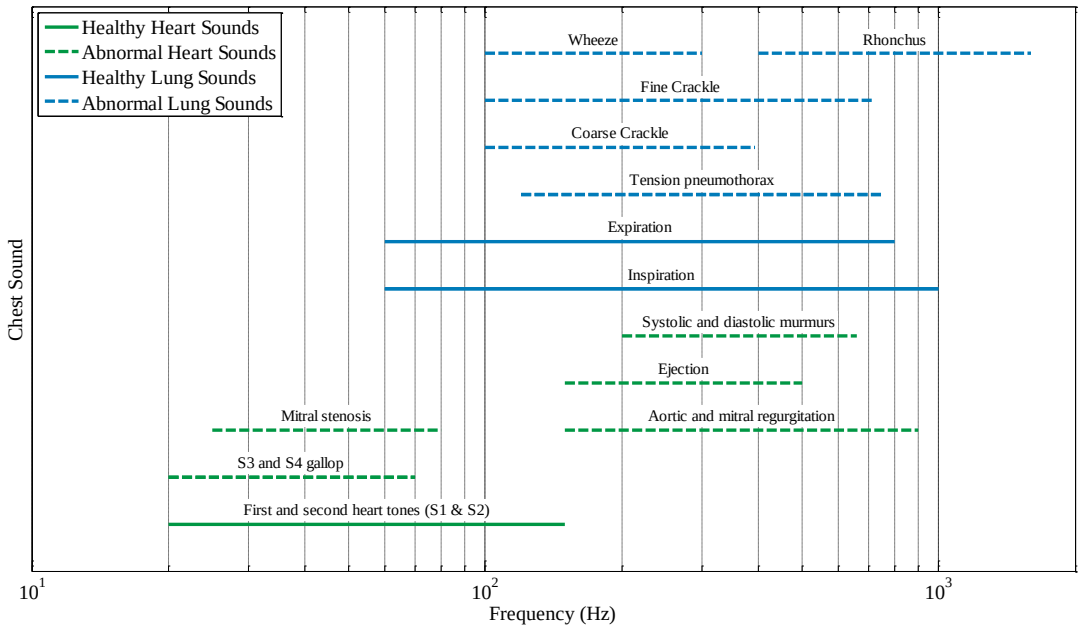

Figure 1-3: Frequency content of healthy and abnormal chest sounds [3, 7, 8, 9, 10, 11, 12]

To enable successful auscultation, the stethoscope's primary function is to amplify sounds emanating from the body. Normal chest sounds typically vary between 22-30 dB at the skins surface [13]. After amplification through the stethoscope, these sounds are amplified to 60-75 dB at which point they are audible to the user. In their modern form, stethoscopes come in both mechanical and electronic versions. Although their construction may differ, all stethoscopes generally consist of three primary components: (1) the chestpiece, (2) the tubing, and (3) the binaurals (see Figure 1-4). Based on factors such as construction, geometry, and material selection, each of these components can have a distinct effect on the quality of sound transmitted to the user [14, 15].

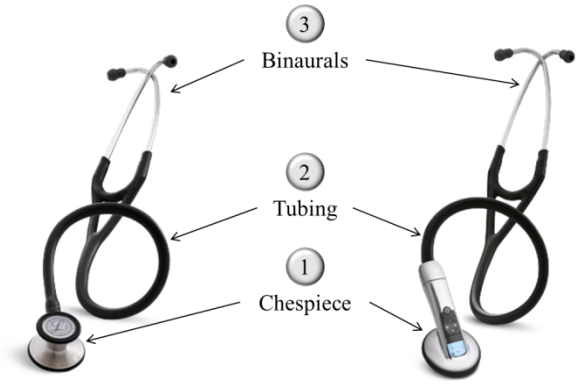

Figure 1-4: Primary components of a modern stethoscope

The chestpiece is the main component of the stethoscope which is placed on a patient during examination. It is responsible for acquiring the desired auscultation signal generated by small pressure waves at the skin's surface. The resulting sound is transferred to the user (i.e. physician) through the tubing and subsequently delivered by way of the stethoscope binaurals which are placed in the user's ears.

The chestpiece of a mechanical stethoscope contains one or two small air cavities which are used to transmit the desired sound to the user. Depending on the application or design, the cavity may be covered by a small tightly stretched diaphragm which vibrates as a result of the chest signal. Other designs feature an open cavity which relies on direct vibrations of the patient's skin acting as the diaphragm. For both configurations, the

pressure change caused in the air cavity by this motion is what creates the sound observed by the user. The characteristics of the relayed sound are affected by the both the shape and volume of the air cavity. A large diameter and short cavity with a diaphragm will generally transmit higher frequency signals. Conversely, a small deep cavity will better transmit lower frequency sounds. Some types of stethoscopes will have both a diaphragm (high frequency, short cavity) and a bell (low frequency, deep cavity) side to allow a physician to selectively listen to different chest sounds depending on which side of the device is used.

In an electronic stethoscope, the direct transmission of acoustic waves through stethoscope chestpiece is replaced by a sensor and speaker. Traditionally, the sensor is either a small microphone or piezoceramic disc which can detect the vibrations at the skins surface. For some microphone based stethoscopes, a diaphragm and closed air cavity is still employed to provide the required pressure differential which is measured by the sensor. The conversion of an acoustic signal to an analog measurement enables further modification to a sound before it is presented to the user. Many commercially available electronic stethoscope models allow the selection of different filter modes which can limit the frequency range of the sound played to the user. In this way, the electronic stethoscope can provide a similar level of versatility as a conventional two-sided (bell and diaphragm) mechanical stethoscope. After acquiring and possibly filtering the signal, the sound is transmitted to the user with a small speaker placed either at the base of the tubing or directly at the binaurals.

1.1.2 *Noise in Emergency Setting*

Due to its versatility in clinical diagnostics, the stethoscope is commonly used by medical practitioners in a wide variety of environments. In many of these settings, the presence of high levels of ambient environmental noise and operational noise caused during routine handling of the stethoscope has been found to interfere with successful auscultation. The potential noise sources can be broken into four main categories:

1. Ambient acoustics: Airborne noise leaking into the stethoscope chestpiece, tubing, or binaurals (e.g. people talking or loud equipment nearby)
2. Ambient vibrations: Structure borne noise traveling through the patient or physician and detected at the chestpiece (e.g. vibrations in a moving vehicle traveling on a rough road)
3. Physician noise: Noise due to handling of the stethoscope (e.g. rubbing caused by a physician's fingers moving on the chestpiece)
4. Patient contact noise: Noise due to relative motion between the stethoscope and the patient (e.g. friction caused by repositioning the stethoscope on a patient's chest)

Some of these noise sources are periodic or sudden in nature and can be avoided with improved training or control of the environment, but others may be more persistent and/or unavoidable. Each presents a unique challenge to auscultation and directly impacts the quality of diagnostics capable with either a mechanical or electronic stethoscope.

In many hospital emergency departments the ambient noise level can vary between 60-70dB. At this level, heart and lung sounds are still audible, but the detection of heart murmurs and other clinically relevant chest sound irregularities is not possible [16, 17]. With the elevated sound levels present during patient ground transport, one study has found that, even on a paved road with no sirens, lung sounds in a healthy subject were detected with only a 9.2% success rate [18]. Thus, in aeromedical transport environments, where noise levels are well in excess of 75 dB, it is obvious that there exists a clear challenge to successful auscultation.

Presented in Table 1-1 are the ambient noise levels in common emergency patient examination environments.

Table 1-1: Ambient noise levels in common emergency patient examination environments

Environment	Conditions	Ambient Noise Level (dB)
Hospital	Pediatric clinic examining room	75 [17]
	Surgical ward	65 [17]
	Emergency department	55.9-76.6 [19]
	Medical clinic examining room	55 [17]
Ambulance	In transit, with siren	93-100 [20]
	In transit, no siren	68 [21]
Helicopter	Civilian Medevac Bell 206L LongRanger	80-95 [22]
	Civilian Medevac MBB BK-17	93-97 [23]
	Army Medevac Sikorsky UH-60	104 [24]
	MBB BO-105	94.9-96.4 [25]
Plane	Bell Jet Ranger 206B	90-100 [26]
	Falcon 50	77 [27]
	C-130	80-100 [28]

In the quietest aeromedical transportation environment, the Falcon 50 Plane, the use of an electronic stethoscope was found to improve detection of heart sounds, but all clinically relevant details were barely audible [27]. Similar assessments of stethoscope performance in helicopters have demonstrated that auscultation of both lung and heart sounds was not possible [25, 29]. Working in a simulated high noise chamber, Cain has quantified the severity of the problem and determined that ambient noise levels in excess of 85dB and 75-80 dB respectively will prevent successful auscultation of heart and lung sounds [29].

In transportation environments, the ambient acoustic noise is often coupled with the presence of structurally transmitted noise [30]. These vibrations originate from mechanical components within the vehicle engine, or the rotor in the case of a helicopter. Additionally, during ground transport vibrations caused by the vehicle frame as it travels over rough road surfaces may be present. Irrespective of their origin, these vibrations can be transferred to the stethoscope by traveling through either the patient or the physician

and to the stethoscope. When traveling through the patient, they can appear as additive components generally indistinguishable from the clinically relevant chest signal.

In addition to ambient noise, successful auscultation can be impeded by operational noise caused by the user handling the stethoscope. This noise can be caused by finger/hand movement along the stethoscope chestpiece surface, accidental contact with the chestpiece, or muscle hand tremors. Generally, this noise is independent of the environment in which the device is used. However, the presence of large levels of vibration in a transportation environment may amplify the problem. For the case of hand tremors and accidental bumping of the device, the noise will appear as short bursts with large relative amplitude. Particularly, in an electronic stethoscope, the high sensitivity of the transducer causes a large amplification of these noise artifacts. Additionally, handling noise may appear due to rubbing on the chestpiece or other stethoscope components. Characteristic of the underlying mechanisms of friction, this noise will be broadband in nature.

1.2 EXISTING TECHNOLOGIES

A variety of approaches have been documented for addressing the different noise components which have been found to interfere with auscultation. The approaches can be generally divided into two main categories: those which try to minimize the energy of the noise before it is sensed by the stethoscope, and those which try to eliminate the noise with filtering or signal processing methods after it has already been picked up by the stethoscope. Depending on the severity of the noise source, the existing technologies have had varied success, but ultimately no complete design solution has been presented which can guarantee successful auscultation in the harshest environments.

1.1.1 *Spectral Filtering*

An initial approach to mitigate the ambient noise in high noise environments may be spectral band filtering. If the primary noise corruption exists in a frequency range other than that of the desired signal, it is possible to design a filter to remove any detected

signal components that lie in this range. This approach has been presented by Orton where a design is proposed which features a variable bandpass filter with an adjustable center frequency and bandwidth [31]. Recall that both heart and lung sounds contain frequency content up to 1 kHz. In lieu of this, for spectral band filtering to be successful in enabling auscultation in high noise environments, it is imperative that majority of ambient noise exists only at frequencies above 1 kHz. However, numerous reports have documented that this is not a valid assumption. Cain has found that considerable noise components in a UH-60 Sikorski helicopter exist in the sub-1000 Hz frequency range of interest. His analysis reveals that the ambient SPL is higher at the heart frequencies than the breath frequencies, but is sufficiently high to successfully mask the desired auscultation signal in both cases [29]. Similar results by Poulton in other helicopter environments indicate that simple electronic filtration of helicopter noise is impossible [30]. Therefore, all designs similar to that of Orton will be insufficient in these environments.

1.2.1 *Active Noise Cancellation*

The inability of simple spectral filtering to remove the unwanted noise components has led many authors to investigate the use of more advanced methods. One of such approaches is the application of Active Noise Cancellation (ANC). Initially proposed by Leug in 1934 for the mitigation of tonal noise in ducts, ANC has since been well documented in numerous applications [32, 33, 34, 35]. The classic noise cancellation structure commonly used today was presented by Widrow in 1975. His method relies on a Finite Impulse Response adaptive filter in a feedforward path to estimate the noise with a Least Mean Square (LMS) adaptive algorithm used to adjust the filter weights [36].

The first well documented application of ANC on a stethoscope to remove the effects of ambient noise was conducted by the US Army in 1993 [26]. For this study they attempted to detect heart and lung sounds in a Bell Jet Range 206B Helicopter using a dual stethoscope transducer design. A primary stethoscope transducer was placed at the auscultation site to obtain the desired signal, and a secondary transducer was placed

elsewhere on the patient's chest to obtain a high fidelity noise reference signal. Using the LMS algorithm they were able to achieve 30dB noise reduction between 20-100Hz and 10-20dB reduction between 100-300Hz in a simulated environment.

Using similar methods, future work conducted by Suzuki was able to extend the range of ambient noise reduction achieved by the LMS algorithm to 40-500Hz with 30dB noise reduction. His work was also performed in a simulated noise environment, but in place of ambient recordings he used white acoustic noise. His design additionally altered the dual transducer configuration to incorporate both the primary and reference sensor in a single device. One electret microphone is used to detect the primary patient signal and the other is directed towards the ambient environment to obtain a reference noise signal. Although his results need to be extended to achieve the necessary reduction at higher frequency ranges, he was the first to identify that a substantial portion of ambient acoustic noise is coupled through the patient's chest [37]. The specific level of noise coupled to the sensor in this manner has been estimated to be around 6.6 dB [38]. Therefore, in high noise environments passive shielding of the device will be ineffective.

In 1998, Fleeter and Patel both investigated ambient stethoscope noise reduction with LMS and NLMS algorithms in a simulated C-130 Aircraft environment [28, 39]. Using a stethoscope chestpiece with two omnidirectional electret microphones (shown in Figure 1) and the LMS algorithm, Patel achieved 15dB noise reduction between 100-600Hz. By switching to the NLMS algorithm, he demonstrated faster convergence and an additional 5dB reduction above 450Hz. Using a similar stethoscope design, Fleeter reported comparable noise reduction between 20-800Hz using the NLMS approach. In the last and most recent work on the subject, Belloni and colleagues were also able to demonstrate 15dB reduction with the LMS algorithm using dual electret microphones [40]. However, this research was limited to noisy office environments notably quieter than most transportation scenarios.

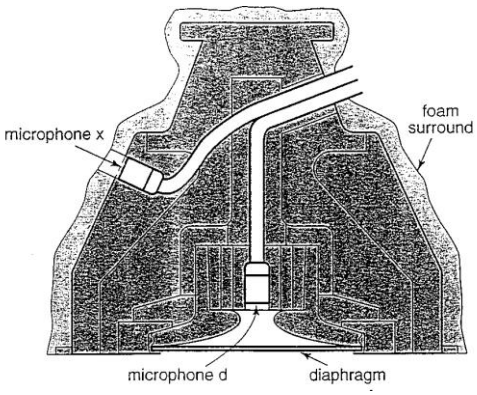

Figure 1-5: Dual microphone stethoscope chestpiece design [39]

Moving beyond basic LMS and NLMS approaches, Wang has proposed a time-shared blind identification process to improve ANC performance [41]. Using two microphones to obtain the primary and noise reference signals, his work leveraged the a priori knowledge of auscultation signal characteristics to improve filter convergence. He constrained adaptation of the filter to operate during estimated pauses in the desired signal. Subsequently, the updated filter was used for signal estimation until the next pause in the desired signal was detected. A similar method was demonstrated by Han for the case of breath sound extraction [42]. It has also been shown that noise reduction may be possible with nonlinear time scaling or fuzzy detection algorithms [43, 44]. Although these results demonstrate improved performance, they rely on a moderate to low ambient noise level to ensure accurate detection of signal cycles. This limitation is also present in the work of Chang, where a spectral subtraction method was used to minimize the effects of ambient noise sources [45].

All the aforementioned studies share the common element of Active Noise Cancellation based on a reference microphone signal. Although each was able to demonstrate considerable SNR improvements, their findings are limited by the use of a simulated acoustic noise environment. Research conducted by Poulton has demonstrated that ANC in a real transportation environment is hampered due to the significant presence of structurally transmitted noise [30]. This suggests that an alternative sensor capable of

detecting this noise could outperform a reference microphone and provide the additional noise reduction necessary to ensure successful auscultation. To date, very limited research has been conducted analyzing this hypothesis. A 2010 study by Pandia has investigated the use of a single chest-worn accelerometer to remove motion artifacts from heart sounds [46]. Using a Savitzky-Golay polynomial smoothing filter to estimate motion artifacts caused by healthy subjects walking at normal speed, heart sounds could be detected with 99.36% accuracy. However, this algorithm will likely suffer in the presence of high levels of broadband noise.

1.2.2 *Passive Isolation*

As a different characteristic type of noise, other methods can be employed to specifically address the effects of handling noise caused by the physician. Specifically, vibration isolation can be employed to dissipate the noise prior to reaching the stethoscope transducer. Although these techniques have been well understood in a wide variety of disciplines, their application to the improvement of stethoscopes' susceptibility to handling noise (or other noise traveling from the physician) has been limited.

An early design presented by Greenberger proposes the use of a flexible member between the primary chestpiece assembly and its shell to achieve handling noise isolation [47]. Although his design was intended for mechanical stethoscopes, the intent can be extended to those with an electronic sensing element. However, the suggested embodiment of the device appears to be effective in only a narrow frequency range. Bilan has developed a similar isolation strategy for use with an electronic stethoscope [48]. By using a floating mass and a flexible diaphragm to stabilize the sensing element, added isolation is achieved from both vibrational waves traveling from the physician as well as surface waves traveling along the patient's skin. The primary limitation of this design is the direct coupling path which exists for vibrational energy traveling from the physician, through the patient, and back into the sensing element. Although some isolation for noise traveling on this path is achieved by Cusson with his earlier design of a resonant chamber sound pick-up device, these effects were not well understood [49]. However, his design

did characterize a valuable alternate embodiment of vibration isolation. Using a floating mass similar to Bilan, he encapsulated the sensing element (microphone) in a high compliance foam shield to provide the desired isolation. This successfully absorbed mechanical vibrational energy as it attempted to pass through the device.

As a means to specifically address handling noise in the form of friction, a team at 3M proposed a stethoscope outer surface coated in a low friction material [50]. This approach may reduce the levels of frictional noise caused by handling, but will not mitigate physician noise in the form of sudden impacts. Additionally, this design does not address other known types of noise that may propagate through the physician.

1.3 THESIS CONTRIBUTIONS

This thesis focuses on the design and development of passive and active stethoscope technology to reduce the stethoscope's susceptibility to noise and enable successful auscultation in high noise environments. Major contributions of this dissertation include:

1. Development and validation of a theoretical electro-mechanical model of the stethoscope to better understand its sensing mechanisms and the transmission of noise.
2. Development and experimental validation of a vibration isolation design to dissipate mechanical vibrational energy from the physician prior to reaching the stethoscope transducer.
3. Derivation and implementation of a directional disturbance estimation algorithm which uses dual sensors to estimate and remove the effects of unwanted noise caused by the physician.
4. Development of an accelerometer based active noise cancellation system which can be used to remove ambient noise encountered during auscultation in transportation environments.

1.4 THESIS OUTLINE

Chapter 2 describes the development of a vibro-acoustic model for a piezo-ceramic based stethoscope. A theoretical multi-DOF rigid body vibration model consisting of discrete connected components is developed for the piezoelectric stethoscope. The model captures

the resulting internal dynamics caused by force inputs from either the patient or physician holding the device. Using a two-port lumped parameter model, the mechanical vibrations are related to a resulting electrical signal. The parameterized state-space model is experimentally validated and its parameters identified by using a thorax simulator and vibration shaker.

Chapter 3 develops a new design to isolate the stethoscope transducer from disturbances caused by the physician during routine handling of the device. Using the theoretical model, the benefits of different isolation methods are explored. It is shown that if isolation is introduced between the transducer housing and the rest of the stethoscope, the greatest vibration isolation can be achieved with minimal losses in patient sensitivity. Constructing the modified stethoscope design, experimental results are presented to study the influence of the proposed design changes and confirm the predicted model behavior.

Chapter 4 presents an alternate, digital method for reducing the effects of physician handling noise without resulting in a loss in device sensitivity to patient signals. The chapter develops a method by which an inverse dynamic model can be obtained to relate measured auscultation signals corrupted by noise to the original noise free signals. Two different dynamic observers are derived to produce the desired signal estimates from the measurement. With a combination of theoretical simulations and experimental results, the successful estimation and removal of an undesired external disturbance signal is demonstrated.

Chapter 5 discusses the use of accelerometer based active noise cancellation to remove the influence of high levels of ambient noise in emergency patient transportation environments. Data is presented from testing conducted in a U.S. Army Sikorsky UH-60 helicopter to demonstrate the existing challenges to auscultation in this environment. With a combination of simulations and experimental data it is shown that adaptive noise cancellation techniques using a reference accelerometer within the device or placed remotely in the vehicle would be significantly more effective at enabling auscultation than conventional microphone based systems.

CHAPTER 2:

STETHOSCOPE MODELING

2.1 MOTIVATION

This chapter focuses on the development of a theoretical model to study the influence of noise and vibration on chest sound measurements with a piezoelectric stethoscope. Two types of vibrations, namely inputs through the patient's chest and disturbances from the physician, influence the acoustic measurement. The goal of this work is to develop a model to understand the propagation of these vibrational noises through the stethoscope and to the piezoelectric sensing element.

A multi-DOF rigid body vibration model consisting of discrete connected components is developed for the piezoelectric stethoscope. Using a two-port lumped parameter model, the mechanical vibrations are related to the resulting electrical signal. The parameterized state-space model is experimentally validated and its parameters identified by using a thorax simulator and vibration shaker.

2.1.1 *3M™ Littmann® Electronic Stethoscope*

The 3M™ Littmann® Model 3200 Electronic Stethoscope is a recent advance in stethoscope technology (see Figure 2-1). At the heart of the design is a small flexible disc piezoceramic transducer. When placed on the skin of a patient, small pressure waves and vibrations caused by heart or lung sounds excite the piezo causing a proportional voltage signal. Subsequently, the signal is broadcast to the user via a small speaker at the base of the binaural tube. The stethoscope comes equipped with three different electronic filter modes to condition the signal prior to playing it for the user. These modes, each with a different frequency response, allow the user to select the type of sounds of interest.

Figure 2-1: 3M™ Littmann® Model 3200 electronic stethoscope [51]

Although the electronic stethoscope has many distinct advantages over its mechanical counterpart, it has some potential drawbacks. Its added sensitivity makes the device increasingly susceptible to unwanted background noise caused by both the ambient environment and routine handling of the device. The piezo is capable of picking up even the faintest sounds caused by any incidental rubbing or tapping along the main body of the device. Therefore, in emergency transportation environments, as vehicle vibrations are transmitted through the physician and patient and into the stethoscope, auscultation can become increasingly difficult.

The construction of the model 3200 electronic stethoscope is shown in Figure 2-2. The piezoceramic element, hereafter "piezo", is mounted in a light-weight aluminum transducer housing. Directly on either side of the piezo is a thin layer of foam. A small metal disc is placed on the front side of the piezo to both protect the sensing element and to allow a more even distribution of force. The housing is secured to a plastic ring, referred to as a "foot", which is subsequently attached to the primary chestpiece of the device. The transducer housing is attached to the foot by way of two small metal tabs press fit into the underside of the ring. An additional six tabs are used to stabilize the housing against the foot, although these tabs are not rigidly attached to the ring. The foot, with attached transducer housing assembly, is secured to the chestpiece using four small screws.

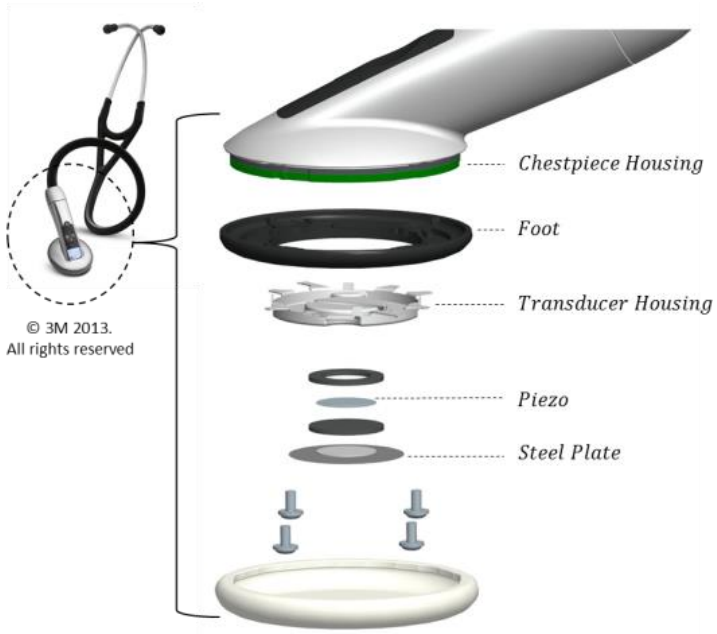

Figure 2-2: Electronic stethoscope assembly exploded view with internal components

The construction of the device results in a sturdy design. However, it is evident that the rigid connection of the transducer housing to the chestpiece provides a direct coupling path for noise caused by routine handling of the stethoscope. As a user makes contact with the outer surface of the chestpiece, the resulting vibrations travel through the device directly to the sensing element. Additionally, there is no isolation provided from unwanted noise traveling from the patient. As required to sense all the auscultation signals of interest, the sensing element is directly coupled to the patient's skin.

2.1.2 *Electronic Stethoscope Performance Characterization*

In order to better understand the mechanisms by which these disturbances are transmitted to the sensing element, the device performance can be examined when subjected to different noise sources. This was accomplished by studying the stethoscope's physical design and sensing mechanism. The mechanical transmission of noise to the piezo can be divided into two distinct paths, forward (patient side) and backward (physician side), $H_{p,p}$ and $H_{p,m}$ respectively. The sensitivity of the piezo to off-axis stimuli is generally small. Accordingly, all lateral transmission paths have been left out of this investigation.

Once the signal has been acquired, it undergoes digital signal processing and filtering. As different filter modes are selected, this filtering affects the system differently. Subsequently, this will be regarded as its own second independent subsystem, H_{f_k}, where $k = 1,2,3$ corresponds to the selected filter mode.

Lastly, the signal is output to the user via a speaker through the binaural tubing. Thus, this will be treated as the third and final subsystem, H_s. A block diagram showing the signal path from each noise source to the user is provided in Figure 2-3 below.

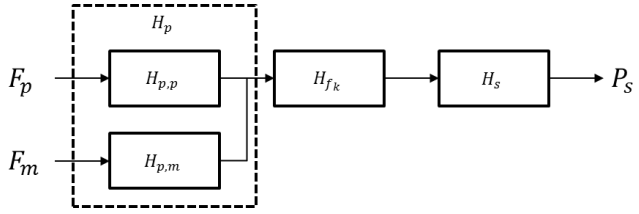

Figure 2-3: Electronic stethoscope system block diagram

By breaking the stethoscope into these subsystems, it is possible to understand how each individually affects the overall performance of the device. Also, as each subsystem operates independently of the others, analysis on each as a standalone system is both valid and advantageous.

As an initial investigation, it was possible to experimentally determine the frequency response of the two sensor transmission paths, $H_{p,p}$ and $H_{p,m}$. This was accomplished by stimulating the stethoscope with vibrational noise from both potential noise sources. Similar to the work done by other authors, in our test environment, the source of the vibrations was an electro-dynamic shaker system [52, 53]. The method by which the stethoscope was coupled to the shaker was varied depending on which noise source was being emulated. For the generation of patient noise, a thorax simulator was used to transmit vibrations from the shaker into the stethoscope. The thorax simulator was employed to more accurately capture the dynamic coupling caused by contact between the face of the stethoscope and the patient. In order to improve the accuracy and reproducibility of this method, multiple simulator ("phantom") designs have been

investigated by other authors. The simplest approach has been the use of a sound source coupled to the sensor with an air chamber [54, 55]. However, the most common of these methods illustrate the use of coupling materials that better mimic biological soft tissue. With this objective, proposed phantom designs have included sound sources embedded in viscoelastic materials [56, 57], water-filled polymer or latex bladders [58, 53], and electromagnetic speakers covered with viscoelastic layers [52].

Leveraging the work of these authors, our phantom has been constructed by covering a viscoelastic polymer mold with a thin flexible polymer membrane. Together, the layered approach of this phantom closely imitates the mechanical properties of a subject's skin and subcutaneous tissue.

When testing a stethoscope, the piezo sensor side of the device is placed on the surface of the thorax simulator (see Figure 2-4). The nominal application pressure was held constant by allowing the stethoscope to rest using its own weight as has been done by other authors [52]. Although less sturdy, this is closer to its actual usage condition and thus preferred over alternate test configurations in which the stethoscope has been firmly secured to the test apparatus [55]. In order to even further improve the clinical relevance of the method selected, additional tests were conducted with added weight to simulate the added pressure traditionally applied by a physician during auscultation. This is congruent with the methods proposed by Kraman [59], although here only a single 50g weight was selected.

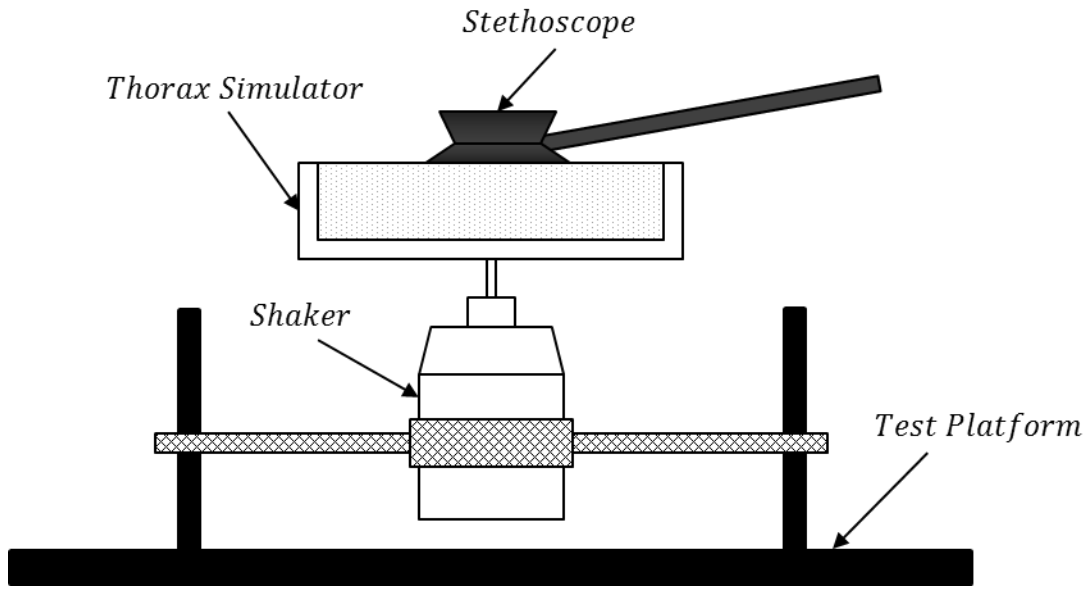

Figure 2-4: Frequency response test apparatus for simulating patient inputs

For all testing conducted, a compatible vibration exciter and force transducer were employed. Each has a bandwidth in excess of 7,500 Hz—well above the highest observed stethoscope system resonance. During each test, the coherence between the input and output signals was carefully monitored to ensure that no undesired resonance caused by the test apparatus was present and corrupting the data.

Providing zero-mean, unit variance, white Gaussian noise to the shaker, the frequency response, $G(f)$, of the stethoscope can be estimated. Specifically, this is obtained by taking the ratio of the output Power Spectral Density, $S_y(f)$, to the input Power Spectral Density, $S_u(f)$.

$$G(f) = \frac{S_y(f)}{S_u(f)} \tag{2.1}$$

In order to simplify analysis and isolate the desired mechanical subsystem, the stethoscope output was taken directly before the analog to digital converter contained on the stethoscope's onboard processor. Thus, the transfer function estimates correspond to only the forward and backward mechanical transmission paths without the addition of filtering in the stethoscope.

The secondary (backward) transmission path, $H_{p,m}$, can be tested using the same test apparatus. However, for this test the stethoscope is inverted and securely mounted above the shaker (see Figure 2-5). The inverted stethoscope is press fit into the specially designed stethoscope holder. By stimulating the system again with white noise, it is possible to obtain the frequency response of the stethoscope chestpiece for physician inputs.

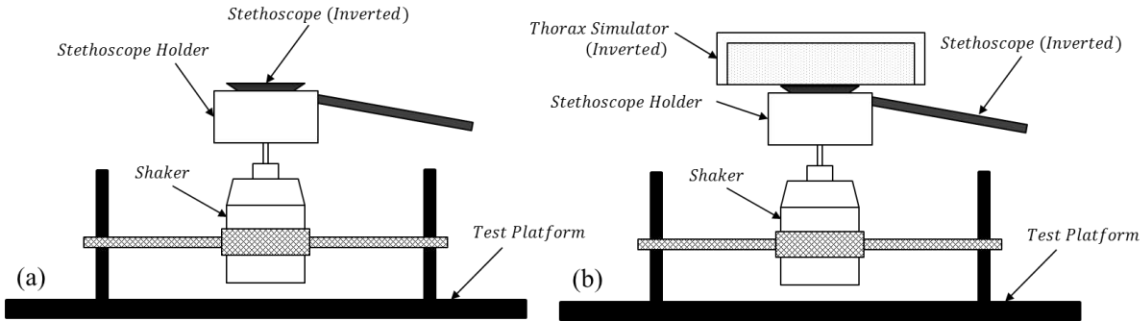

Figure 2-5: Frequency response test apparatus for simulating physician inputs while (a) unloaded and (b) loaded

This test can be conducted with and without the addition of a load on the piezo transducer. During normal operation, the stethoscope would be placed against the patient's body. Therefore, a more accurate end use measure would be testing the chestpiece backward transmission path sensitivity while loaded. This has been accomplished by applying the thorax simulator on top of the inverted stethoscope. The weight of the thorax simulator alone is used to apply the desired level of pressure. Its soft surface allows the load to conform to the face of the chestpiece as would normally occur with the patient's chest.

Employing the test methods as defined above, transfer functions for both the forward and backward mechanical transmission paths of an unmodified Model 3200 electronic stethoscope have been obtained (see Figure 2-6 and Figure 2-7).

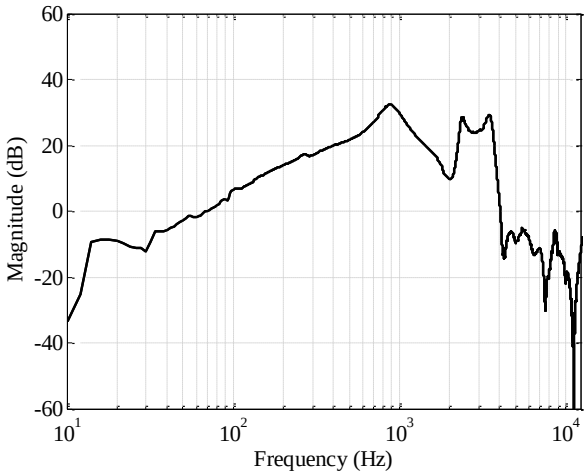

Figure 2-6: Experimental frequency response to white noise patient input

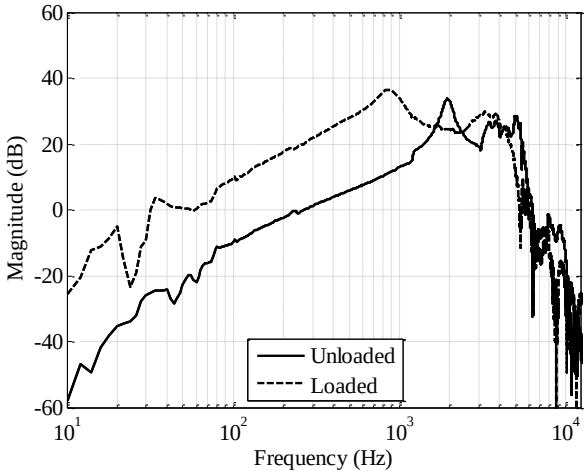

Figure 2-7: Experimental frequency response to white noise physician input

From these results, the following observations can be made:

- In all loading conditions, the stethoscope is more sensitive to inputs at intermediate frequencies. For noise sources of equal magnitude, a sound at 1000 Hz will be roughly 40 dB louder than one at 20 Hz.

- In both the patient and physician input frequency responses, three prominent resonant frequencies exist. However, for the physician input scenario, these resonances exist at higher frequencies.
- In the presence of physician inputs, a load on the face of the stethoscope causes the device's first dominant resonant peak to shift to a higher magnitude and lower frequency. Thus, the device is noticeably more sensitive to low frequency noise while loaded when compared to the unloaded case. In practice, the pressure applied by the physician during auscultation may vary and the actual frequency response encountered will vary between the two extremes presented—the loaded and unloaded case.

In order to provide a framework with which to interpret these and future frequency response data, it is important to recall the frequency range of clinically relevant auscultation signals. Using this information, it is possible to assess if or how the inherent system resonance affects a doctor's ability to assess chest sounds. The majority of auscultation signals fall below 1000 Hz, just above the first dominant resonant frequency in the stethoscope's dynamics. In this range, it can be seen that the stethoscope has an approximately equal sensitivity to chest sounds and handling noise (when placed on a patient's chest).

2.2 ONE-DIMENSIONAL MECHANICAL MODEL

To begin work on understanding the mechanical transmission of vibrations through the device, the stethoscope has been studied to identify the degrees of freedom necessary in a theoretical model. Deconstructing the device, each component capable of independent motion was identified. In the model, these were each treated as an individual mass and degree of freedom. Subsequently, to characterize the interactions between masses, the coupling between each component has been reduced to simple spring or spring/damper connections.

The resulting mechanical system has five degrees of freedom—five independent masses. Due to the device's construction, very little motion and/or dynamics are exhibited by these masses when exposed to lateral forces. Correspondingly, lateral forces induce very little bending in the piezoceramic sensor. Thus, their contribution to the output signal is negligible, and only forces acting through the plane of the piezo need be considered. It is possible, however, that an uneven force distribution on the face of the piezo may cause additional dynamics in the system due to tilting of each component. This motion could result in piezo bending and a noticeable output response. In practice, once the stethoscope is placed on a patient's chest, most vibration energy will be observed in the form of plane waves. Thus, the response due to localized forces—non-axisymmetric forces—is uncommon. Therefore, a uniaxial model in line with the piezo sensing element accounts for the majority of all practical input energy that will have a noticeable impact on the output signal. The resulting one dimensional model shown in Figure 2-8 clearly demonstrates the independent masses which have been identified and their corresponding interconnections.

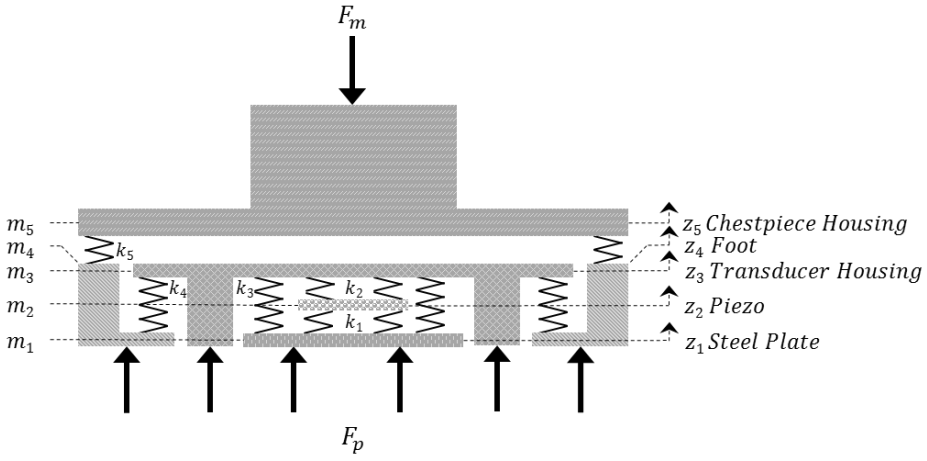

Figure 2-8: One-dimensional stethoscope mechanical model

Although they have not been explicitly illustrated in the simplified model representation above, at each spring location is a corresponding viscous damper.

In the selected one-dimensional stethoscope mechanical model, two independent inputs have been identified, F_p and F_m, corresponding to vibrational inputs from the patient and medic/physician respectively. In a noise free setting, F_m would correspond to the static force applied by a physician on the back of the stethoscope as it is placed on a patient's chest and F_p would correspond to the desired auscultation signal.

Using the defined inputs and established component relationships, the equations of motion for each independent mass have been derived. Combining these equations into a state-space representation, the stethoscope's dynamic model is given as follows:

$$\dot{x}_d = \mathrm{A_d} x_d + \mathrm{B_d} u \tag{2.2}$$

where $x_d \in \mathbb{R}^{10}$ is the state,

$$x_d = [z^{\mathrm{T}} \quad \dot{z}^{\mathrm{T}}]^{\mathrm{T}} \tag{2.3}$$

and $u \in \mathbb{R}^2$ is the input,

$$u = [F_p \quad F_m]^{\mathrm{T}} \tag{2.4}$$

The system matrices $\mathrm{A_d} \in \mathbb{R}^{10\times10}$ and $\mathrm{B_d} \in \mathbb{R}^{10\times2}$ are given by:

$$\mathrm{A_d} = \begin{bmatrix} 0_{5\times5} & \mathrm{I}_{5\times5} \\ -\mathrm{M}^{-1}\mathrm{K} & -\mathrm{M}^{-1}\mathrm{C} \end{bmatrix} \tag{2.5}$$

$$\mathrm{B_d} = \begin{bmatrix} 1/\mathrm{m}_1 & 0 & 1/\mathrm{m}_3 & 1/\mathrm{m}_4 & 0 & 0_{1\times5} \\ 0 & 0 & 0 & 0 & -1/\mathrm{m}_5 & 0_{1\times5} \end{bmatrix}^{\mathrm{T}} \tag{2.6}$$

with, M the mass matrix

$$\mathrm{M} = diag(m_1, m_2, m_3, m_4, m_5) \tag{2.7}$$

K the stiffness matrix,

$$\mathrm{K} = \begin{bmatrix} k_1 + k_3 & -k_1 & -k_3 & 0 & 0 \\ -k_1 & k_1 + k_2 & -k_2 & 0 & 0 \\ -k_3 & -k_2 & k_2 + k_3 + k_4 & -k_4 & 0 \\ 0 & 0 & -k_4 & k_4 + k_5 & -k_5 \\ 0 & 0 & 0 & -k_5 & k_5 \end{bmatrix} \tag{2.8}$$

and C the damping matrix,

$$\mathrm{C} = \begin{bmatrix} c_1 + c_3 & -c_1 & -c_3 & 0 & 0 \\ -c_1 & c_1 + c_2 & -c_2 & 0 & 0 \\ -c_3 & -c_2 & c_2 + c_3 + c_4 & -c_4 & 0 \\ 0 & 0 & -c_4 & c_4 + c_5 & -c_5 \\ 0 & 0 & 0 & -c_5 & c_5 \end{bmatrix} \tag{2.9}$$

After having identified the independent components and their dynamic relationships, it is necessary to ascribe numerical values to each parameter defined in the model. The mass of each component was easily measured and recorded. Since they are less easily measured, theoretical approximations based on material properties and dimensions were used to quantify the stiffness and damping values corresponding to each connection.

The foot of the stethoscope is connected to the chestpiece housing by four small screws. Based on the material and diameter of the screws and other dimensions of the joint, the stiffness of this connection is well defined [60].

$$k = \frac{\pi E d_c \tan \alpha_f}{\ln\left[\frac{\left(2L_i \tan \alpha_f + d_i - d_c\right)\left(d_i + d_c\right)}{\left(2L_i \tan \alpha_f + d_i + d_c\right)\left(d_i - d_c\right)}\right]} \tag{2.10}$$

where E is the modulus of elasticity, d_c is the face diameter, d_i is the outer thread diameter, α_f is the pressure distribution frusta angle, and L_i is the bolted length of the thread.

Proceeding in a similar manner, the connection between the transducer housing and the foot can be defined. Here, the connection is characterized by the stiffness of the tabs on the transducer housing. The tabs can each be treated as a beam rigidly supported on end. By calculating the moment of inertia of the tabs and using beam bending theory, a simple approximation can be made for the tab's stiffness [61]:

$$k = \frac{3EI}{L^3} \tag{2.11}$$

where E is the modulus of elasticity, I is the moment of inertia, and L is the length of the tab.

Lastly, an approximation is required to characterize the foam used on either side of the piezo in the transducer housing. Using a Kelvin-Voigt model with a spring and damper in parallel, the viscoelastic behavior of the foam can be approximated [62]. Subsequently, each foam connection can be estimated by defining the stiffness of the foam using Hooke's law [61]:

$$k = \frac{EA}{L} \tag{2.12}$$

where E is the modulus of elasticity of the foam, A is its cross-sectional area, and L is the length/height of the material.

Using equations (2.10), (2.11), and (2.12) with the applicable material properties and dimensions for each component, the stiffness of each joint was calculated. Using these values and adding a small level of damping to each connection provided a preliminary dynamic model approximation. Since an analytical expression for the damping at each connection is not readily available, all connections were assumed to a damping coefficient of 10%. These values were later refined using experimental verification. The mass, stiffness, and damping parameters employed in the final model can be found in Table 2-1.

Table 2-1: Mechanical model mass, stiffness, and damping parameters

Index, i	Mass, m_i	Stiffness, k_i	Damping, c_i
1	0.18	2.02×10^{4}	4.85×10^{-2}
2	0.11	1.36×10^{4}	9.99×10^{-2}
3	1.83	3.29×10^{4}	1.99×10^{-1}
4	2.46	4.25×10^{7}	1.41×10^{-1}
5	51.71	1.02×10^{7}	1.19×10^{1}

2.3 LUMPED PARAMETER PIEZOELECTRIC MODEL

The derived one-dimensional mechanical model can be used to relate the vibrational inputs to forces on the piezo sensing element. However, a conversion is required to relate these forces to an output voltage. For the piezo, the output voltage is proportional to the strain due to bending. The specific piezo element within this stethoscope is an

axisymmetric piezo unimorph with unequal radii for the piezoelectric layer and substrate (see Figure 2-9).

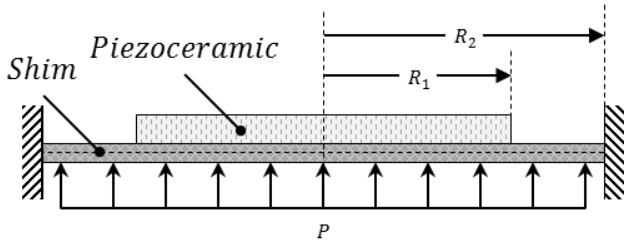

Figure 2-9: Cross-sectional schematic of piezoceramic transducer

Based on the material properties and geometric relationships of the shim and piezoceramic layers, it is possible to determine a two-port lumped parameter model that relates an applied pressure on the face of the shim to an induced voltage [63]. An equivalent circuit representation of this model can be seen in Figure 2-10.

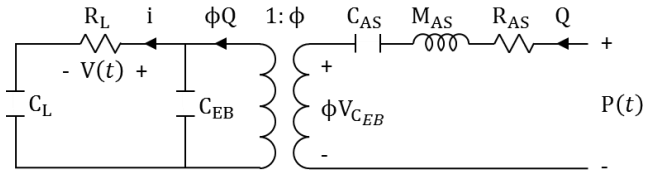

Figure 2-10: Two-port electroacoustic piezo model

In the acoustic domain of the equivalent lumped-element model, C_{AS} is the short circuit acoustic compliance, M_{AS} is the acoustic mass, and $P(t)$ is the uniform pressure load applied to the face of the shim. In order to account for structural damping and acoustic losses, an acoustic resistance, R_{AS}, has been added to the model.

The electrical and acoustic elements of the two-port model are related by an ideal transformer. The transformer turns ratio, ϕ, is the electroacoustic transduction coefficient. This quantity is given by the negative ratio of the volumetric displacement of the piezo due to a unit voltage loading relative to the volumetric displacement of the piezo due to a unit pressure loading.

In the electrical domain, the input/output voltage of the conventional electroacoustic model is given by the voltage across C_{EB}, the blocked electrical capacitance of the piezo. In order to account for losses and to include the effect of measuring this voltage, a small load resistance and capacitance, R_L and C_L respectively, have been added to this model. The new voltage output is taken as the voltage across the load resistor. This causes a high-pass filtering effect on the voltage across C_{EB}.

Using the selected two-port model representation, and selecting the two-port model states $x_p \in \mathbb{R}^3$ as

$$x_p = [Q \quad \dot{Q} \quad i]^{\mathrm{T}} \tag{2.13}$$

the state-space representation of the differential equations relating pressure and voltage can be written as follows

$$\dot{x}_p = \mathrm{A_p} x_p + \mathrm{B_p} \dot{P} \tag{2.14}$$

$$V = \mathrm{C_p} x_p \tag{2.15}$$

where the system matrices are given by

$$\mathrm{A_p} = \begin{bmatrix} 0 & 1 & 0 \\ -\frac{1}{M_{AS}}\left(\frac{\phi^2}{C_{EB}} + \frac{1}{C_{AS}}\right) & -\frac{R_{AS}}{M_{AS}} & \frac{\phi}{M_{AS} C_{EB}} \\ \frac{\phi}{R_L C_{EB}} & 0 & -\frac{1}{R_L}\left(\frac{1}{C_L} + \frac{1}{C_{EB}}\right) \end{bmatrix} \tag{2.16}$$

$$\mathrm{B_p} = \begin{bmatrix} 0 & \frac{1}{M_{AS}} & 0 \end{bmatrix}^{\mathrm{T}} \tag{2.17}$$

$$\mathrm{C_p} = [0 \quad 0 \quad R_L] \tag{2.18}$$

2.4 COMBINED STETHOSCOPE MODEL

In order to incorporate the electroacoustic piezo model into the previously derived mechanical vibration model, the pressure applied to the sensing element must be expressed in terms of the motions of physical components within the stethoscope. If you denote F_{12} as the forces exerted by the shim, m_1, on the piezo, m_2, then the pressure on the face of the piezo is given by

$$P = \frac{\mathrm{F}_{12}}{A} \tag{2.19}$$

Here, the area over which these forces act on the piezo is taken as the area of the shim, $A = \pi R_2^2$. From the mechanical model's dynamic equations, the relevant forces acting on the piezo are defined as

$$F_{12} = k_1(z_1 - z_2) + c_1(\dot{z}_1 - \dot{z}_2) \tag{2.20}$$

Applying equation (2.20) to equation (2.19) and using the state definitions given by equation (2.3), the equation for pressure can be written in matrix form as

$$P = \mathrm{C_d} x_d \tag{2.21}$$

where,

$$\mathrm{C_d} = \frac{1}{\mathrm{A}}[k_1 \quad -k_1 \quad 0 \quad 0 \quad 0 \quad c_1 \quad -c_1 \quad 0 \quad 0 \quad 0] \tag{2.22}$$

Augmenting the original mechanical model's state vector with states from the piezo two-port model as follows

$$x = \begin{bmatrix} x_d^{\mathrm{T}} & x_p^{\mathrm{T}} \end{bmatrix}^{\mathrm{T}} \tag{2.23}$$

and using the dynamic and two-port model state-space system matrices given by equations (2.5), (2.6), (2.16), and (2.17), the complete stethoscope model can be expressed as

$$\dot{x} = \begin{bmatrix} \mathrm{A_d} & 0_{10\times3} \\ 0_{3\times10} & \mathrm{A_p} \end{bmatrix} x + \begin{bmatrix} 0_{10\times1} \\ \mathrm{B_p} \end{bmatrix} \dot{P} + \begin{bmatrix} \mathrm{B_d} \\ 0_{3\times2} \end{bmatrix} u \tag{2.24}$$

Applying equation (2.21) to equation (2.24) and using the definition given by equation (2.2), the complete model is given by:

$$\dot{x} = \mathrm{A}x + \mathrm{B}u \tag{2.25}$$

$$V = \mathrm{C}x \tag{2.26}$$

where the combined state-space representation matrices have been defined as

$$\mathrm{A} = \begin{bmatrix} \mathrm{A_d} & 0_{10\times3} \\ \mathrm{B_p C_d A_d} & \mathrm{A_p} \end{bmatrix} \tag{2.27}$$

$$B = \begin{bmatrix} B_d \\ B_p C_d B_d \end{bmatrix} \tag{2.28}$$

$$C = [0_{1\times 10} \quad C_p] \tag{2.29}$$

2.5 MODEL VALIDATION

By applying all derived estimates to the established system model, a preliminary stethoscope model estimate was obtained. In order to validate the model against the actual physical performance of the stethoscope, the predicted frequency domain transfer function estimate was compared to frequency domain data from experiments on the unmodified stethoscope.

For valid comparisons between experimental data and the derived model, appropriate boundary conditions were required to obtain the theoretical response. These conditions accounted for the method by which the physical device was tested. Accordingly, the mass and elastic coupling due to contact between the stethoscope and thorax simulator needed to be incorporated into the theoretically obtained responses. This was accomplished by replacing the direct force input to the stethoscope model by forces acting on each mass on the face of the stethoscope through a spring and damper pair. The stiffness and damping were assumed to be proportional to the application area of each mass in contact with the thorax simulator. Similarly, the mass of the stethoscope holder used during physician input response testing was accounted for.

Model verification and validation were accomplished manually by comparing discrepancies between theoretical and experimental results. Since the damping values were not derived theoretically, their values were increased gradually until the theoretical model exhibited the same level of damping at each critical resonant frequency. Preference was given to agreement between the lower frequency modes and resonances. Although higher order dynamics can be important to understanding the full system behavior of the stethoscope, they do not interfere with the relevant frequency range for auscultation and can be regarded as having little effect on the stethoscope's overall

function. If future applications of this model require increased accuracy over a higher frequency range, more rigorous model fitting and model validation techniques can be employed to account for these dynamics. The resulting model estimate can be seen to demonstrate a high level of agreement with the experimental data for all testing conditions (see Figure 2-11 and Figure 2-12).

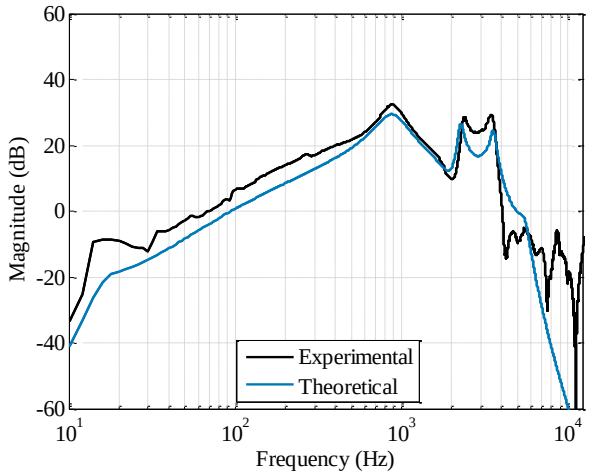

Figure 2-11: Theoretical and experimental frequency response to white noise patient input

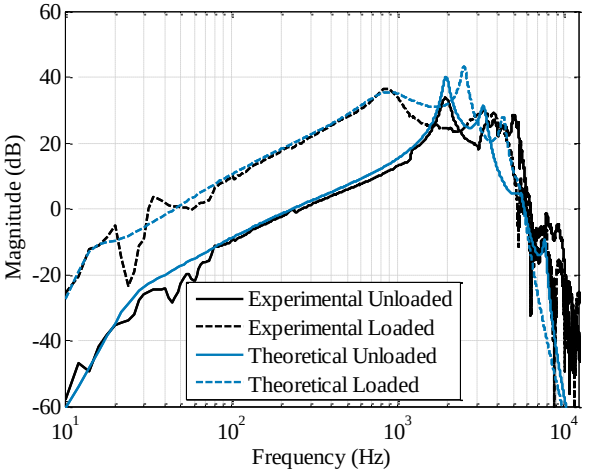

Figure 2-12: Theoretical and experimental frequency response to white noise physician input

2.6 CONCLUSIONS

In a digital stethoscope a piezoelectric transducer is used to convert the heart and lung induced motions of the chest into electrical signals. It has been demonstrated that during routine use of the device, physician handling noise created by rubbing of fingers on the chestpiece, motion of chestpiece on the patient's chest, tapping of fingers on chestpiece, etc., can possibly prevent successful auscultation.

In order to characterize the stethoscope response to excitation inputs from the physician's handling and from the patient's chest, a theoretical model has been developed and experimentally validated. The parameterized model enables detailed analysis and investigation into the effects of each component on the stethoscope's overall performance.

The transmission of vibrational inputs acting on the stethoscope from both sources (physician and patient) was characterized by a one-dimensional mechanical model. The connections between components were represented by elementary spring and damper pairs. The resulting forces on the piezoceramic transducer were related to a voltage signal by employing a two-port electroacoustic model. After applying initial theoretical estimates for each parameter value, the model was validated against experimentally obtained frequency responses of the stethoscope to white noise inputs from both the patient and physician. Accounting for minor discrepancies in the assumed levels of damping at each connection in the mechanical model, it demonstrates close agreement to the experimental data.

CHAPTER 3:

VIBRATION ISOLATION

3.1 MOTIVATION

This chapter focuses on reducing the influence of handling disturbances from the physician on measurements obtained with a piezoelectric stethoscope. Using a theoretical model of the stethoscope, methods to reduce the influence of these disturbances acting on the stethoscope's transducer are explored.

Based on predictions from the model, the introduction of vibration isolation so as to reduce the transmission of physician noise to the transducer is pursued. It is shown that direct vibration isolation between the transducer and the rest of the stethoscope structure leads to a reduction in coupling with the patient's chest. However, if isolation is instead introduced between the transducer housing and the body of the stethoscope, then vibration isolation from the physician is achieved with a far less reduction in patient coupling.

A modified stethoscope assembly is constructed to introduce the desired isolation and verify its efficacy. Experimental results from the modified stethoscope design are presented to study the influence of the proposed design changes and confirm the predicted model behavior.

3.2 THEORETICAL VIBRATION ISOLATION DESIGN

Having validated the stethoscope dynamic model with experimental results, it is possible to use the model to investigate potential design changes that could improve stethoscope performance. It was anticipated that by decoupling the sensor from the chestpiece, the device's susceptibility to handling noise could be effectively reduced.

Corresponding to the simplest physical change that could possibly provide the desired isolation, the first option explored was increased isolation between the chestpiece housing and transducer. In the model, this corresponds to a reduction of k_2. Simulations with the developed model revealed that the level of stiffness reduction required at this connection to achieve sufficient isolation from physician noise would cause poor coupling—loss in sensitivity—between the transducer and the patient's chest. The lack of a stiff connection behind the transducer results in less deformation of the piezoceramic element. Instead of bending, the piezo will have the tendency to experience rigid body motion. Thus, by this method of isolation, it is not possible to achieve a high sensitivity to auscultation signals while also successfully isolating the sensing element from undesired noise transmitted from/through the physician.

An alternate method of isolation is provided through a reduction of the stiffness between the transducer housing and the chestpiece. Physically, this corresponds to a reduction in stiffness of the metal tabs on the transducer housing (k_4) that are press-fit into the stethoscope foot. After implementing this change in the model, the predicted physician input frequency response due to increasing levels of isolation at this connection can be obtained (see Figure 3-1).

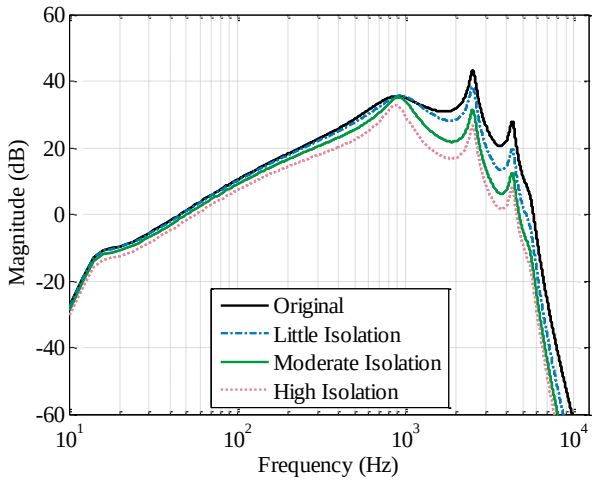

Figure 3-1: Theoretical frequency response to physician input with and without isolation

As shown, the model predicts that softening the connection between the chestpiece and transducer housing (leaving all other model parameters constant) moves a primary system corner frequency well below the first primary peak observed in the original system. After this resonance, the high frequency transmission of noise is considerably attenuated.

Looking at the patient input frequency response, it is evident that the isolation is achieved with little change to the device's sensitivity to patient input in the relevant frequency range (see Figure 3-2).

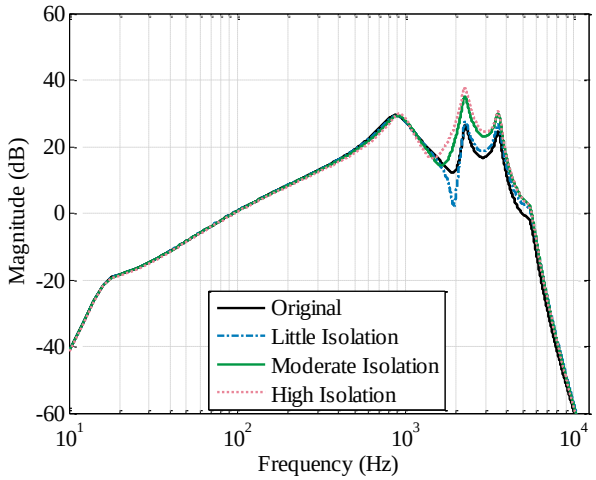

Figure 3-2: Theoretical frequency response to patient input with and without isolation

3.3 EXPERIMENTAL VIBRATION ISOLATION

3.3.1 *Modified Stethoscope Design*

In order to experimentally verify the change in the system response predicted theoretically, it was necessary first to alter the mechanical design of the stethoscope to accommodate modifications at the desired connection. For this purpose, the stethoscope foot and transducer housing were modified to allow a foam insert on either side of the transducer housing mounts.

The small metal tabs on the transducer housing are insufficient for the foam isolation intended. Specifically, the housing requires tabs with a larger surface area. This design is desired for both for ease of assembly as well as investigational purposes during the

prototype phase. With too small a surface, the size of foam used for isolation is limited. However, with a larger initial surface, the size of foam used can always be reduced as desired. In attempt to isolate the observed changes in performance to only those caused by the altered mounting configurations, the existing transducer housing assembly was incorporated into the new design. A small adapter was designed to mount firmly to the rear side of the transducer housing (see Figure 3-3). This adapter has the added mounting surfaces desired. The only change to the transducer housing is the removal of the small metal tabs that were initially used for mounting (see Figure 3-4).

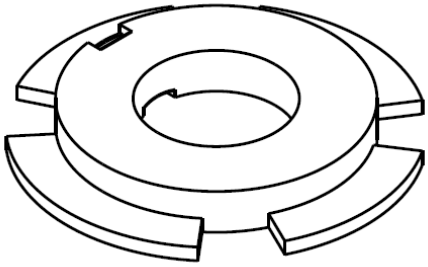

Figure 3-3: Transducer housing adapter for vibration isolation design

Figure 3-4: Modified transducer housing assembly with incorporated vibration isolation

Six different iterations of this adapter were built (see Table 3-1). The various adapters have different heights and different masses to allow a characterization of the effects of changes in each.

Table 3-1: Vibration isolation stethoscope prototype transducer housing adapters

Transducer Housing Adapter	Mass (g)	Height (mm)	Height (in)
Short, s	2.66	4.0	0.157
Short Hollow, sh	1.92		
Medium, m	2.93	4.5	0.177
Medium Hollow, mh	2.03		
Tall, t	3.19	5.0	0.197
Tall Hollow, th	2.15		

To accommodate the modified transducer housing, a small recess was included on the rear face of a new foot design. The diaphragm was constructed with two different pocket sizes, 3mm or 5mm. This provides the level of design flexibility necessary to vary the thickness of each isolation material.

Both the transducer housing adapters and feet designs were prototyped using a PC/ABS blend. The prototype material is similar to the material currently used to manufacture the foot on the commercially available Model 3200 electronic stethoscope.

Multiple different foam and rubber samples were selected to provide the desired isolation. By using samples with varying thicknesses and elastic moduli, it was possible to explore the effect of both decreased stiffness and increased damping at this connection. A summary of the full set of isolation samples can be seen in Table 3-2 below.

Table 3-2: Vibration isolation stethoscope prototype isolation materials

P/N	Material	Thickness (mm)	Thickness (in)
8614K71	Open Cell Polyurethane Foam, F1		
8722K13	Open Cell Polyethylene Foam, F2	3.18	.1250
-	Closed Cell Polyurethane Foam, F3		
8722K17	Open Cell Polyethylene Foam, F4	1.59	.0625
8824T122	40 OO Durometer Polyurethane Rubber, R1		
8824T123	50 OO Durometer Polyurethane Rubber, R2	1.52	.0600
8824T124	60 OO Durometer Polyurethane Rubber, R3		
8599K19	Natural Latex Rubber, R4	0.76	.0300

3.3.2 *Experimental Results*

Using the selected materials with the modified stethoscope, the level of added isolation resulting from the addition of foam mounts for the physician side mechanical transmission path, $H_{p,m}$, was experimentally tested. The same test methods were employed as had been used during original device characterization testing on the unmodified stethoscope.

After calibrating for small performance changes between individual piezo transducers, the results for physician input tests (with and without loading) with prototype designs in which transducer housing isolation was added (i.e. reduced k_4) can be seen in Figure 3-5.

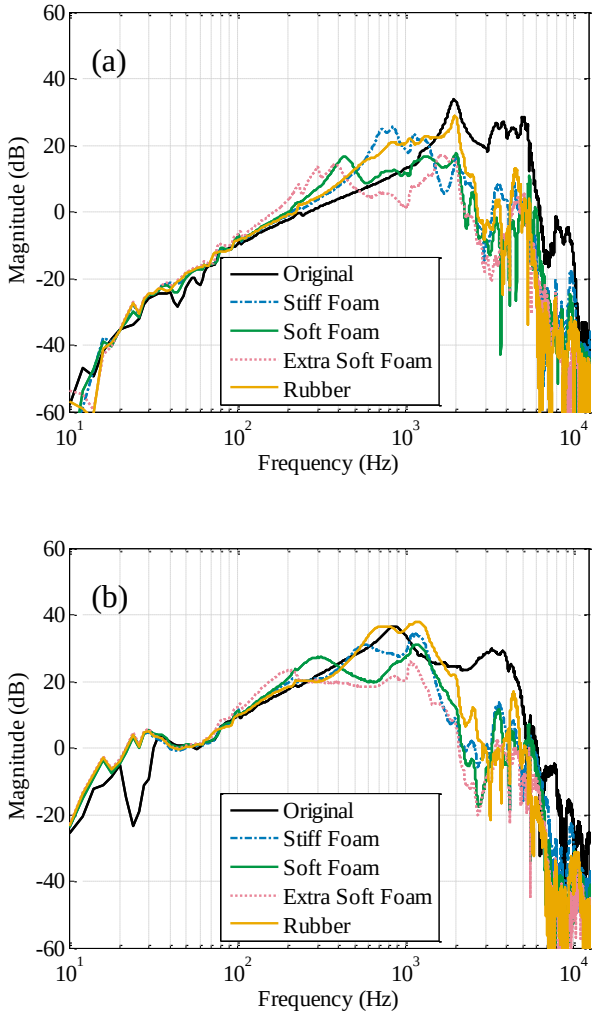

Figure 3-5: Experimental frequency response of stethoscope with vibration isolation to white noise physician inputs (a) unloaded and (b) loaded

The experimental results demonstrate that the added foam provides isolation from unwanted physician noise. This confirms the prediction made by the theoretical model. The softer the foam at this connection the greater the attenuation achieved. To more clearly highlight the differences between each of the experimental results, provided in Table 3-3 are the first primary resonant frequency and the H_2 norm for each experimental frequency response.

Table 3-3: Physician input frequency response (unloaded) summary.

Isolation	1st Corner Frequency (Hz)	Band-limited H_2 Norm			
		"Heart Sounds" 20Hz - 1kHz	"Lung Sounds" 500Hz - 1kHz	"Patient Noise" 20Hz - 2kHz	"Physician Noise" 20Hz – 12.8kHz
Original	1,950	74.34	69.99	721.64	1304.8
Stiff Foam	735	290.43	287.72	383.73	402.18
Soft Foam	450	109.18	81.36	209.28	228.72
Extra-Soft Foam	375	73.47	38.78	171.72	184.63
Rubber	1,375	198.01	193.17	519.11	581.14

In addition to moving a resonant mode of the system to this new lower frequency (i.e. 1st corner frequency listed in Table 3-3), the shifted mode has less damping—larger amplitude resonance. At frequencies higher than this resonance, the response is attenuated and the amplitude begins to roll off. Higher damping—smaller amplitude resonance—was expected for tests conducted with rubber samples. This is due to the increased energy dissipative characteristics of rubber. In agreement with these expectations, for these samples we observed lower amplitude resonance at the new location of the shifted resonant mode.

In order to fully understand the results of these changes to the physician side mechanical transmission path, they must be viewed in light of changes that also occurred to the frequency response for the patient side mechanical transmission path, $H_{p,p}$. Accordingly, the chestpiece prototype assemblies were tested using the thorax simulator. The results for these tests can be seen in Figure 3-6.

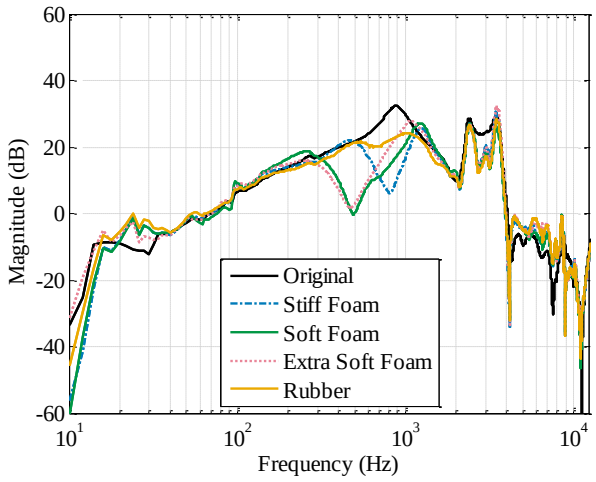

Figure 3-6: Experimental frequency response of stethoscope with vibration isolation to white noise patient inputs

These results demonstrate that the added isolation affected not only the physician side transmission path, but also the patient side transmission.

To objectively evaluate the effectiveness of the various isolation designs, it is helpful to normalize the results. Using the patient side transmission path frequency response of the unmodified Model 3200 stethoscope as the design standard, the following calculation can be performed on each data set.

$$G_{p,p} = \frac{\bar{H}_{p,p}}{H_{p,p}} \tag{3.30}$$

$$G_{p,m} = H_{p,m} * G_{p,p} \tag{3.31}$$

where the bar has been used to denote the frequency response of the unmodified stethoscope. Effectively, this equation normalizes all data sets to have an equivalent patient side transmission path frequency response. Any compensation necessary to achieve this equivalence has been added to the medic/physician side transmission path. By comparing this new frequency response curve for each data set, it is more reasonable to draw conclusions. These normalized frequency responses can be seen in Figure 3-7 below.

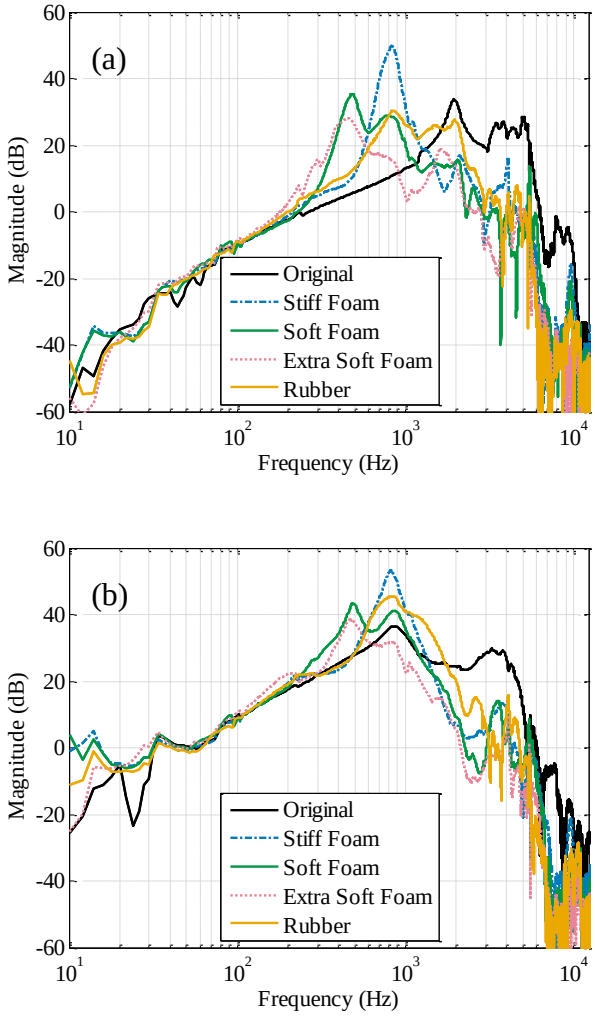

Figure 3-7: Normalized experimental frequency response of stethoscope with vibration isolation to white noise physician inputs (a) unloaded and (b) loaded

Using these normalized frequency responses, the system performance improvements and degradation are noted by a decrease and increase in the frequency response respectively. It is evident in each plot that the notch caused by the isolation in the patient side transmission path adversely affects performance. In all cases, this results in an overall degradation of stethoscope sensitivity to handling noise in the effected frequency range. However, it is evident that the stethoscope sensitivity to noise at frequencies above this range is considerably reduced.

Overall, it can be noted that the experimental results demonstrate a higher level of attenuation than originally predicted by the model. Additionally, the modified stethoscope's response to patient inputs has a narrowband loss in sensitivity that was not initially predicted. Theoretically, the change that was physically implemented should have corresponded to only a change in the connection stiffness k_4. However, in order to accommodate the isolation materials, a number of surrounding components were altered. In order to properly assess the model agreement to the added isolation, these changes in mass and configuration must be accounted for.

Making the required adjustments, the new model prediction is obtained (see Figure 3-8 and Figure 3-9).

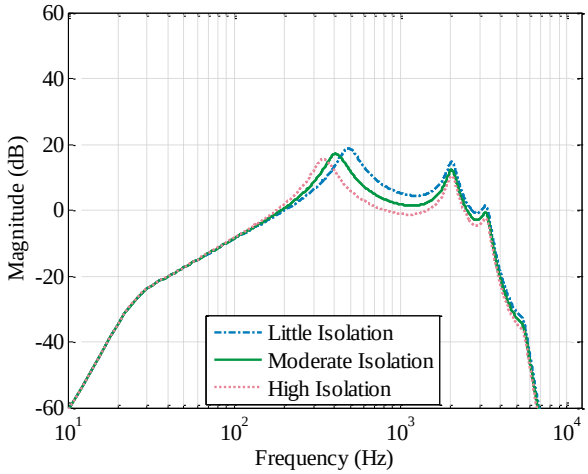

Figure 3-8: Theoretical frequency response of stethoscope with vibration isolation and adjusted masses to white noise physician input

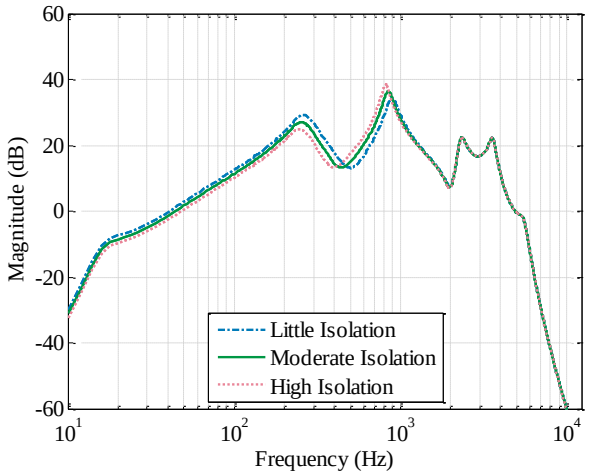

Figure 3-9: Theoretical frequency response of stethoscope with vibration isolation and adjusted masses to white noise patient input

After having verified the resulting changes in the stethoscope's response both experimentally and theoretically, it is necessary to assess the modified device's overall performance. Comparing all the experimental responses, it is evident that for all tests at frequencies below this resonance the performance is unaffected by the added isolation. For the unloaded stethoscope case, the isolation affects primarily only frequencies beyond the primary range of interest (20 Hz to 2 kHz). However, as noted with the original testing conducted on the unmodified stethoscope, the first major resonant frequency is shifted to lower frequencies and higher magnitudes once a load has been applied. The same is true of the added corner frequency caused by the new isolation designs. Thus, with an applied load, the isolation affects a much larger portion of the frequency range critical for auscultation.

These results demonstrate that the added isolation affected not only the physician side transmission path, but also the patient side transmission. A change in the frequency response for this path must be carefully considered. The isolation designs cause a loss in piezo sensitivity to patient noise between approximately 300 Hz and 1100 Hz. This was not originally predicted by theory given that the changes to surrounding components

required to accommodate the added isolation were not accounted for. Looking at both the experimental and theoretical results, it is evident that the softer the foam used in the isolation design, the lower the new resonant peak in the patient side transmission. In order to achieve comparable isolation without the observed loss in sensitivity, the isolation material must have both a low stiffness and high damping characteristic. These combined properties were not available in the isolation materials investigated. However, if a suitable material satisfying these conditions were introduced, successful isolation of the full relevant frequency range would be possible. Additionally, it is possible that by leveraging the model an optimal solution which combines simultaneous changes to multiple components and connections may be possible.

3.4 CONCLUSIONS

In order to investigate the effectiveness of added isolation at minimizing the propagation of handling noise to the piezo transducer, it was necessary to introduce soft vibration isolation mounts between the chestpiece and the transducer. Using the theoretical model, it was possible to demonstrate that traditional sensor isolation introduced immediately behind the sensing element would cause a large loss in stethoscope sensitivity to auscultation signals. If isolation is instead introduced between the transducer housing and the stethoscope foot, a greater reduction in handling noise can be achieved with less loss in patient noise sensitivity. The added mass of the transducer housing allows greater isolation to be realized while maintaining greater coupling of the sensing element with the patient's chest. This prevents a wideband reduction of patient noise sensitivity.

Experimentally, this work has been verified by introducing foam and other soft polymer materials as vibration isolation pads between the transducer housing and the stethoscope chestpiece. An improvement in vibration isolation from physician handling was achieved over a broad range of frequencies. However, this isolation was also found to cause some decrease in coupling with the patient's chest over a narrow range of frequencies.

Alternate passive isolation configurations and methods are possible, but based on the analysis conducted it is believed that each will result in some level of patient signal loss. For optimal performance a new isolation material is required which exhibits both low stiffness and high damping characteristics. If wideband isolation is desired without compromising the device sensitivity to patient sounds, it is also possible that active noise cancellation and other signal processing methods can be employed. Moving beyond simple frequency based filtering, these approaches could leverage information about the noise and/or device design to actively estimate and remove unwanted disturbance inputs.

CHAPTER 4:

DIRECTIONAL NOISE CANCELLATION

4.1 MOTIVATION

As discussed in the previous chapter, one of the potential noise sources in both transport and regular clinical settings is caused by a physician's handling of the stethoscope. This noise can be caused by finger/hand movement along the stethoscope chestpiece surface, accidental contact with the chestpiece, or muscle hand tremors. Modern electronic stethoscopes which have significantly larger chest pieces and metallic surface areas experience higher occurrence of handling noise. Mechanical isolation of the stethoscope's transducer from these noise sources is possible, but this isolation is often achieved at the cost of a loss in sensitivity to patient chest sounds.

If the noise source cannot be adequately decoupled from the transducer, it is advantageous to pursue alternate methods by which this noise can be removed digitally. This can make it possible to overcome the existing performance limitations of passive design approaches. Specifically, by applying control system theory and active noise reduction methods improved results may be obtained. Regarding the physician handling noise as an unknown disturbance input acting on the stethoscope system, it is possible to estimate and remove the effects of this noise by using knowledge of the stethoscope's dynamics.

The problem of unknown input estimation has long been investigated as a tool for use in control applications. This problem typically arises in systems subject to disturbances, unmeasurable inputs, un-modeled dynamics, or in applications that require fault detection and isolation.

For the linear time invariant system,

$$\dot{x} = Ax + Bd \tag{4.1}$$

$$y = Cx \tag{4.2}$$

where $x \in \mathbb{R}^n$, $d \in \mathbb{R}^p$, and $y \in \mathbb{R}^q$ and the system matrices A , B, and C are known, constant, and of appropriate dimension, the objective is to estimate the unknown input, d, given the measured signal y. In the broadest class of observers, no a priori knowledge of the unknown input is assumed.

Model inversion is one possible technique that has been established to generate a system mapping $R^{-1}: y \rightarrow u$ given an initial system map $R: u \rightarrow y$. Research in this area can be roughly divided into two categories—that of the left and right system inverse. The left inverse solves the problem of estimating the input, u, from a set of measurements, y. The right inverse solves the complementary problem of determining the input, u, that will produce a desired output, y. In the event that the number of inputs is equal to the number of outputs, these two inverses reduce to the same problem.

Looking at the topic of functional reproducibility, Brockett and Mesarović [64] gave the first necessary and sufficient conditions for invertibility. An alternate test for invertibility has been presented by Sain [65], but these two criteria have since been found to be equivalent [66, 67]. A strengthened version of these conditions has been presented by Willsky [68], and an alternate method which establishes invertibility based on the original system matrices (A, B, C, D) instead of its Markov parameters $(D, CB, CAB, \ldots)$ has been derived [69]. Brockett [70] provided an inversion algorithm for the linear time-invariant (LTI) single-input single-output (SISO) case. This was later generalized by Silverman [71] to include linear time-variable (LTV) systems. Dorato [72] derived a simplified criterion for invertibility and proposed a procedure for obtaining the inverse of a multiple-input multiple-output (MIMO) system. Further simplifications of this approach have since been presented by other authors [65, 73, 74]. Silverman has provided an iterative procedure for inversion of the MIMO system which includes a built-in existence test [75]. Also, he has demonstrated methods by which the inverse system can be reduced

after it has been constructed. Additional research has been conducted to study the stability of such inverse systems. The conditions for the existence of a stable system inverse and its construction are given by Moylan [76]. These preliminary findings were primarily focused on the existence of such systems and their inherent system properties. However, they do not account for unknown initial conditions and do not estimate the states.

Another approach for determining unknown inputs acting on a system can be achieved through the use of a so-called unknown input observer (UIO). Preliminary observer design in this area was in the interest of estimating the unknown state independent of the unmeasurable disturbances [77, 78]. However, the unknown disturbance itself was not estimated. The first standard rank condition—the so called "Observer Matching Condition" was developed by Kudva [79] to determine when a reduced order UIO was possible. This requirement demonstrated that the necessary and sufficient condition for this class of observers to exist for a given system is the following simple condition:

$$rank(CD) = rank(D) = p \tag{4.3}$$

Following from this condition, many reduced order UIO designs have been proposed [80, 81]. These approaches use a linear transformation to separate the state vector into two sets—those driven by the unknown input and those that are independent. Additionally, other authors have presented methods for full order UIO design [82, 83]. Unfortunately, this necessary rank condition widely limits their applicability to many real world systems.

A large advance in UIO theory has been the development of observers for system which do not satisfy the observer matching condition. In general, these systems will require the use of one or more output derivatives to successfully estimate the state and/or input. The work of Liu provides an approach for systems that violate the matching condition and have a relative degree equal to one [84]. However, this assumption on the relative degree is not valid for the stethoscope system which is explored here (and will generally not be valid for many applications). More recently, Floquet and Zhu have presented methods for systems with a higher relative degree [85, 86]. The approaches of both authors rely on the

use of high order sliding mode observers to estimate output derivatives. The methods which have been presented have complex design conditions and lack methods to add additional robustness considerations. Additionally, in practice the implementation of these sliding mode observers in discrete time can result in chatter. What is presented here is a simpler method by which a linear observer can be designed which requires only the solution of a linear matrix inequality and has a straight-forward discrete time implementation.

4.2 MODEL INVERSION BASED INPUT ESTIMATION

4.2.1 *Generating a Model Inverse*

Given the initial system model, it is possible to estimate the unknown input, d, for a class of linear time-invariant systems. Without loss of generality, it can be assumed that the matrices B and C are full column and row rank respectively. As is done by most authors, it is necessary to restrict the class of systems to those for which the number of unknown inputs is less than or equal to the number of available outputs, $p \leq q$. For convenience of presentation, we have chosen to omit a known control input as it does not apply to the system investigated here or alter the method described herein.

In order to obtain an expression for the unknown input, d, we first differentiate the output from equation (4.2). After taking the output derivative and substituting for the state dynamics, equation (4.1), we obtain the following

$$\dot{y} = C\dot{x} = C(Ax + \mathrm{Bd}) \tag{4.4}$$

Define the relative degree r_j for the j^{th} output as the number of times that this output needs to be differentiated for an input to appear, that is $C_j A^{i-1} B = 0$ for all $1 \leq i \leq r_j - 1$ and $C_j A^{r_j - 1} B \neq 0$.

Thus, after differentiating the j^{th} output r_j times, we obtain

$$y_j^{(r_j)} = C_j A^{r_j} x + C_j A^{r_j - 1} B d \tag{4.5}$$

where the superscript (l) denotes the l^{th} derivative of a variable. Choose p of the y_j such that $\sum r_j$ is minimized. Without loss of generality, assume that $r_1 \leq r_2 \leq \cdots \leq r_q$. Then, the output derivatives can be combined in increasing order of relative degree in matrix form as follows:

$$\begin{bmatrix} y_1^{(r_1)} \\ y_2^{(r_2)} \\ \vdots \\ y_p^{(r_p)} \end{bmatrix} = \begin{bmatrix} C_1 A^{r_1} \\ C_2 A^{r_2} \\ \vdots \\ C_p A^{r_p} \end{bmatrix} x + \begin{bmatrix} C_1 A^{r_1 - 1} B \\ C_2 A^{r_2 - 1} B \\ \vdots \\ C_p A^{r_p - 1} B \end{bmatrix} d \tag{4.6}$$

This can be written in the following compact notation

$$\bar{y} = \bar{C} x + \bar{D} d \tag{4.7}$$

by defining $\bar{y} \in \mathbb{R}^p$, $\bar{C} \in \mathbb{R}^{p \times n}$, and $\bar{D} \in \mathbb{R}^{p \times p}$ as

$$\bar{y} = \begin{bmatrix} y_1^{(r_1)} \\ y_2^{(r_2)} \\ \vdots \\ y_p^{(r_p)} \end{bmatrix}, \qquad \bar{C} = \begin{bmatrix} C_1 A^{r_1} \\ C_2 A^{r_2} \\ \vdots \\ C_p A^{r_p} \end{bmatrix}, \qquad \bar{D} = \begin{bmatrix} C_1 A^{r_1 - 1} B \\ C_2 A^{r_2 - 1} B \\ \vdots \\ C_p A^{r_p - 1} B \end{bmatrix} \tag{4.8}$$

If the matrix $\bar{D}$ is invertible, then equation (4.7) can be solved to find the input, d, in terms of the output derivatives and states

$$d = -F^{-1} C' x + F^{-1} y' \tag{4.9}$$

Applying equation (4.9) to the original system equation, a new state equation without the unknown input can be obtained:

$$\begin{aligned} \dot{x} &= Ax + B(-\bar{D}^{-1}\bar{C}x + \bar{D}^{-1}\bar{y}) \\ &= (A - B\bar{D}^{-1}\bar{C})x + B\bar{D}^{-1}\bar{y} \end{aligned} \tag{4.10}$$

If we define the matrices,

$$\begin{aligned} A_b &= A - B\bar{D}^{-1}\bar{C}, & B_b &= B\bar{D}^{-1}, \\ C_b &= -\bar{D}^{-1}\bar{C}, & D_b &= \bar{D}^{-1} \end{aligned} \tag{4.11}$$

the new dynamic equations relating the original system output to an estimate of the input is given by,

$$\dot{x} = A_b x + B_b \bar{y} \tag{4.12}$$

$$d = C_b x + D_b \bar{y} \tag{4.13}$$

The resulting system requires r_j derivatives of the measured output signal y_j to estimate the original system input(s). Correspondingly, the matrix A_b will have eigenvalues at zero with a minimum multiplicity of $\sum r_j$. This is shown in the results of Lemma 1 and Theorem 1 which follow.

Lemma 1. *Given* $A_b = A - B\bar{D}^{-1}\bar{C}$, *where* $A \in \mathbb{R}^{n\times n}$, $B \in \mathbb{R}^{n\times p}$, $\bar{C} \in \mathbb{R}^{p\times n}$, *and* $\bar{D} \in \mathbb{R}^{p\times p}$ *are nonzero matrices given by the definition provided by Eq. (16),* $r_j \in \mathbb{Z}$ *is smallest value for which* $C_j A^i B = 0$ *for all* $0 \le i < r_j - 1$ *and* $C_j A^{r_j - 1} B \neq 0$, *the matrix* $C_j A_b^k = C_j A^k$ *for all* $0 \le k \le r_j$ *and* $C_j A_b^l = 0$ *for all* $l \ge r_j$. ◇

Proof: If $r_j = 1$, then by using the fact that $C_j B = 0$ it is clear that

$$\begin{aligned} C_j A_b &= C_j[A - B\bar{D}^{-1}\bar{C}] \\ &= \left[C_j A - C_j B\bar{D}^{-1}\bar{C}\right] \\ &= C_j A \end{aligned} \tag{4.14}$$

Using similar methods, for systems where $r_j > 1$

$$\begin{aligned} C_j A_b^k &= C_j A_b A_b^{k-1} \\ &= C_j[A - B\bar{D}^{-1}\bar{C}]A_b^{k-1} \\ &= \left[C_j A - C_j B(\cdot)\right]A_b^{k-1} \end{aligned} \tag{4.15}$$

where $(\cdot)$ has been used to indicate a quantity that is not critical for the remainder of the derivation. Continuing to expand,

$$\begin{aligned} C_j A_b^k &= \left[C_j A - C_j B(\cdot)\right][A - B\bar{D}^{-1}\bar{C}]A_b^{k-2} \\ &= \left[C_j A^2 - C_j B(\cdot) - C_j AB(\cdot)\right]A_b^{k-2} \\ &= \left[C_j A^2 - C_j B(\cdot) - C_j AB(\cdot) - C_j A^2 B(\cdot)\right]A_b^{k-3} \\ &\vdots \\ &= C_j A^k - C_j B(\cdot) - C_j AB(\cdot) - \cdots - C_j A^{k-2}B - C_j A^{k-1}B(\cdot) \end{aligned} \tag{4.16}$$

Given that $C_j A^i B = 0$ for all $0 \leq i < r_j - 1$ this simplifies to

$$C_j A_b^k = C_j A^k \tag{4.17}$$

for all $0 \leq k < r_j$. Now, setting $k = r_j$ we find

$$C_j A_b^{r_j} = C_j A^{r_j} - C_j A^{r_j - 1} B \bar{D}^{-1} \bar{C} \tag{4.18}$$

Combining $C_j A_b^{r_j}$ for all increasing j in matrix form, this can be written as follows

$$\begin{bmatrix} C_1 A_b^{r_1} \\ C_2 A_b^{r_2} \\ \vdots \\ C_p A_b^{r_p} \end{bmatrix} = \begin{bmatrix} C_1 A^{r_1} \\ C_2 A^{r_2} \\ \vdots \\ C_p A^{r_p} \end{bmatrix} - \begin{bmatrix} C_1 A^{r_1 - 1} B \\ C_2 A^{r_2 - 1} B \\ \vdots \\ C_p A^{r_p - 1} B \end{bmatrix} \bar{D}^{-1} \bar{C} \tag{4.19}$$

Applying the definitions of $\bar{C}$ and $\bar{D}$ this can be simplified to

$$\begin{bmatrix} C_1 A_b^{r_1} \\ C_2 A_b^{r_2} \\ \vdots \\ C_p A_b^{r_p} \end{bmatrix} = \bar{C} - \bar{D} \bar{D}^{-1} \bar{C} = \bar{C} - \bar{C} = 0 \tag{4.20}$$

from which it is clear that each individual row is identically equal to zero, $C_j A_b^{r_j} = 0$. Further, it is clear that $C_j A_b^l = 0$ for all $r_j \leq l$. Thus, we have shown that $C_j A_b^i = C_j A^i$ for all $1 \leq i \leq r_j - 1$ and $C_j A_b^l = 0$ for all $r_j \leq l$. □

Theorem 1. *Given $A_b = A - B\bar{D}^{-1}\bar{C}$, where $A \in \mathbb{R}^{n \times n}$, $B \in \mathbb{R}^{n \times p}$, $\bar{C} \in \mathbb{R}^{p \times n}$, and $\bar{D} \in \mathbb{R}^{p \times p}$ are nonzero matrices given by the definition provided by Eq. (16), $r_j \in \mathbb{Z}$ is smallest value for which $C_j A^i B = 0$ for all $0 \leq i < r_j - 1$ and $C_j A^{r_j - 1} B \neq 0$, the square matrix A_b will have at least $\sum_1^p r_j$ eigenvalues at zero.* ◇

Proof: The matrix A_b has an eigenvalue at zero iff $\exists v \neq 0$ such that $A_b v = 0$ and $v^T A_b = 0$. Take $v^T = a\left(C_j A^{r_j - 1}\right)$ where $C_j \neq 0$ has rank 1, $a \in \mathbb{R}$, and $a \neq 0$. Then,

$$\begin{aligned} v^T A_b &= v^T A_b \\ &= a(C_j A^{r_j - 1}) A_b \end{aligned} \tag{4.21}$$

From Eq. (4.17) in Lemma 1, $C_j A^{r_j-1} = C_j A_b^{r_j-1}$, and Eq. (28) can be rewritten

$$\begin{aligned} v^T A_b &= a(C_j A_b^{r_j-1}) A_b \\ &= a C_j A_b^{r_j} \end{aligned} \tag{4.22}$$

and by employing Eq. (4.20) where $C_j A_b^{r_j} = 0$, this is reduced to

$$v^T A_b = 0 \tag{4.23}$$

Thus, $C_j A^{r_j-1}$ is an eigenvector of A_b with an associated eigenvalue at zero. Since there are p outputs, there are at least p eigenvalues at zero. Each of the p eigenvalues located at zero given by the eigenvectors above has algebraic multiplicity of r_j. By taking $v_2^T = a_2 C_j$ where $a_2 \in \mathbb{R}$, and $a_2 \neq 0$, it is possible to show that C_j is a generalized eigenvector of rank $r_j > 0$ of $A_b^{r_j}$. First, by employing Lemma 1, it is clear that C_j is an eigenvector of $A_b^{r_j}$ corresponding to an eigenvalue at zero.

$$\begin{aligned} v_2^T A_b^{r_j} &= a_2^T C_j A_b^{r_j} \\ &= 0 \end{aligned} \tag{4.24}$$

However, by the same Lemma it is possible to show that C_j is not an eigenvector of all lower powers of A_b. That is $\forall 1 \leq i \leq r_j - 1$

$$\begin{aligned} v_2^T A_b^i &= a_2^T C_j A_b^j \\ &= a_2^T C_j A^j \\ &\neq 0 \end{aligned} \tag{4.25}$$

Thus, based on generalized eigenvector theory the eigenvalue at zero corresponding to this eigenvector has a geometric multiplicity r_j. Therefore, it has been shown that there exist p eigenvalues at zero each with multiplicity r_j for the matrix $A_b = A - B\bar{D}^{-1}\bar{C}$. □

The system given by equations (4.12) and (4.13) will provide an exact solution for the state and unknown input only if the original system is minimum phase and the initial state $x(t_0) = x_0$ is perfectly known. In practice, the initial conditions are often unknown.

Accordingly, what follows is an observer design which uses output feedback to correct for unknown initial conditions.

4.2.2 *Model Inversion Based Input Observer*

In order to remove these restrictions and account for the effects of unknown initial conditions, it is possible to modify the design of the unknown input observer using classical observer design methods.

Choose the following update law for the state estimate

$$\dot{\hat{x}} = (A_b - LC)\hat{x} + B_b\bar{y} + Ly \tag{4.26}$$

where $L \in \mathbb{R}^{n\times p}$. Choose the Lyapunov candidate,

$$V = e^{\mathrm{T}}Pe \tag{4.27}$$

where $P = P^T \in \mathbb{R}^{n\times n}$. Differentiating,

$$\dot{V} = e^{\mathrm{T}}P\dot{e} + \dot{e}^{\mathrm{T}}Pe \tag{4.28}$$

From the state equation the state estimate error derivative can be rewritten as,

$$\begin{aligned}\dot{e} &= \dot{x} - \dot{\hat{x}}\\ &= (Ax + Bd) - (A_b\hat{x} + B_b\bar{y} + LCe)\\ &= (Ax + Bd) - [(A - B\bar{D}^{-1}\bar{C})\hat{x} + (B\bar{D}^{-1})(\bar{C}x + \bar{D}d) + LCe]\\ &= (A - LC - B\bar{D}^{-1}\bar{C})e\\ &= (A_b - LC)e\end{aligned} \tag{4.29}$$

and $\dot{V}$ can be simplified as follows

$$\begin{aligned}\dot{V} &= e^{\mathrm{T}}P[(A_b - LC)e] + [(A_b - LC)e]^T Pe\\ &= -e^{\mathrm{T}}Qe\end{aligned} \tag{4.30}$$

where $Q = Q^T \in \mathbb{R}^{n\times n}$ is defined as

$$Q = -P(A_b - LC) - (A_b - LC)^T P \tag{4.31}$$

If there exist a pair of symmetric positive-definite matrices P and Q that satisfy equation (4.31), then the observer can asymptotically estimate the unknown state. By extension, if

the observer guarantees that the state estimates will converge to the true state, the input estimate will converge to the true input.

$$\lim_{t\to\infty}(x-\hat{x})=0\Rightarrow\lim_{t\to\infty}\left(d-\hat{d}\right)=0 \tag{4.32}$$

The existence of this solution requires the pair (A_b, C) to be observable or at a minimum detectable. If the original system is observable and minimum phase, this condition on the pair (A_b, C) can be guaranteed. This is shown in Lemma 2 which follows.

Lemma 2. *Given the pair (A, C) is observable and the system is minimum phase, the pair (A_b, C) is detectable and the $\tilde{r}=\sum r_j$ modes at zero are observable.* ◇

Proof: The observability matrix for the original system is given by the following

$$\mathcal{O}=\begin{bmatrix} C \\ CA \\ \vdots \\ CA^{n-1} \end{bmatrix} \tag{4.33}$$

Given that the pair (A, C) is observable, the row rank of the matrix, $\mathcal{O}$, is equal to n. Define the observability matrix of the pair (A_b, C) as follows

$$\mathcal{O}_b=\begin{bmatrix} C \\ CA_b \\ \vdots \\ CA_b^{n-1} \end{bmatrix} \tag{4.34}$$

and let

$$\mathcal{O}'_{b_j}=\begin{bmatrix} C_j \\ C_jA_b \\ \vdots \\ C_jA_b^{n-1} \end{bmatrix}\ \forall 1\le j\le q \tag{4.35}$$

Then,

$$\mathcal{O}'_b=\begin{bmatrix} \mathcal{O}'_{b_1} \\ \mathcal{O}'_{b_2} \\ \vdots \\ \mathcal{O}'_{b_q} \end{bmatrix} \tag{4.36}$$

where $rank(\mathcal{O}_b') = rank(\mathcal{O}_b)$. Employing Lemma 1, the matrix $\mathcal{O}_{b_j}'$ can be simplified as follows

$$\mathcal{O}_{b_j}' = \begin{bmatrix} C_j \\ C_j A_b \\ \vdots \\ C_j A_b^{r_j-1} \\ C_j A_b^{r_j} \\ C_j A_b^{r_j+1} \\ \vdots \\ C_j A_b^{n-1} \end{bmatrix} = \begin{bmatrix} C_j \\ C_j A \\ \vdots \\ C_j A^{r_j-1} \\ C_j A_b^{r_j} \\ C_j A_b^{r_j+1} \\ \vdots \\ C_j A_b^{n-1} \end{bmatrix} = \begin{bmatrix} C_j \\ C_j A \\ \vdots \\ C_j A^{r_j-1} \\ 0 \\ 0 \\ \vdots \\ 0 \end{bmatrix} \tag{4.37}$$

By the original assumption that $rank(\mathcal{O}) = n$, the matrix $\mathcal{O}_{b_j}'$ has rank equal to r_j. Thus, for each output j there are r_j observable modes. Let λ be an observable mode of the system given by the pair (A_b, C). Then, by the Popov-Belevitch-Hautos (PBH) test,

$$rank\left(\begin{bmatrix} \lambda I - A_b \\ C \end{bmatrix}\right) = n \tag{4.38}$$

This is equivalent to stating that the pair (A_b, C) is unobservable if and only if there exists a $v \neq 0$ such that $A_b v = \lambda v$ and $Cv = 0$. Suppose that $\lambda = 0$ is an unobservable mode of the system, then

$$rank\left(\begin{bmatrix} -A_b \\ C \end{bmatrix}\right) \neq n \tag{4.39}$$

Thus, there must exist a nonzero v such that $A_b v = 0$ and $Cv = 0$. Recall from Lemma 1, that $CA_b = 0$ (i.e. C is a left eigenvector of A_b). By the first condition, v is a right eigenvector of A_b. The second condition requires that the product $Cv = 0$. However, by the orthogonality property of left and right-eigenvectors, the product of the left and right eigenvectors corresponding to a single eigenvalue should be equal to $\gamma \neq 0$ ($\gamma = 1$ if the eigenvectors are normalized). Thus, there exists a contradiction. Therefore, $\lambda = 0$ must be an observable mode of the pair (A_b, C). By extension, all $\tilde{r}$ modes at zero are observable. Since only $\tilde{r}$ observable modes were found to exist for the system, it can be concluded that all remaining $n - \tilde{r}$ modes of the system are unobservable. However, by

the original condition that the original system was minimum phase, the modes will be detectable. □

It has been shown that the states corresponding to the repeated eigenvalues at zero are observable. Additionally, it was demonstrated that all other eigenvalues—the zeros of the original system—are unobservable. Since we required the original system to be minimum phase, this guarantees that all poles of the observer are already or can be placed in the open left-half of the complex plane. Thus, a stable observer is possible.

The benefit of this observer design is that it does not require any assumptions about the boundedness of the unknown input. However, since it requires that the original system is minimum phase, it may rule out its applicability to some physical applications in which sensor locations relative to the input location may result in unstable zeros.

4.2.3 *Unknown Input Observer*

As an alternate method to estimate the unknown input of a system, it is possible to design an unknown input and state observer that does not rely on the construction of an inverse dynamic model.

Theorem 2. *If there exist observer gain matrices L and $\mathcal{G}$ and two symmetric positive-definite (SPD) matrices P_x, P_d, and Q such that*

$$Q = \begin{bmatrix} -P_x(A-LC) - (A-LC)^{\mathrm{T}}P_x & -P_xB + \tilde{\mathcal{C}}^{\mathrm{T}}\mathcal{G}^{\mathrm{T}}P_d \\ -B^{\mathrm{T}}P_x + P_d\mathcal{G}\tilde{\mathcal{C}} & P_d\mathcal{H}\widetilde{\mathcal{D}} + \widetilde{\mathcal{D}}^{\mathrm{T}}\mathcal{H}^{\mathrm{T}}P_d \end{bmatrix} \tag{4.40}$$

the observer given by

$$\dot{\hat{x}} = (A-LC)\hat{x} + B\hat{d} + Ly \tag{4.41}$$

$$\dot{\hat{d}} = -\mathcal{G}\tilde{\mathcal{C}}\hat{x} - \mathcal{H}\widetilde{\mathcal{D}}\hat{d} + \mathcal{G}\tilde{y} \tag{4.42}$$

can be used to asymptotically estimate both the state and the unknown input. ◇

Proof: For a system where each output has a relative degree r_j as previously defined, define the structures of the matrices, $\mathcal{G} \in \mathbb{R}^{p\times(\tilde{r}+q)}$, $\mathcal{H} \in \mathbb{R}^{p\times q}$, $\tilde{\mathcal{C}} \in \mathbb{R}^{(\tilde{r}+q)\times n}$, and $\widetilde{\mathcal{D}} \in \mathbb{R}^{q\times p}$ as follows:

$$\mathcal{G} = [G_1 \quad G_2 \quad \cdots \quad G_q], \qquad \mathcal{H} = [H_1 \quad H_2 \quad \cdots \quad H_q],$$

$$\tilde{\mathcal{C}} = \begin{bmatrix} \tilde{C}_1 \\ \tilde{C}_2 \\ \vdots \\ \tilde{C}_q \end{bmatrix}, \qquad \widetilde{\mathcal{D}} = \begin{bmatrix} \widetilde{D}_1 \\ \widetilde{D}_2 \\ \vdots \\ \widetilde{D}_q \end{bmatrix} \tag{4.43}$$

where

$$\tilde{r} = \sum_{i=1}^{q} r_i \tag{4.44}$$

and the sub-matrices $G_i \in \mathbb{R}^{p\times(r_i+1)}$, $H_i \in \mathbb{R}^{p\times 1}$, $\tilde{C}_i \in \mathbb{R}^{(r_i+1)\times n}$, and $\widetilde{D}_i \in \mathbb{R}^{1\times p}$ $\forall i \in \{1,2,\dots,q\}$ are defined as follows

$$G_i = [G_{i,0} \quad G_{i,1} \quad \cdots \quad G_{i,r_i}], \qquad H_i = G_{i,r_i},$$

$$\tilde{C}_i = \begin{bmatrix} C_i \\ C_iA \\ \vdots \\ C_iA^{r_i} \end{bmatrix}, \qquad \widetilde{D}_i = C_iA^{r_i-1}B \tag{4.45}$$

Then, define the observer update law as follows

$$\dot{\hat{x}} = (A - LC)\hat{x} + B\hat{d} + Ly \tag{4.46}$$

$$\dot{\hat{d}} = -\mathcal{G}\tilde{\mathcal{C}}\hat{x} - \mathcal{H}\widetilde{\mathcal{D}}\hat{d} + \mathcal{G}\tilde{\mathcal{y}} \tag{4.47}$$

where $L \in \mathbb{R}^{n\times q}$ and the output derivative vector, $\tilde{\mathcal{y}} \in \mathbb{R}^{\tilde{r}+q}$, is defined as

$$\tilde{\mathcal{y}} = \begin{bmatrix} \tilde{y}_1 \\ \tilde{y}_2 \\ \vdots \\ \tilde{y}_q \end{bmatrix} \tag{4.48}$$

with $\tilde{y}_i \in \mathbb{R}^{r_i+1}$

$$\tilde{y}_i = \begin{bmatrix} y_i \\ \dot{y}_i \\ \vdots \\ y_i^{(r_i)} \end{bmatrix} \tag{4.49}$$

Defining the state and input estimate errors as

$$e_x = x - \hat{x}, \qquad e_d = d - \hat{d} \tag{4.50}$$

the observer state estimate can be rewritten as

$$\dot{\hat{x}} = A\hat{x} + B\hat{d} + LCe_x \tag{4.51}$$

Similarly, after some manipulation, the unknown input estimate can be written as

$$\dot{\hat{d}} = \mathcal{G}\tilde{\mathcal{C}}e_x + \mathcal{H}\tilde{\mathcal{D}}e_d \tag{4.52}$$

In order to show that state and unknown input estimate errors converge to zero, we can choose the Lyapunov candidate

$$V = e_x^{\mathrm{T}}P_x e_x + e_d^{\mathrm{T}}P_d e_d \tag{4.53}$$

where $P_x \in \mathbb{R}^{n\times n}$ and $P_d \in \mathbb{R}^{p\times p}$. Differentiating the Lyapunov function, we obtain

$$\dot{V} = e_x^{\mathrm{T}}P_x\dot{e}_x + \dot{e}_x^{\mathrm{T}}P_x e_x + e_d^{\mathrm{T}}P_d\dot{e}_d + \dot{e}_d^{\mathrm{T}}P_d e_d \tag{4.54}$$

From the state equation, the state estimate error derivative can be rewritten as

$$\begin{aligned}\dot{e}_x &= \dot{x} - \dot{\hat{x}}\\ &= (Ax + Bd) - \left(A\hat{x} + B\hat{d} + LCe_x\right)\\ &= (A - LC)e_x + Be_d\end{aligned} \tag{4.55}$$

If we assume that the disturbance inputs are constant, $\dot{d} = 0$, then $\dot{e}_d = -\dot{\hat{d}}$, and $\dot{V}$ can be simplified as follows

$$\begin{aligned}\dot{V} = e_x^{\mathrm{T}}P_x[(A - LC)e_x + Be_d] + [(A - LC)e_x + Be_d]^{\mathrm{T}}P_x e_x\\ -e_d^{\mathrm{T}}P_d\left[\mathcal{G}\tilde{\mathcal{C}}e_x + \mathcal{H}\tilde{\mathcal{D}}e_d\right] - \left[\mathcal{G}\tilde{\mathcal{C}}e_x + \mathcal{H}\tilde{\mathcal{D}}e_d\right]^{\mathrm{T}}P_d e_d\end{aligned} \tag{4.56}$$

Expanding, this can be rewritten as follows

$$\begin{aligned}\dot{V} = e_x^{\mathrm{T}}[P_x(A - LC) + (A - LC)^{\mathrm{T}}P_x]e_x + e_x^{\mathrm{T}}\left[P_x B - \tilde{\mathcal{C}}^{\mathrm{T}}\mathcal{G}^{\mathrm{T}}P_d\right]e_d\\ +e_d^{\mathrm{T}}\left[B^{\mathrm{T}}P_x - P_d\mathcal{G}\tilde{\mathcal{C}}\right]e_x - e_d^{\mathrm{T}}\left[P_d\mathcal{H}\tilde{\mathcal{D}} + \tilde{\mathcal{D}}^{\mathrm{T}}\mathcal{H}^{\mathrm{T}}P_d\right]e_d\end{aligned} \tag{4.57}$$

In matrix form, this is given by

$$\dot{V} = -\begin{bmatrix}e_x^{\mathrm{T}} & e_d^{\mathrm{T}}\end{bmatrix}Q\begin{bmatrix}e_x\\ e_d\end{bmatrix} \tag{4.58}$$

where

$$Q = \begin{bmatrix} -P_x(A - LC) - (A - LC)^{\mathrm{T}} P_x & -P_x B + \tilde{\mathcal{C}}^{\mathrm{T}} \mathcal{G}^{\mathrm{T}} P_d \\ -B^{\mathrm{T}} P_x + P_d \mathcal{G} \tilde{\mathcal{C}} & P_d \mathcal{H} \widetilde{\mathcal{D}} + \widetilde{\mathcal{D}}^{\mathrm{T}} \mathcal{H}^{\mathrm{T}} P_d \end{bmatrix} \tag{4.59}$$

If there exists symmetric positive-definite matrices P_x, P_d, and Q that satisfy equation (4.59), then V is positive definite and $\dot{V}$ is negative definite on the entire space $\mathbb{R}^{n+p}$. Additionally, since V is radially unbounded, it is possible to conclude that $e_x = 0$ and $e_d = 0$ is a globally asymptotically stable equilibrium point. Thus, the given observer can guarantee that both the state and unknown input can be asymptotically tracked. It should be noted that although the disturbance was assumed to be an unknown constant, in practice a time varying disturbance can also be estimated in real-time if the sampling frequency is adequately fast.

4.2.4 *Observer Performance on an Example System*

In order to demonstrate the performance of the proposed input estimation methods, they can be applied to a simple low order single-input and single-output mass-spring-damper system. Here, a two mass system is presented where the unknown input is a force acting on one mass and the output is taken as the relative deflection between the two masses (see Figure 4-1).

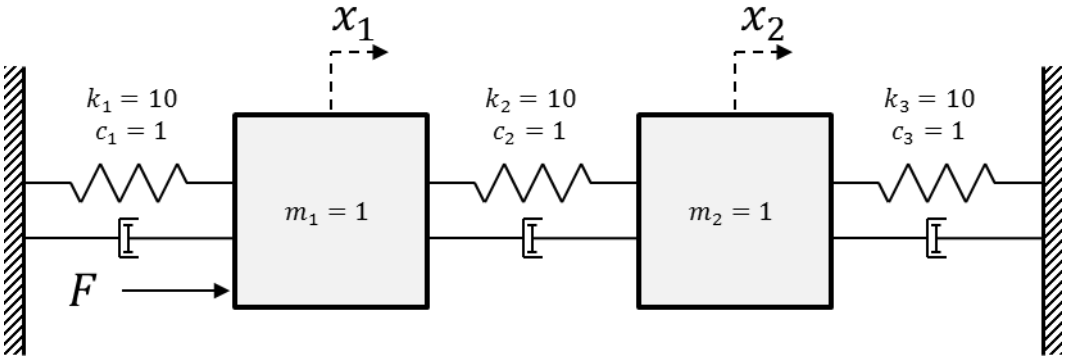

Figure 4-1: Schematic of two mass system for unknown input observer design example

In state-space form, the physical system's dynamic model is given as follows:

$$\dot{x} = \mathrm{A}x + \mathrm{B}d \tag{4.60}$$

$$y = Cx \tag{4.61}$$

where $x \in \mathbb{R}^4$ is the state, $d \in \mathbb{R}$ is the unknown force input, and the system matrices $A \in \mathbb{R}^{4\times4}$, $B \in \mathbb{R}^{4\times1}$, and $C \in \mathbb{R}^{1\times4}$ are given by:

$$A = \begin{bmatrix} 0 & 0 & 1 & 0 \\ 0 & 0 & 0 & 1 \\ -20 & 10 & -2 & 1 \\ 10 & -20 & 1 & -2 \end{bmatrix} \tag{4.62}$$

$$B = [0 \quad 0 \quad 1 \quad 0]^{\mathrm{T}} \tag{4.63}$$

$$C = [1 \quad -1 \quad 0 \quad 0] \tag{4.64}$$

First, to obtain the relative degree, r, take the derivative of the output until the input appears, that is $CA^{i-1}B = 0$ for all $1 \leq i \leq r-1$ and $CA^{r-1}B \neq 0$.

After differentiating the first time, we obtain

$$\dot{y} = C\dot{x} \tag{4.65}$$

$$= C(Ax + \mathrm{Bd}) \tag{4.66}$$

$$= [1 \quad -1 \quad 0 \quad 0]x + [0]d \tag{4.67}$$

Given that the input does not appear, we take the derivative again to obtain

$$\ddot{y} = CA\dot{x} \tag{4.68}$$

$$= CA(Ax + \mathrm{Bd}) \tag{4.69}$$

$$= [-30 \quad 30 \quad -3 \quad 3]x + [1]d \tag{4.70}$$

Here, the derivative explicitly appears (after two derivatives), therefore $r = 2$. Using equation (4.8) obtain the following $\bar{y} = y^{(2)}$, $\bar{C} = CA^2$, and $\bar{D} = CAB$. Then, from equation (4.11) the inverse system matrices are given as follows:

$$A_b = \begin{bmatrix} 0 & 0 & 1 & 0 \\ 0 & 0 & 0 & 1 \\ 10 & -20 & 1 & -2 \\ 10 & -20 & 1 & -2 \end{bmatrix} \tag{4.71}$$

$$B_b = [0 \quad 0 \quad 1 \quad 0]^{\mathrm{T}} \tag{4.72}$$

$$C_b = [30 \quad -30 \quad 3 \quad -3] \tag{4.73}$$

$$D_b = 1 \tag{4.74}$$

As anticipated, the resulting inverse system has two poles at zero ($\sum r = 2$). Thus, for non-zero initial conditions the resulting estimate will diverge. The required observer has been obtained by using a linear matrix inequality (LMI) solver. From the solver, it has been found that the observer gain

$$L = [0.74647 \quad -0.15893 \quad 15.84 \quad 14.562]^{\mathrm{T}} \tag{4.75}$$

and matrix

$$P = \begin{bmatrix} 1.7391 & 0.5904 & -0.49515 & 0.47155 \\ 0.5904 & 1.7335 & -0.027814 & 0.13696 \\ -0.49515 & -0.027814 & 0.76687 & -0.52263 \\ 0.47155 & 0.13696 & -0.52263 & 0.75352 \end{bmatrix}^{\mathrm{T}} \tag{4.76}$$

provide a positive definite Q as defined by equation (4.31).

Similarly, an unknown input observer can be designed that does not rely on the inverse system model. From equation (4.43) define the matrices $\tilde{C} \in \mathbb{R}^{3\times4}$, and $\widetilde{D} \in \mathbb{R}$ as

$$\tilde{C} = \begin{bmatrix} C \\ CA \\ CA^2 \end{bmatrix} = \begin{bmatrix} 1 & -1 & 0 & 0 \\ 0 & 0 & 1 & -1 \\ -30 & 30 & -3 & 3 \end{bmatrix} \tag{4.77}$$

$$\widetilde{D} = CAB = 1 \tag{4.78}$$

Again, using an LMI solver, the following matrices are obtained

$$G = [16.122 \quad 1.7669 \quad 0.53552] \tag{4.79}$$

$$H = 0.53552 \tag{4.80}$$

$$L = [0.13862 \quad -0.098478 \quad -13.968 \quad 13.961] \tag{4.81}$$

$$P = \begin{bmatrix} 1.7008 & 0.68044 & 0.080704 & -0.04769 \\ 0.68044 & 1.7528 & -0.031092 & 0.084743 \\ 0.080704 & -0.031092 & 0.27393 & -0.033885 \\ 0.04769 & 0.084743 & -0.033885 & 0.28682 \end{bmatrix}^{\mathrm{T}} \tag{4.82}$$

to provide a positive definite Q defined by equation (4.59).

To compare the baseline performance of each observer design, first the response was obtained when the unknown force was a constant, $d = 1$. A simple first order difference

equation was used to calculate the derivatives of the output signal. The error of the resulting estimates as a function of time can be seen in Figure 4-2.

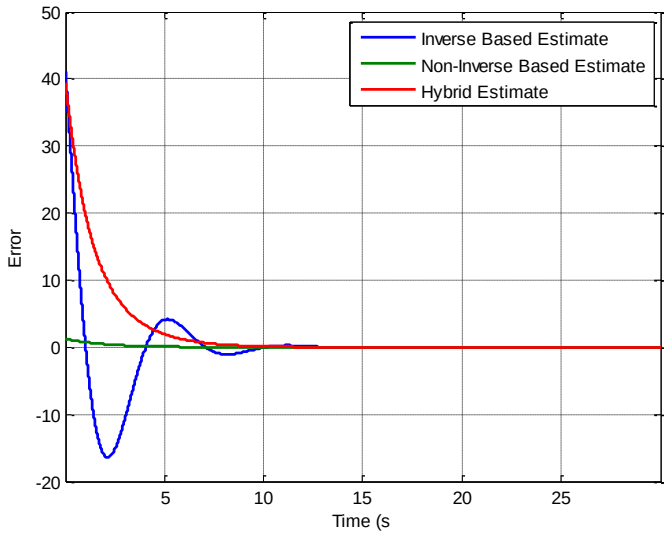

Figure 4-2: Unknown input observer estimate error convergence in response to a constant input

In addition to the two primary observers, a third hybrid estimate is presented. This estimate was obtained by combining the state dynamics from the non-inverse based observer with the estimate output equation from the inversion based observer. As shown in the figure, each estimate converges to zero. The inverse based estimate exhibits larger oscillatory transient behavior than the other two estimates. The hybrid estimate has comparable convergence speed but removes the transient oscillations. In contrast, the non-inverse based estimate has rapid convergence with no transient oscillations.

If simulations are repeated with a complex sinusoidal input, the following behavior is observed (see Figure 4-3).

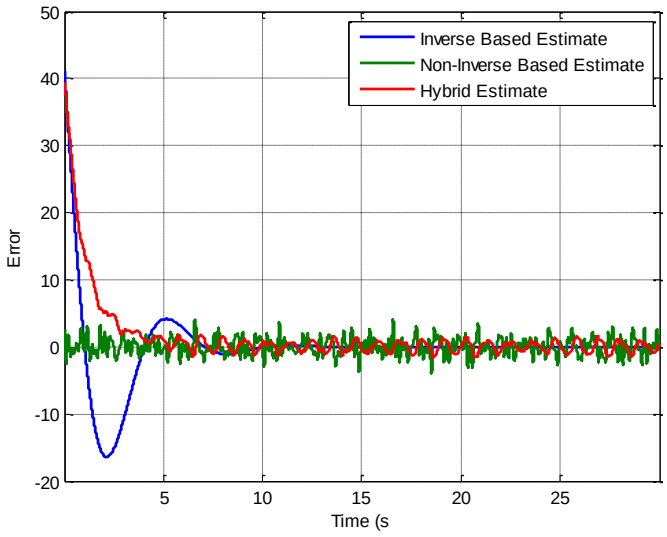

Figure 4-3: Unknown input observer estimate error convergence in response to a complex sinusoidal input

Here, the general shape of the error dynamics is preserved, but the non-inverse and hybrid estimates have a non-zero steady-state error. This is due to a violation of the assumption that the unknown input is constant. The inverse based estimate relies on no assumptions of the input behavior. Thus, its error demonstrates no change in behavior. The hybrid estimate has a transient steady-state error but with less high frequency components.

To improve the performance of the non-inverse based estimate, the gain of the observer matrices (G and H) can be increased by a constant factor. Scaling all elements of both matrices by 10^6 and using the same input signal, the following error is obtained (see Figure 4-4).

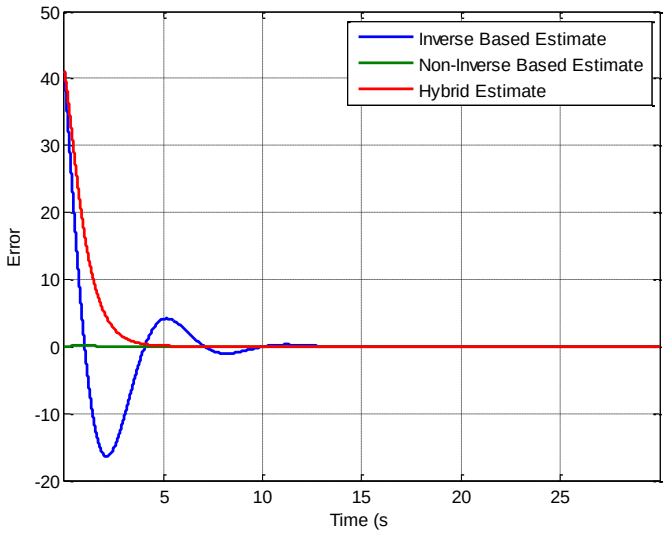

Figure 4-4: High gain unknown input observer estimate error convergence in response to a complex sinusoidal input

The effect of the larger gain can be seen as a decrease in the response time of the estimate to changes in the unknown input derivative. With a larger gain, the observer is more responsive. However, as with most high-gain observers, the resulting system will have an increased sensitivity to measurement noise.

As a final test of the observer performance, their response to a broadband random (white noise) input can be obtained (see Figure 4-5). As a worst case scenario, this signal tests the response of each observer to inputs at all frequencies.

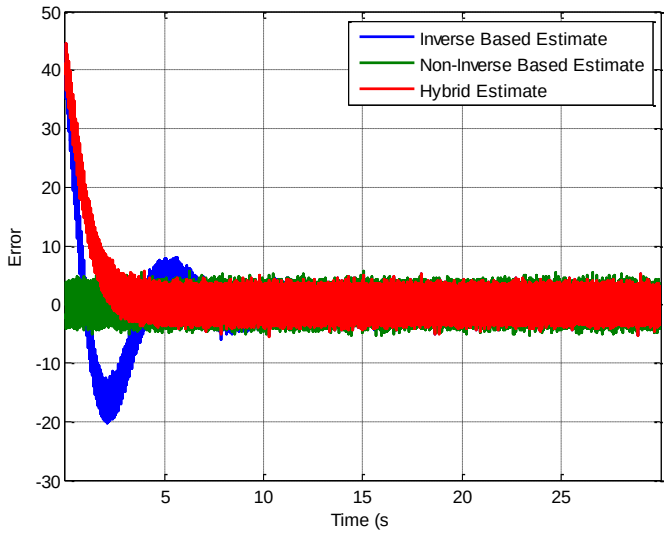

Figure 4-5: High gain unknown input observer estimate error convergence in response to a white noise input

It can be seen that the trend of each observer estimate error is preserved, but now each error has a non-zero error after "convergence." The nature of the error can be better understood by looking at the power spectral density of the original input signal and its estimates for the end of the simulation results (see Figure 4-6).

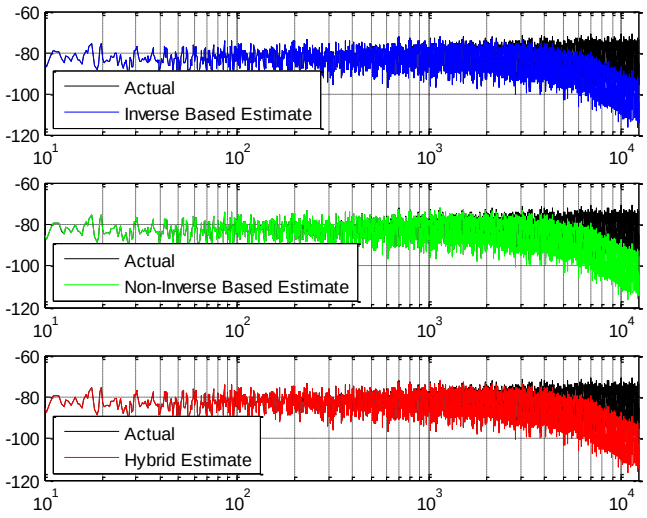

Figure 4-6: Power spectral density of high gain unknown input observer estimates in response to a white noise input

Each observer appears to fail at capturing the high frequency dynamics of the unknown input signal. This discrepancy can be attributed to errors in the derivatives obtained for the observers. The derivations of each observer relies having available the exact derivative of the measured system output signal. Without having access to this derivative, it is necessary to approximate it with a numerical derivative. The error shown here is a result of the error in a first order finite difference approximation given the sampling frequency employed. For a larger sampling frequency, the bandwidth of the observer estimate will increase. This implies that the sampling frequency is a critical design parameter which must be accounted for when applying the observers on a physical system.

4.3 STETHOSCOPE INPUT ESTIMATION

4.3.1 *Model Inversion*

Having verified the theoretical performance of the proposed unknown input/disturbance estimation algorithms, it was then necessary to apply this technique on the stethoscope problem. As stated in the introduction, our unknown input observer approach will rely on

the assumption that the number of system outputs (i.e. measurements) must be greater than or equal to the number of unknown inputs. Given that the stethoscope has two unknown inputs, at least one more measurement is required beyond that currently available in the original stethoscope design in order to accurately estimate and remove the effects of the unknown disturbance. Accordingly, a second piezo assembly has been added to the design. In order to reduce the complexity and verify the methodology, a simplified dual-piezo mechanical system has been constructed. The design consists of two identical subassemblies each with a piezo sensor. Both piezos are encased in a rigid transducer housing with an upper and lower foam ring support. The two assemblies are connected via a foam disk. A one-dimensional mechanical model of the resulting system can be seen in Figure 4-7 below.

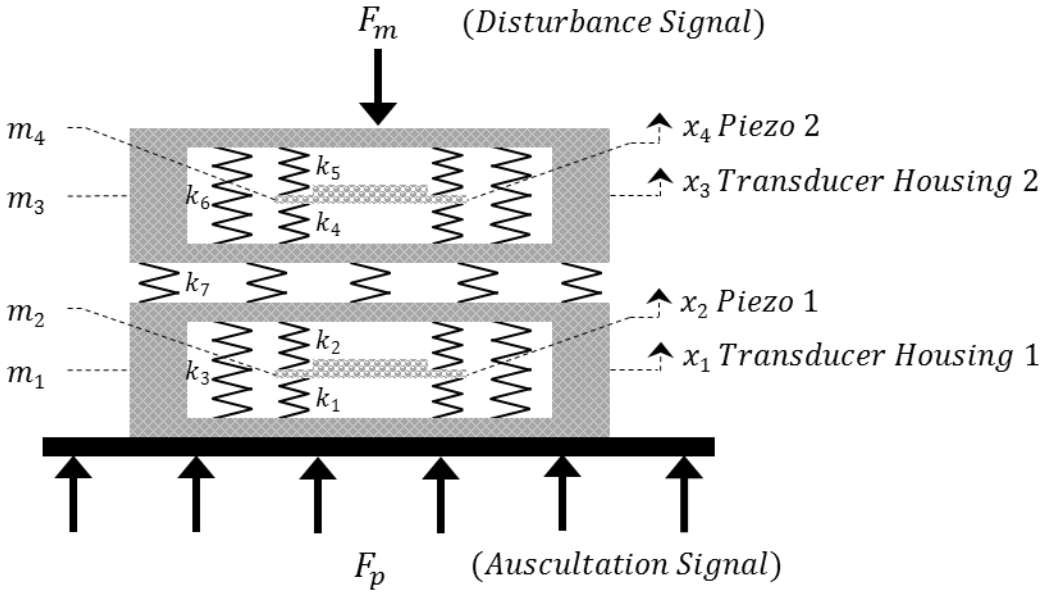

Figure 4-7: Dual-piezo transducer assembly one-dimensional mechanical model

Within the larger stethoscope body, this simplified mechanical design could be realized by the following

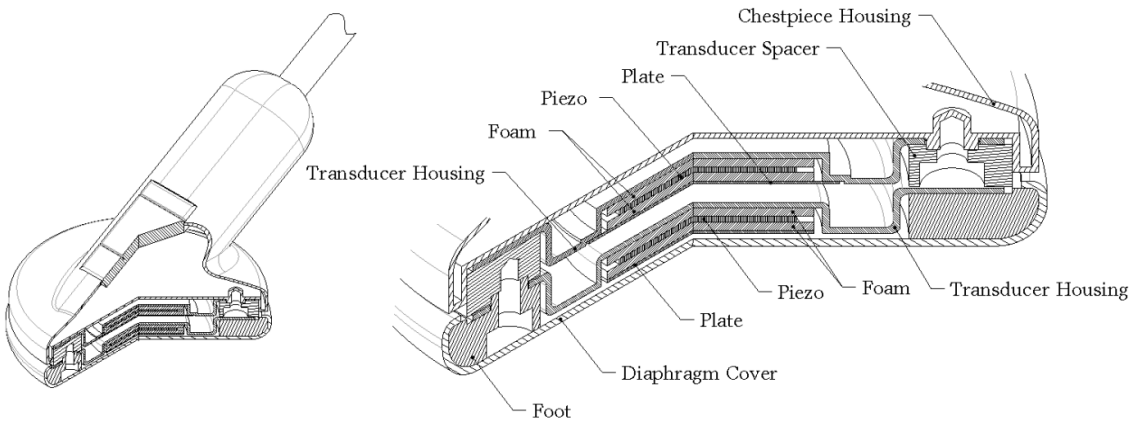

Figure 4-8: Preferred embodiment of a dual-piezo stethoscope assembly

In state-space form, the physical system's dynamic model is given as follows:

$$\dot{x}_{\mathrm{d}} = A_d x_d + B_d d \tag{4.83}$$

$$y_d = C_d x_d \tag{4.84}$$

where $x_d \in \mathbb{R}^8$ is the state and $d \in \mathbb{R}^2$ is the unknown input,

$$d = [F_p \quad F_m]^{\mathrm{T}} \tag{4.85}$$

The system matrices $A_d \in \mathbb{R}^{8\times 8}$, $B_d \in \mathbb{R}^{8\times 2}$, and $C_d \in \mathbb{R}^{2\times 8}$ are given by:

$$A_d = \begin{bmatrix} -44.08 & 1562.68 & 174.23 & -153.38 & 213.30 & 112.67 & -2.83 & 5.04 \\ -1562.68 & -94.40 & -158.90 & 213.71 & -261.99 & -185.22 & 6.18 & -8.10 \\ -175.56 & -161.87 & -420.59 & 4158.95 & -803.25 & -847.52 & 86.22 & -86.53 \\ 64.23 & -2.88 & -3615.96 & -537.89 & 1471.00 & 998.75 & -97.93 & 147.54 \\ -213.03 & -261.84 & -843.69 & -239.26 & -2021.47 & -4056.59 & 32.12 & 13.08 \\ 93.36 & 158.59 & 737.93 & -816.94 & 3875.64 & -1808.43 & 34.73 & 28.92 \\ -27.23 & -41.52 & -195.15 & -265.07 & -475.81 & -24.80 & -1030.82 & 4472.69 \\ -11.61 & -17.37 & -93.57 & -378.44 & -119.73 & -602.68 & -4383.90 & -2312.17 \end{bmatrix} \tag{4.86}$$

$$B_d = \begin{bmatrix} -82521.54 & -114774.36 & -156926.33 & -449007.32 & -107215.10 & -123552.41 & -172406.83 & -193414.42 \\ 300294.54 & 421995.38 & 445898.00 & -236420.39 & 670076.75 & -393644.12 & 52537.97 & -10752.79 \end{bmatrix}^{\mathrm{T}} \tag{4.87}$$

$$C_d = \begin{bmatrix} 8648.32 & -8602.71 & 67844.05 & -108708.54 & -82749.97 & -30555.85 & -179490.77 & 192359.08 \\ 311306.64 & -437240.50 & -467812.01 & 495665.84 & -673535.73 & -411445.29 & 16352.89 & -22863.65 \end{bmatrix} \tag{4.88}$$

The original model which was theoretically derived has been replaced by a minimal balanced realization. This model can be used to relate the vibrational inputs to pressure on the piezo sensing elements. However, a conversion is required to relate these forces to

output voltages. The state-space representation of the differential equations relating pressure and voltage for piezo i can be written as follows

$$\dot{x}_{p_i} = A_{p_i} x_{p_i} + B_{p_i} u_{p_i} \tag{4.89}$$

$$y_{p_i} = C_{p_i} x_{p_i} \tag{4.90}$$

where $x_{p_i} \in \mathbb{R}^3$ and the system matrices $A_{p_i} \in \mathbb{R}^{3\times3}$, $B_{p_i} \in \mathbb{R}^{3\times1}$, and $C_p \in \mathbb{R}^{1\times3}$ are given by:

$$A_{p_1} = \begin{bmatrix} -4923.06 & -26157.30 & -10510.92 \\ 32768.00 & 0 & 0 \\ 0 & 8192.00 & 0 \end{bmatrix},$$

$$A_{p_2} = \begin{bmatrix} -2808.29 & -22389.14 & -7334.77 \\ 32768.00 & 0.00 & 0.00 \\ 0.00 & 4096.00 & 0.00 \end{bmatrix},$$

$$B_{p_1} = \begin{bmatrix} 0.03 \\ 0 \\ 0 \end{bmatrix}, \qquad B_{p_2} = \begin{bmatrix} 0.06 \\ 0 \\ 0 \end{bmatrix},$$

$$C_{p_1} = [0 \quad 0 \quad 0.05], \qquad C_{p_2} = [0 \quad 0 \quad 0.04] \tag{4.91}$$

The output of each piezo sensor is quite small. In order to amplify and improve the signal quality, a small preamplifier circuit is used for each piezo. The state-space model for amplifier i is given by the following

$$\dot{x}_{a_i} = A_{a_i} x_{a_i} + B_{a_i} u_{a_i} \tag{4.92}$$

$$y_{a_i} = C_{a_i} x_{a_i} \tag{4.93}$$

where $x_{a_i} \in \mathbb{R}^5$ and the system matrices are given by

$$A_{a_1} = \begin{bmatrix} -44060.84 & -19445.95 & -7947.02 & -2397.29 & -1074.61 \\ 32768.00 & 0.00 & 0.00 & 0.00 & 0.00 \\ 0.00 & 16384.00 & 0.00 & 0.00 & 0.00 \\ 0.00 & 0.00 & 4096.00 & 0.00 & 0.00 \\ 0.00 & 0.00 & 0.00 & 512.00 & 0.00 \end{bmatrix}.$$

$$A_{a_2} = \begin{bmatrix} -62499.47 & -20212.80 & -10041.14 & -2805.13 & -723.10 \\ 65536.00 & 0.00 & 0.00 & 0.00 & 0.00 \\ 0.00 & 16384.00 & 0.00 & 0.00 & 0.00 \\ 0.00 & 0.00 & 4096.00 & 0.00 & 0.00 \\ 0.00 & 0.00 & 0.00 & 1024.00 & 0.00 \end{bmatrix},$$

$$B_{a_1} = [32 \quad 0 \quad 0 \quad 0]^{\mathrm{T}},$$
$$B_{a_2} = [16 \quad 0 \quad 0 \quad 0]^{\mathrm{T}},$$
$$C_{a_1} = [0.00 \quad 12.46 \quad 6.15 \quad 1.24 \quad 0.10]$$
$$C_{a_2} = [0.00 \quad 12.37 \quad 8.17 \quad 1.60 \quad 0.13] \tag{4.94}$$

For ease of development, the two preamplifier models will be stacked to create a decoupled two input and two output system, G_a, given by (A_a,B_a,C_a).

$$A_a = \begin{bmatrix} A_{a_1} & 0 \\ 0 & A_{a_1} \end{bmatrix}, \qquad B_a = \begin{bmatrix} B_{a_1} & 0 \\ 0 & B_{a_1} \end{bmatrix} \quad , C_a = \begin{bmatrix} C_{a_1} & 0 \\ 0 & C_{a_1} \end{bmatrix} \tag{4.95}$$

Similarly, the two piezo models have been stacked and the resulting system, G_p, is given by (A_p,B_p,C_p).

$$A_p = \begin{bmatrix} A_{p_1} & 0 \\ 0 & A_{p_1} \end{bmatrix}, \qquad B_p = \begin{bmatrix} B_{p_1} & 0 \\ 0 & B_{p_1} \end{bmatrix}, \quad C_p = \begin{bmatrix} C_{p_1} & 0 \\ 0 & C_{p_1} \end{bmatrix} \tag{4.96}$$

Schematically, the interconnection of the sub-systems can be seen in Figure 4-9. The following change of notation will be introduced for the complete system model: $u_1 \triangleq F_p$, $u_1 \triangleq F_m$, $y_1 \triangleq y_{a_1}$, and $y_2 \triangleq y_{a_2}$.

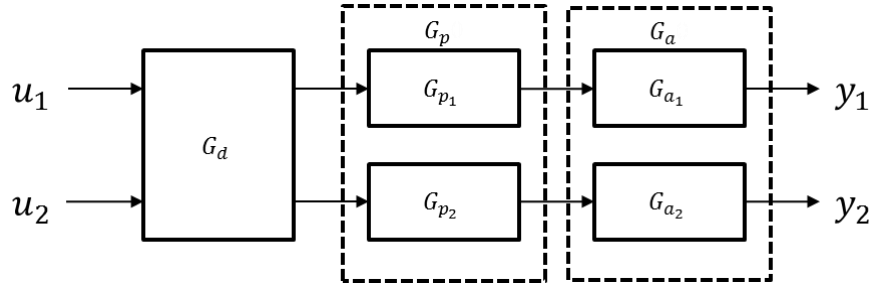

Figure 4-9: Dual-piezo sensor system model schematic diagram

4.3.2 *Observer Design*

It is possible to construct a full system observer for the combined model. However, here we have chosen to design an unknown input observer for each cascaded subsystem. This minimizes the number of output derivatives required for each estimator (i.e. reduces the effect of measurement noise).

The dynamic model, G_d, has well defined relative degree equal to one for each output $\left(r_{d_1} = 1, r_{d_2} = 1\right)$. The piezo subsystems each have a relative degree of three $\left(r_{p_1} = 3, r_{p_2} = 3\right)$, and each preamplifier subsystem has a relative degree of two $\left(r_{a_1} = 2, r_{a_2} = 2\right)$.

The inversion based observer for this system can be given by

$$\dot{\hat{x}}_a = \left(A_{b,a} - L_a C_a\right)\hat{x}_a + B_{b,a}\bar{y}_a + L_a y_a \tag{4.97}$$

$$\dot{\hat{x}}_p = \left(A_{b,p} - L_p C_p\right)\hat{x}_p + B_{b,p}\hat{\bar{y}}_p + L_p \hat{y}_p \tag{4.98}$$

$$\dot{\hat{x}}_d = \left(A_{b,d} - L_d C_d\right)\hat{x}_d + B_{b,d}\hat{\bar{y}}_d + L_d \hat{y}_d \tag{4.99}$$

where the observer gains $L_a \in \mathbb{R}^{8\times 2}$, $L_p \in \mathbb{R}^{6\times 2}$, and $L_d \in \mathbb{R}^{10\times 2}$ were selected as

$$L_d = \begin{bmatrix} -3.39\text{e}^{-3} & -4.30\text{e}^{-3} & -1.04\text{e}^{-2} & -1.73\text{e}^{-2} & -3.99\text{e}^{-4} & -5.27\text{e}^{-3} & 5.76\text{e}^{-3} & -1.74\text{e}^{-3} \\ -1.77\text{e}^{-3} & -1.52\text{e}^{-3} & 8.06\text{e}^{-4} & 5.42\text{e}^{-4} & 2.68\text{e}^{-4} & -4.26\text{e}^{-4} & 3.60\text{e}^{-5} & 2.21\text{e}^{-4} \end{bmatrix}^{\mathrm{T}},$$

$$L_p = \begin{bmatrix} 516.16 & 713052.69 & 2797.54 & 0 & 0 & 0 \\ 0 & 0 & 0 & 240.93 & 1078955.40 & 3684.15 \end{bmatrix}^{\mathrm{T}},$$

$$L_a = \begin{bmatrix} 43.08 & 0 \\ 151.58 & 0 \\ 280.68 & 0 \\ 2157.8 & 0 \\ 709.71 & 0 \\ 0 & 1.5636 \\ 0 & -6.0234 \\ 0 & 37.024 \\ 0 & 443.2 \\ 0 & 348.38 \end{bmatrix} \tag{4.100}$$

by solving the linear matrix inequality given by condition that a positive definite P and Q must exist where Q is defined by equation (4.31). The remaining observer system matrices are defined by equation (4.11).

It is important to note that since a cascaded observer design was selected all systems after the first observer rely on the use of output estimates (the result of the prior observer's estimate) and not a direct measurement. In the steady state, the internal stability of each observer guarantees that the cascaded observer will converge.

Similarly, a non-inversion based observer can be design for the stethoscope system. The state estimates are given by the following

$$\dot{\hat{x}}_a = (A_a - L_a C_a)\hat{x}_a + B_a \hat{d}_a + L_a y_a \tag{4.101}$$

$$\dot{\hat{x}}_p = \left(A_p - L_p C_p\right)\hat{x}_p + B_p \hat{d}_p + L_p \hat{y}_p \tag{4.102}$$

$$\dot{\hat{x}}_d = (A_d - L_d C_d)\hat{x}_d + B_d \hat{d}_d + L_d \hat{y}_d \tag{4.103}$$

The update laws for the unknown input estimates for each stage of the observer are given by

$$\dot{\hat{d}}_a = -\mathcal{G}_a \tilde{\mathcal{C}}_a \hat{x}_a - \mathcal{H}_a \tilde{\mathcal{D}}_a \hat{d}_a + \mathcal{G}_a \tilde{\mathcal{Y}}_a \tag{4.104}$$

$$\dot{\hat{d}}_p = -\mathcal{G}_p \tilde{\mathcal{C}}_p \hat{x}_p - \mathcal{H}_p \tilde{\mathcal{D}}_p \hat{d}_p + \mathcal{G}_p \tilde{\mathcal{Y}}_p \tag{4.105}$$

$$\dot{\hat{d}}_d = -\mathcal{G}_d \tilde{\mathcal{C}}_d \hat{x}_d - \mathcal{H}_d \tilde{\mathcal{D}}_d \hat{d}_d + \mathcal{G}_d \tilde{\mathcal{Y}}_d \tag{4.106}$$

The state observer gains $L_a \in \mathbb{R}^{8\times 2}$, $L_p \in \mathbb{R}^{6\times 2}$, and $L_d \in \mathbb{R}^{10\times 2}$ and the disturbance observer gains $\mathcal{G}_a \in \mathbb{R}^{2\times 4}, \mathcal{G}_p \in \mathbb{R}^{2\times 4}, \mathcal{G}_d \in \mathbb{R}^{2\times 6}$, $\mathcal{H}_a \in \mathbb{R}^{2\times 2}$, $\mathcal{H}_p \in \mathbb{R}^{2\times 2}$, and $\mathcal{H}_p \in \mathbb{R}^{2\times 2}$ were obtained by solving the linear matrix inequality given by condition that a positive definite P and Q must exist where Q is defined by equation (4.59). The remaining observer system matrices are defined by equation (4.45).

4.3.3 *Simulation Results*

The first step to verifying the designed unknown input/disturbance observer was to benchmark its performance using simulated data. Perfect measurements were obtained by passing inputs through the original theoretical system model. A clean heart sound recording was used for the desired patient signal. The disturbance input was created by generating a pure white noise signal. In this simulated scenario it is possible to compare to resulting signal estimates to the known input signals.

After applying the specified input signals to the original dual-piezo model (with random initial conditions), the following two output measurements were obtained (see Figure 4-10).

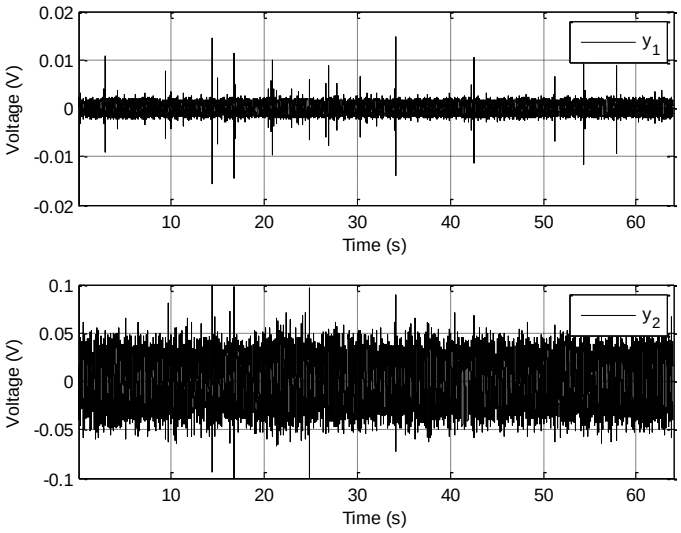

Figure 4-10: Simulated dual-piezo sensor system measurement signals

It is evident that the noise due to the disturbance input is sufficient to completely mask the desired auscultation signal in either measurement. Applying these measurements to the unknown input estimation algorithm, the following input signal estimate errors are obtained (see Figure 4-11 and Figure 4-12).

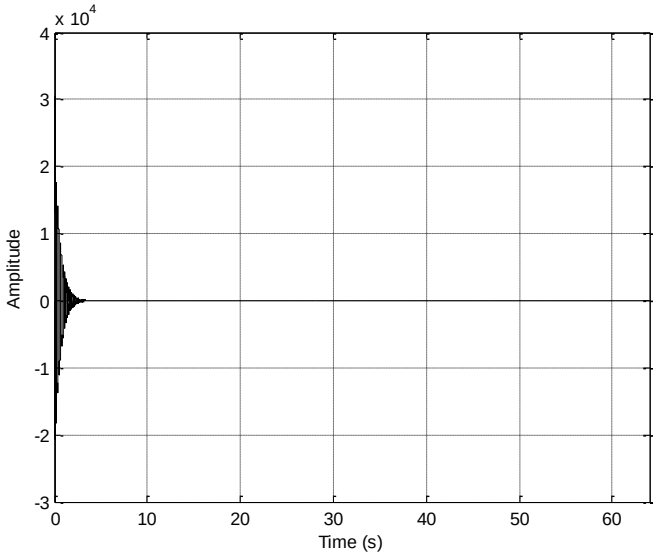

Figure 4-11: Simulated dual-piezo sensor system estimated patient input signal error

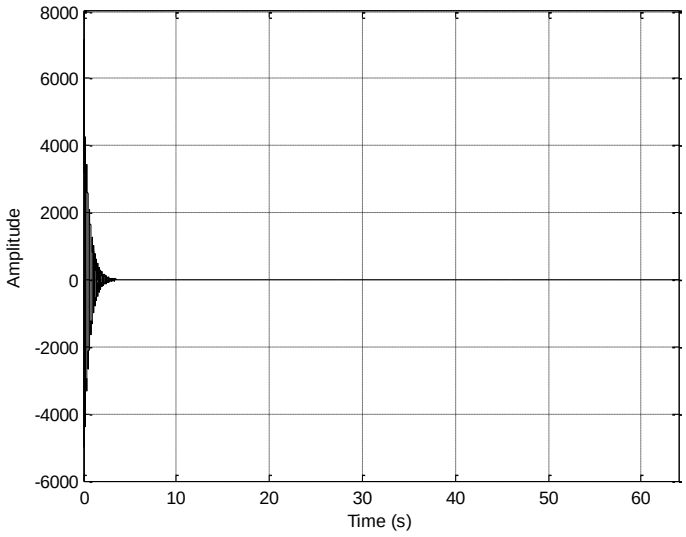

Figure 4-12: Simulated dual-piezo sensor system estimated disturbance input signal error

In this expanded time window, it is possible to see that the error in both estimates converges after approximately 4 seconds. The large initial error is due to the unknown initial conditions. As the observer begins to accurately estimate the state trajectories, the input estimates converge. Looking at the end of the simulation results, it is possible to observe the performance of the converged estimates (see Figure 4-13 and Figure 4-14).

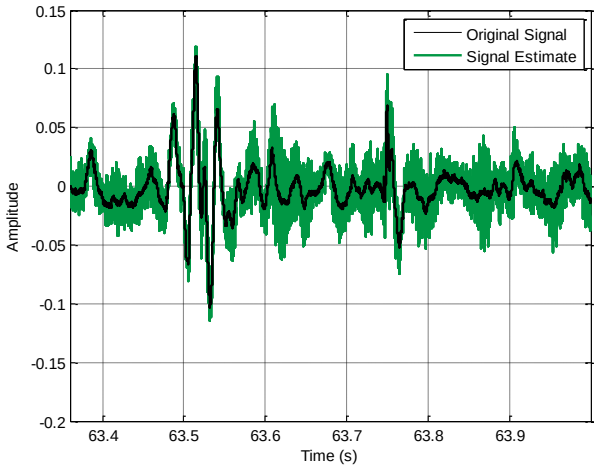

Figure 4-13: Simulated dual-piezo sensor system estimated patient input signal

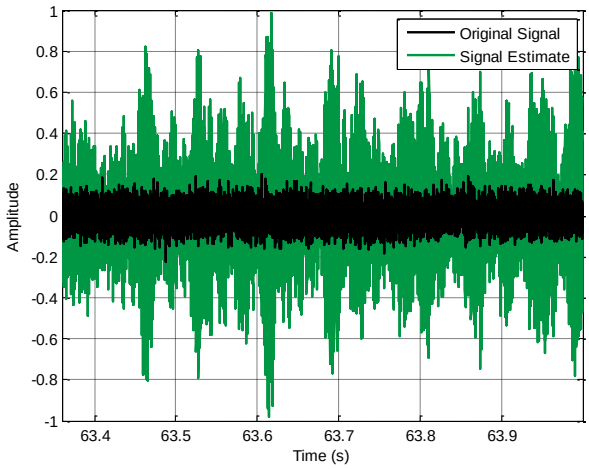

Figure 4-14: Simulated dual-piezo sensor system estimated disturbance input signal

Although the heart sound is visible in the patient input estimate, it is obstructed by the presence of significant high frequency noise. In the frequency domain, the error in the estimates becomes quite clear (see Figure 4-15)

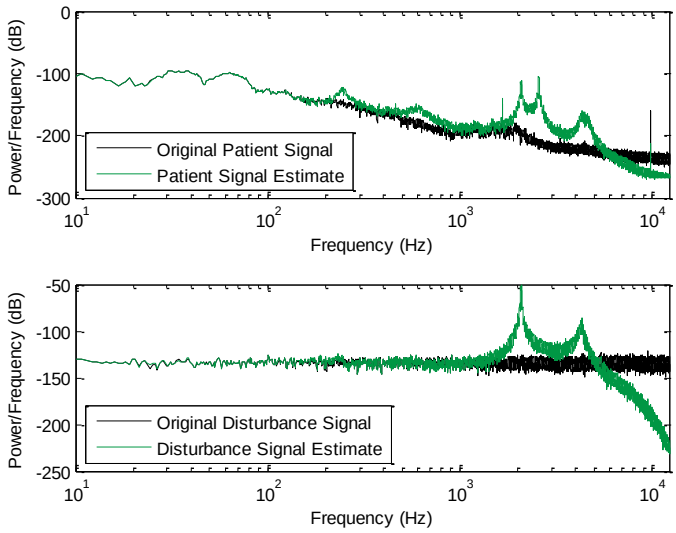

Figure 4-15: Simulated dual-piezo sensor system estimated patient input signal

However, the frequency response data suggests that the quality of the low frequency signal estimates is quite good. If the signals are filtered to remove all the extraneous

components above the desired auscultation signal, the following estimates are obtained (see Figure 4-16 and Figure 4-17)

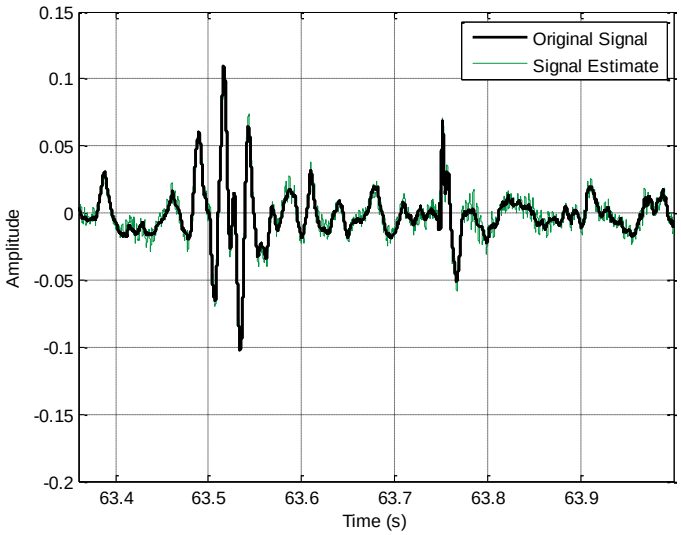

Figure 4-16: Simulated dual-piezo sensor system estimated patient input signal after filtering

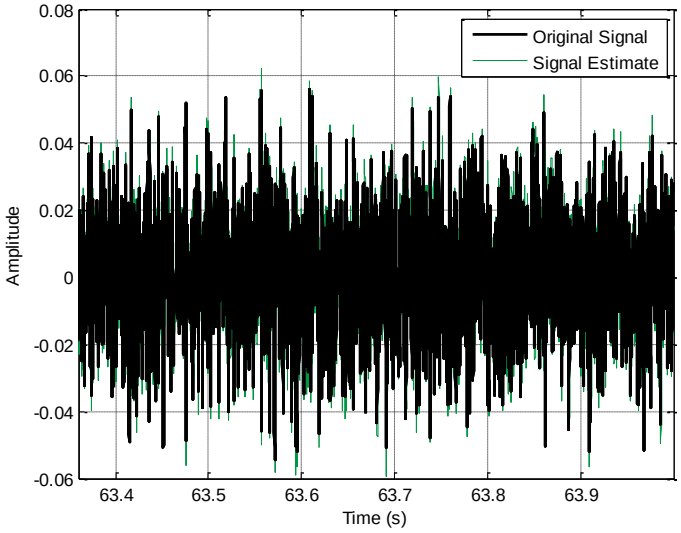

Figure 4-17: Simulated dual-piezo sensor system estimated disturbance input signal after filtering

In this frequency range, the estimates closely match both the desired heart sound and the broadband disturbance. The high frequency error in the signal estimates before filtering can be partially attributed to errors in the derivative approximations used in the algorithm. Repeating the simulations with exact derivatives, a high fidelity estimate is obtained for both inputs across the entire frequency range. By carefully selecting the observer gains, it is possible to improved performance may be obtained. Specifically, by adjusting the cost function used in the LMI solver to account for derivative estimation error, a more optimal gain for each observer can be identified.

4.3.4 *Experimental Results*

In order to experimentally verify the proposed design and algorithm on the physical system, a prototype of the proposed dual-piezo assembly was constructed and tested. Experimental testing was accomplished by stimulating the dual-piezo assembly with vibrational noise from both potential noise sources. For the generation of patient noise, a vibration shaker was used to generate a vibrational noise signal representative of a standard heartbeat. Traditionally, this noise would be coupled to the sensor via the patient's thorax. In a lab setting, this effect is most commonly reproduced through the use of a thorax simulator. For the initial investigation presented here, a thorax simulator has been omitted and the sensor assembly has been directly coupled to the shaker system. During each test, the housing for the first piezo assembly was bonded to the shaker via a foam disk with double-sided adhesive tape. The second unknown input, a disturbance due to physician handling noise, was created by rubbing and tapping on the top surface of the second (upper) piezo housing. Although a known reference disturbance signal was not used for this noise source, knowledge of the desired chest sound signal allows for a sufficient assessment of the algorithms performance.

In order to monitor the actual input acceleration experienced by the sensor assembly, a single axis accelerometer was rigidly attached to the shaker head. A National Instruments CompactRio chassis (NI cRIO-9074) with an analog input (NI 9205) and an analog

output (NI 9264) module has been used to generate and acquire the test signals. A constant sampling rate of 25 kHz has been used for all results presented.

Before presenting results in which an auscultation signal is used to drive the system, an initial white noise only patient input test was conducted with no added disturbance signal. The following measurements from each piezo sensor were obtained (see Figure 4-18).

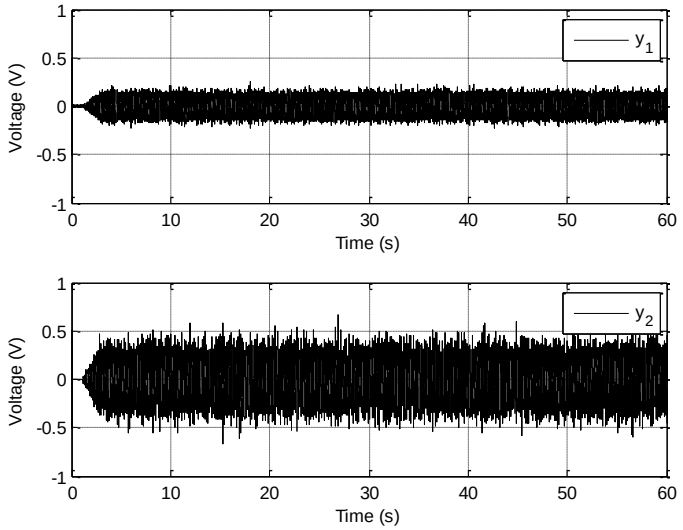

Figure 4-18: Dual-piezo sensor assembly measurement in presence of unknown vibrational inputs from bottom of assembly only

Since only a single input was present, after processing the data through the designed observer, the signal energy should all be attributed to a single input. More specifically, all the input should be identified as having originated from input 1 (i.e. u_1). As shown in Figure 4-19, in general this is confirmed in the processed data.

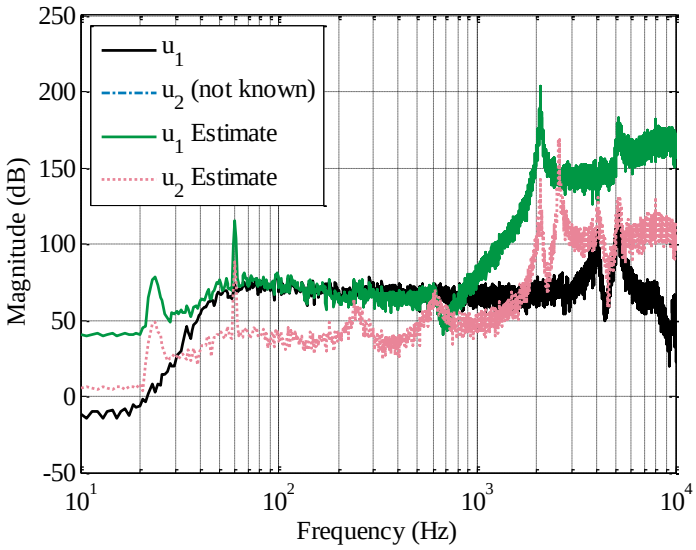

Figure 4-19: Frequency response of estimate of unknown inputs from a dual-piezo sensor assembly subject to only a white noise patient input

For frequency components below approximately 800 Hz, the signal estimate agrees well with the original input signal. In this same frequency range, the second input estimate has been reduced greatly. However, in both datasets it can be seen that considerable high frequency components exist which diverge from the desired signal. These errors are once again due to the numerical derivative approximation and the given choice of observer gains. Given that much of the estimate error lies above the frequency range of interest, it can be removed with filtering. After adjusting the responses, the time domain signal estimates shown in Figure 4-20 are obtained.

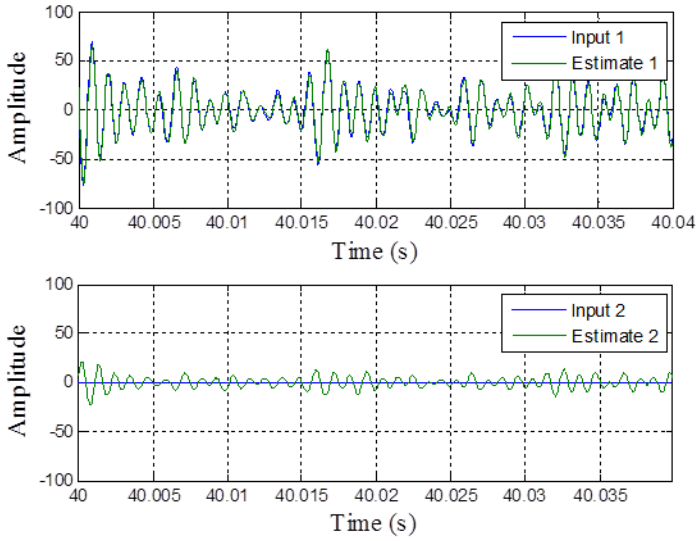

Figure 4-20: Time series data of estimate of unknown inputs from a dual-piezo sensor assembly subject to only a white noise patient input

The estimate of the first input agrees will with the actual input signal used for the experiment. Additionally, as desired, the amplitude of the second input estimate is considerably smaller.

To assess the performance of the observer when both inputs are present simultaneously, a test was conducted with both the known patient input and unknown tapping/rubbing on the top piezo assembly. The following measurement data was obtained (see Figure 4-21).

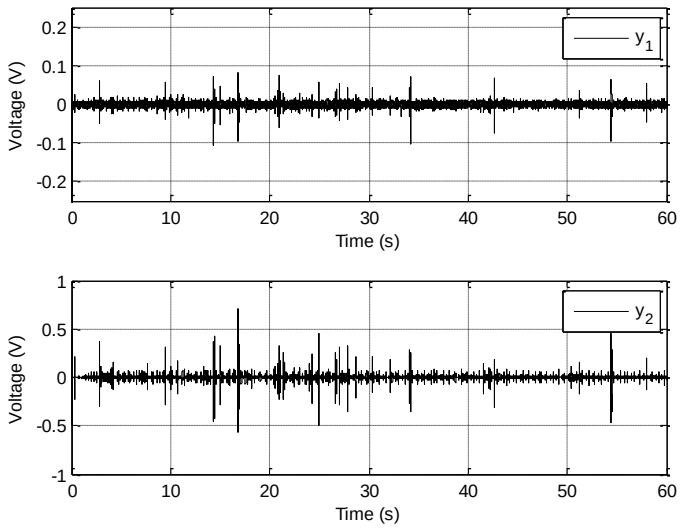

Figure 4-21: Dual-piezo sensor assembly measurements in the presence of unknown patient signals and disturbances

As would be anticipated, both measurements contain a mix of signals resulting from the unknown inputs acting on both sides of the device. The large spikes seen in both measurements are the result of tapping. The short periods of broadband noise (most clearly visible in the second piezo measurement) are caused by rubbing motions on the top of the sensor assembly.

After running the measurement data through the designed observer, the following estimates were obtain for both the unknown patient and unknown disturbance input signals (see Figure 4-22)

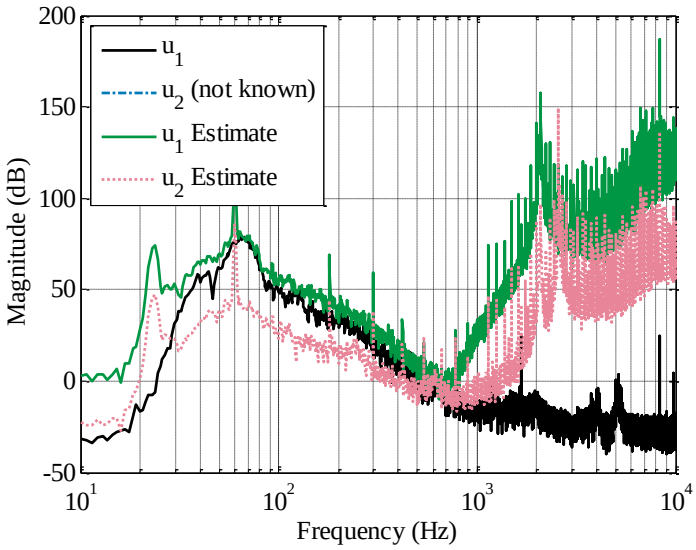

Figure 4-22: Frequency response of estimate of unknown inputs from dual-piezo sensor assembly in the presence of unknown patient signals and disturbances

As shown in the case of only a single unknown input, the high frequency estimates deviate largely from the desired signals. However, the energy due to the patient input signal (heart sound) is properly estimated to be from the first input.

In the time domain, the estimates appear as follows (see Figure 4-23)

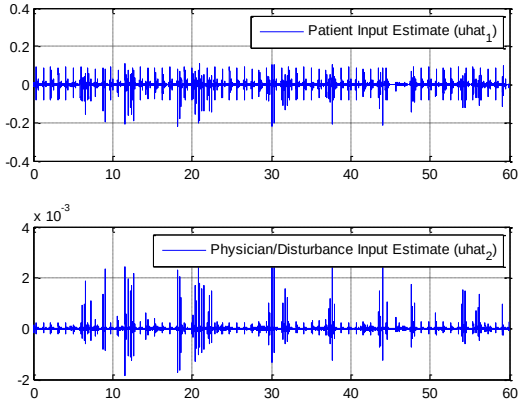

Figure 4-23: Time series data of estimate of unknown inputs from a dual-piezo sensor assembly in the presence of unknown patient signals and disturbances

As shown, much of the desired heart signal has been recovered. However, not all portions of the disturbance input have been successfully removed. Below 2kHz, this is explained due to small inaccuracies in the model estimate. Conducting smaller scale testing on only the preamplifier circuits, it was possible to accurately estimate the unknown inputs to each by using the proposed algorithms. This confirms that the errors are due to the mechanical model of the stethoscope (or that of the piezoceramic). By refining the initial dual-piezo assembly model to more accurately capture these underlying dynamics, it is anticipated that greater performance can be achieved.

4.4 CONCLUSIONS

Existing approaches to minimize the effect of disturbances caused by a physician during auscultation have been focused on passive improvements to the design. These methods attempt to isolate the transducer from such input signals and dissipate their energy prior to reaching the measurement sensor. Depending on the nature of the design, this isolation may not achieve sufficient noise reduction without compromising the device's sensitivity to patient signals. Using an unknown input observer design based on a model of how these interference signals reach the sensor, their effects can be removed digitally.

Given an original dynamic model, it has been shown that an inverse dynamic system can be constructed to relate measurement signals to estimates of the original system inputs acing on the system. In order to remove the errors due to unknown initial conditions a system observer based on the inverse dynamics has been derived. As an alternate approach, an additional observer design has been presented which does not rely on the system inverse model.

The performance of both system estimate architectures has been demonstrated on a simplified system in simulation. The use of numerical differentiation required within each algorithm degrades the estimate performance in the high frequency range, but low frequency estimates demonstrate a high level of performance.

A duel piezo sensor assembly has been constructed to investigate the performance of the algorithms on the stethoscope application. With simulation results, it is shown that successful disturbance rejection is possible up to approximately 1000Hz. With additional refinement of the observer gains, it is likely that this range can be extended.

Experimentally, the algorithm performance has been tested on the physical dual-piezo assembly. The inverse system can successfully attribute signal energy to the respective inputs, but errors in the phase of the original model compromise its performance. By refining the model of the new assembly, the estimates produced by the algorithms can be improved.

Overall, it has been demonstrated that directional disturbance estimation is possible, provided that a sufficiently accurate model of the system dynamics is obtained. Using this approach, it is feasible that the unwanted effects of disturbances caused by the physician can be reduced while providing a high quality estimate of the original auscultation signal. This technology can improve the stethoscope's performance and generally improve the quality of patient examination possible in a wide variety of environments.

CHAPTER 5:

ACTIVE NOISE CANCELLATION

5.1 MOTIVATION

Since its advent, the design of stethoscopes has gradually advanced to improve the signal to noise ratio encountered during normal use. Most recently, electronic stethoscopes have been developed to further amplify the signals of interest. Due to its versatility in clinical diagnostics, the stethoscope is commonly used by medical practitioners in a wide variety of environments. In many of these settings, auscultation is not possible due to high levels of ambient noise. This problem is particularly severe during patient transport where noise levels are commonly well in excess of 75 dB.

It is possible that with sufficient information about the nature of the noise in these environments, signal processing methods may be employed to improve signal quality. Specifically, if access is made available to a reference sensor which contains information about the noise, active noise cancellation may be possible. If the environmental noise and its propagation path are not known a priori, an adaptive filter architecture must be used. By this method, the noise corruption can be estimated in real-time and removed from the measured auscultation signal.

5.2 ENVIRONMENTAL NOISE CHARACTERIZATION

To better understand the characteristic high noise environments in which stethoscopes are commonly used, extensive field testing has been conducted. The testing provided information about the severity and nature of the ambient noise. By identifying the source of the noise and its effect on auscultation, it was possible to develop methods by which this noise can be mitigated.

5.2.1 *Stethoscope Instrumentation*

A pair of modified electronic stethoscopes has been designed to enable the collection of data about the ambient environment. Specifically, modified 3M™ Littmann® Model 3200 Electronic Stethoscopes have been developed to gather data for characterization of both the ambient acoustic and vibratory conditions during routine auscultation. A LabVIEW™ program was designed in conjunction with the test unit to enable high speed data capture in a mobile test environment. The program was specifically designed to index and save test data such that it was made available for detailed off-line analysis.

Prior to development of the first generation test units, it was concluded that in a given environment both the acoustic and vibrational characteristics are of interest. The sensor included in the commercially available Model 3200 stethoscope is a small flexible disc piezo-ceramic transducer. The Ø15mm sensor is centered in the face of the device in a small metal housing [87]. Using the stethoscope's built in electronic filters the device is capable of amplifying sounds from 20 – 2000 Hz [88]. When coupled to a patient's chest, the sensor responds to small variations in pressure and produces a corresponding voltage signal. These variations can be caused by both acoustic waves and physical vibrations. Therefore, both forms of ambient noise have the potential to drastically mask the desired auscultation signal.

Without having sufficient preliminary results available to indicate the general intensity or frequency content of the ambient conditions in the environments of interest, each test unit was designed to accommodate a wide range of testing conditions. In order to account for the scenario of varying sound pressure levels on a given face of the stethoscope, an evenly spaced radial arrangement of microphones was selected for one of the two test units. With this configuration, it is possible to identify if the noise corruption of the primary transducer exhibits any higher levels of correlation to a specified direction over another. In place of the radially configured microphones, the second test device featured a single internal MEMS microphone. The location of this microphone was selected to determine the level of acoustic energy that reaches the internal cavity of the device.

The design process required the development of multiple iterations of both test units. The device with a MEMS microphone was carefully configured to add the sensor without substantially altering the original internal configuration of the device. After the first iteration of the radial microphone design, the unit was improved to make it more compact. The new design helped the unit conform to the original fit and form of the unmodified 3M™ Littmann® Model 3200 Electronic Stethoscope (see Figure 5-1).

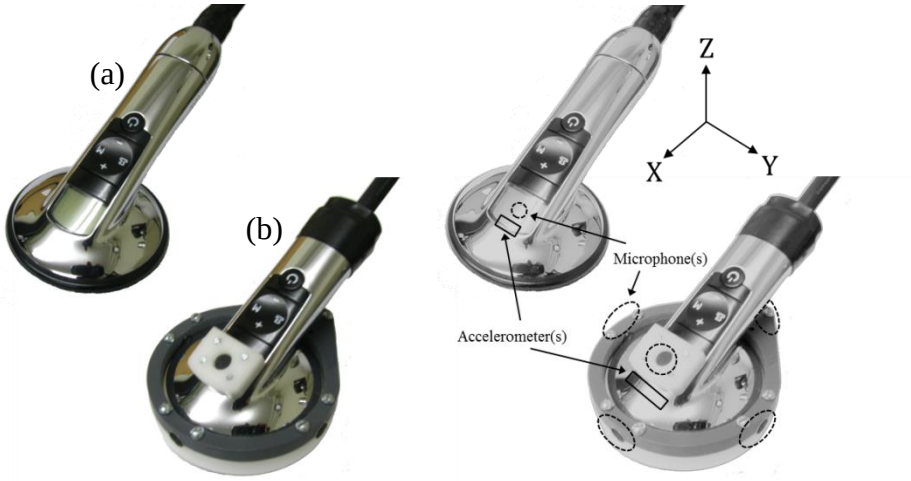

Figure 5-1: Modified stethoscope test units with (a) MEMS microphone and 3-Axis accelerometer and (b) omnidirectional microphones and z-axis accelerometer

As can be seen in the schematic of the sensor placement on each device, the first test unit (Device A) has been reconfigured with an internal MEMS microphone and a 16g 3-axis accelerometer. The second test unit (Device B) is another original stethoscope that has been retrofitted with five microphones (Front, Back, Left, Right, and Top) and one accelerometer. The microphones have been rigidly secured to the outside of the chestpiece housing via a hard plastic mounting ring. The 3g single-axis accelerometer has been rigidly attached inside the chestpiece and aligned with the original stethoscope piezoelectric sensing element. For both units, the accelerometer was included specifically to provide data that could demonstrate the level of correlation between the vibrations transmitted through the patient and the piezo transducer output. In addition to the hardware modifications visible in the figures provided, for Device B the original circuit

board provided in the stethoscope has been replaced with a pre-amplifier circuit necessary for the microphones. On both devices, the built-in piezo electronic filtering was disabled. This made it possible to acquire signals with frequency components outside the range of the pre-defined stethoscope filters.

In conjunction with the test unit development, a program was developed in LabVIEW™ to enable high-speed capture of the analog signals from the piezo and additional reference sensors. Due to the known high frequency range of the environments under investigation, it was necessary to design the program with sufficiently high sampling rates. Accordingly, the final program was capable of recording up to 12 input channels with a sampling rate of 50 kHz. In addition to indexing and storing each dataset, the program allowed the test administrator to document and store pertinent information regarding the test conditions.

5.2.2 *Measurement of Helicopter Noise Characteristics*

As previously discussed, the versatility and portability of the stethoscope has motivated its use by medical personnel in a wide variety of environments. Given its previously documented status as the harshest of such environments, the Sikorsky UH-60 helicopter (see Figure 5-2) was selected as the primary test environment for further investigation.

Figure 5-2: UH-60A Black Hawk helicopter on a medical mission [89]

With the assistance of the U.S. Minnesota Army National Guard, extensive testing was conducted on the UH-60 “Black Hawk” both while idling on the ground and during

routine flight maneuvers. In order to enable successful comparative characterizations, additional testing was performed in less harsh environments (i.e. in the lab and during ground transport). These other tests allow for a broad characterization of the general environments in which the stethoscope is used. Additionally, they establish a proper framework with which to highlight the severity of the ambient conditions present during helicopter transport.

For ground transport testing, a passenger van was used in place of an ambulance. Choosing to conduct testing without the use of a siren, it was anticipated that the type of vehicle was less critical than the type of roadway conditions. Therefore, testing was conducted on both smooth (e.g. paved) and rough (e.g. gravel) roads.

For a baseline comparison, tests conducted in each environment were repeated with an unmodified 3M™ Littmann® Model 3200 Electronic Stethoscope. Also, in order to isolate noise sources caused by handling of the test devices, pure ambient sensor readings were also obtained. During each field test, an ambient microphone was suspended in the vehicle and a 3-axis accelerometer was mounted to the vehicle frame. Specifically, the ambient accelerometer was mounted directly to the vehicle on the floor immediately below the microphone. Shown in Figure 5-3 is a schematic of the Black Hawk helicopter's internal cabin configuration. The location of both ambient sensors has been indicated with an "X".

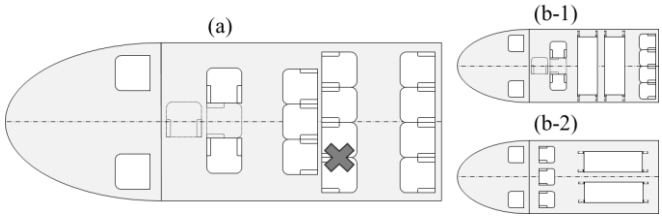

Figure 5-3: UH-60 Black Hawk helicopter ambient sensor position in (a) passenger and (b) litter configurations (not drawn to scale)

Also provided in the figure are alternate configurations of the UH-60 Black Hawk helicopter. Although multiple different internal cabin configurations are possible [90], the

ambient sensor location coincides closely to the general litter (i.e. patient) position during transport. Thus, these sensors provided data characteristic of the vehicle's inherent operating noise conditions as they affect a medic's interaction with a patient.

After having gathered sufficient data from field testing, it was possible to accurately characterize the environments in which the stethoscope is intended for use. The primary analysis was concerned with determining the following:

- Ambient acoustic noise levels
- Ambient vibration levels
- Ambient noise frequency content
- Level of corruption caused by ambient noise
- Primary contributor of corruption

This analysis is necessary for future design considerations to help improve the stethoscope's performance in high noise environments.

5.2.3 *Environmental Noise Levels*

The ambient acoustic microphone and vehicle mounted 3-axis accelerometer used for testing provided data containing the general environment characteristics desired. From this data, it was observed that the acoustic noise levels present in the UH-60 Sikorsky Helicopter were substantially higher than those recorded in all other test environments. In order to numerically evaluate and compare these levels, the average and peak sound pressure levels (SPL) were evaluated for all data sets available. The instantaneous sound pressure level, $L_p[n]$, and equivalent continuous A-weighted sound pressure level, L_{eq}, in decibels are given by

$$L_p[n] = 20\,log_{10}\left[\frac{p_A^2[n]}{p_0^2}\right] \tag{5.1}$$

$$L_{eq} = 20\,log_{10}\left[\frac{1}{N}\sum_{n=1}^{N}\frac{p_A^2[n]}{p_0^2}\right] \tag{5.2}$$

where $p_A[n]$ is the measured instantaneous A-Weighted sound pressure level in Pascals, p_0 is the reference sound pressure level of 20 μPa, and N is the measurement samples for

a given test. The equivalent continuous sound pressure level is used here as it provides a measure of the average acoustic energy.

Figure 5-4 below summarizes the sound pressure levels observed in each test environment.

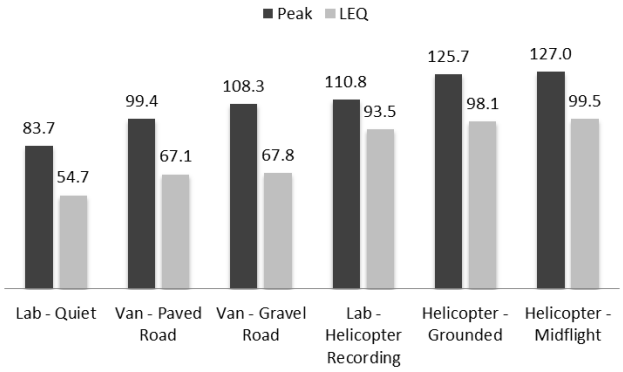

Figure 5-4: Measured sound levels (dB) in patient transportation environments

Reported in the figure are the mean values from each test condition. As anticipated, the helicopter exhibits the highest noise level with peak noise levels in excess of 125 dBA. More importantly, the equivalent continuous sound pressure levels encountered in the helicopter were approximately 100 dBA (more than 3000 times the sound level of chest sounds at the skins surface)! Even without further analysis, this begins to illustrate the severity of the challenge in conducting successful auscultation during emergency helicopter patient transport.

In addition to high acoustic noise levels, the data demonstrated that significant vibrations were present during operation of the helicopter both while grounded and mid-flight. These vibrations can be attributed to constant rotation of the helicopter rotor—primary moving mechanism of the helicopter. As the rotor turns, it produces an array of structure borne vibrations that propagate through the frame of the aircraft. For each dataset, both the peak and root mean square (RMS) acceleration levels were calculated. The RMS acceleration, a_{RMS}, is given by

$$a_{RMS} = \sqrt{\frac{1}{N}\sum_{n=1}^{N} a^2[n]} \tag{5.3}$$

Figure 5-5 and Figure 5-6 below summarize the acceleration levels observed in each test environment.

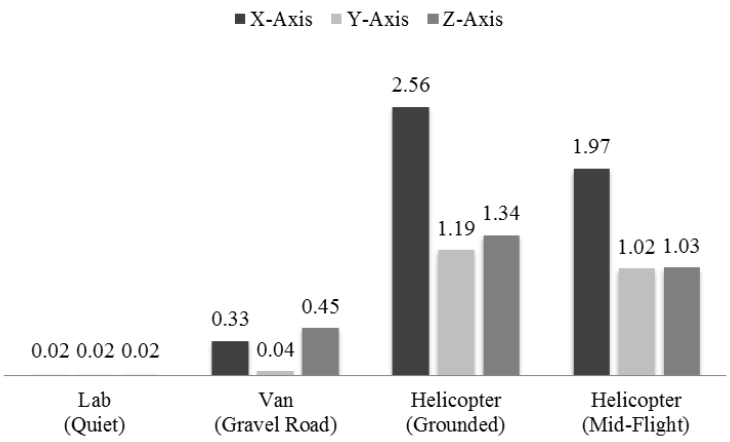

Figure 5-5: Measured peak acceleration levels (g) in patient transportation environments

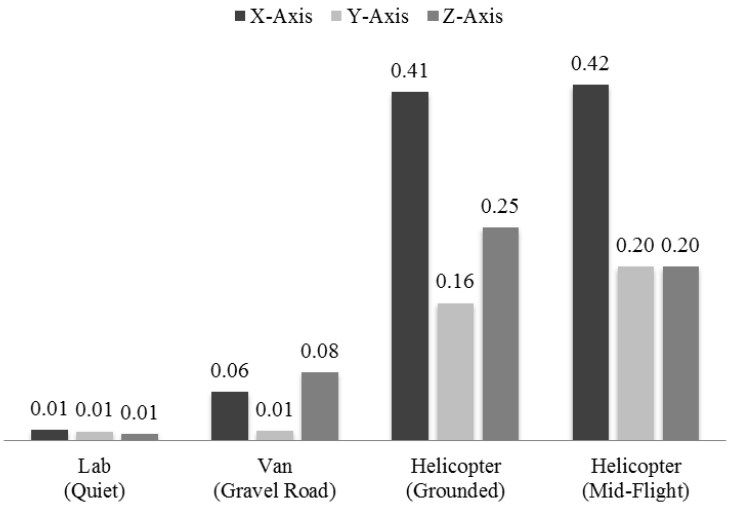

Figure 5-6: Measured RMS acceleration levels (g) in patient transportation environments

As anticipated, the vibrations in the helicopter have significant content along all three axes. Although the testing conducted in the van provides some acceleration data, the peak acceleration levels due to vibrations of the helicopter are more than five times higher.

Thus, if the vibrations are found to be a large contributor to the stethoscope's piezoelectric sensor's disturbance, this will need to be considered when designing a device capable of operating in a helicopter. Similar to the acoustic noise levels observed, it is important to note that these vibrations are present not only while the helicopter is mid-flight, but also while the helicopter is idling on the ground. As long as the rotor is under power, the cabin of the helicopter appears to vibrate heavily.

5.2.4 *Environmental Frequency Content*

As arguably the harshest clinical environment in which a stethoscope is commonly used, the analysis that follows will focus only on the data corresponding to helicopter testing. Here, we have assumed that the rich acoustic and vibrational signatures exhibited by this environment present the worst case scenario for successful auscultation. Thus, a design solution that overcomes the current limitations of stethoscope use on a helicopter will be capable of operating in less severe environments.

In addition to the overall amplitude, one of the key characteristics of the ambient noise is its power spectral density—the power of the signal at each frequency. Here, we have chosen to use Welch's method for estimating the power spectral density.

The data reveals that there is considerable frequency content in the low frequency range. Given that standard auscultation signals consist primarily of low frequency content, this provides a very significant technical challenge for stethoscope designs. Provided below is the power spectral density estimates from the ambient microphone data (see Figure 5-7).

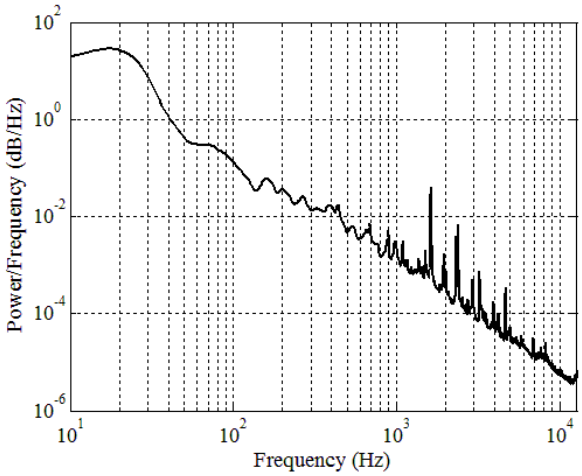

Figure 5-7: Measured power spectral density of Black Hawk helicopter acoustic noise

Although this estimate has been calculated from a single test, it is characteristic of the entire data set available. In order to better understand the significance of the frequency content observed, we can compare it to the frequency content contained in data from a heart sound recording obtained in a quiet environment. Figure 5-8 shows the signal-to-noise ratio (SNR) in the low frequency range around which typical heart sounds occur. The data presented has been divided into 3rd Octave Bands.

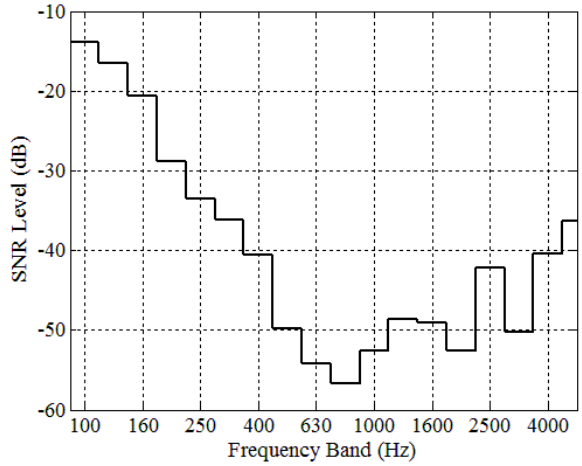

Figure 5-8: Observed signal-to-noise ratio of heart sounds relative to helicopter noise per third octave band

It is clear from the figure that although the SNR is worse in some frequency bands more than others, it is clearly unfavorable for successful auscultation across all frequencies of interest.

Along with examining the acoustic frequency content, it is informative to study the power spectral density estimates of the accelerometer X, Y, and Z-Axis data (see Figure 5-9, Figure 5-10, and Figure 5-11 respectively).

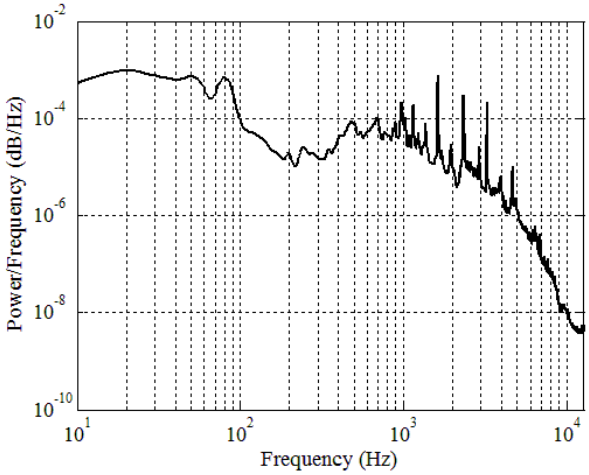

Figure 5-9: Measured power spectral density of Black Hawk helicopter vibration (X-Axis)

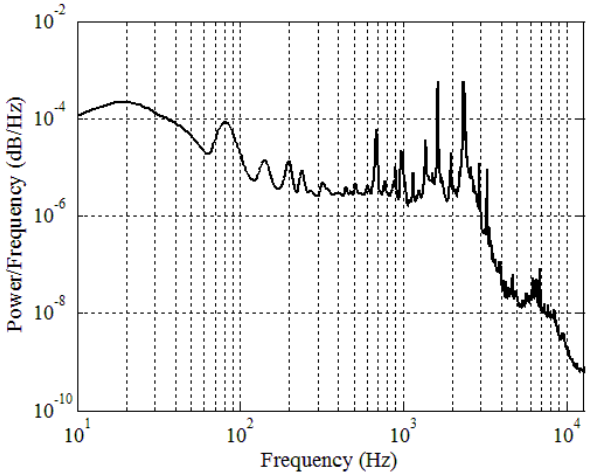

Figure 5-10: Measured power spectral density of Black Hawk helicopter vibration (Y-Axis)

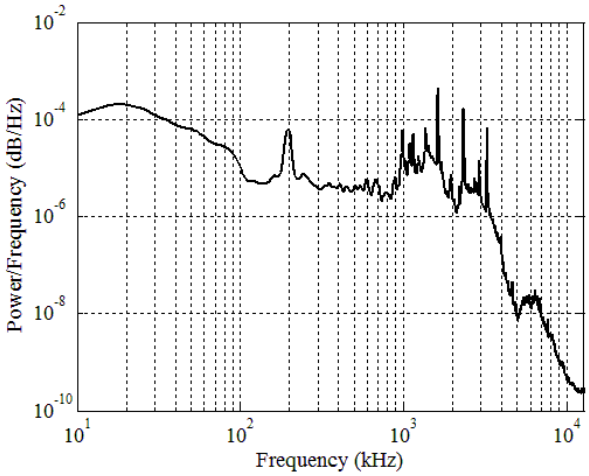

Figure 5-11: Measured power spectral density of Black Hawk helicopter vibration (Z-Axis)

These power spectral density estimates reveal that significant low frequency vibrations exist. Specifically, below 500Hz the frequency spectrum shows elevated vibrational noise levels for all three axes.

The data presented confirms that both the ambient vibrations and ambient acoustic noise corrupt the signal obtained by the stethoscope's sensing element. Subsequently, it is necessary to characterize the relative noise level when compared to the desired auscultation signals. This is most simply captured by calculating the SNR as the ratio of the desired signal root-mean-square (RMS) power to the noise RMS power. Using data that has been acquired, the SNR can be estimated by comparing the signals obtained during routine auscultation in a quiet environment with those obtained in the helicopter. The SNR is given by the following equation,

$$SNR = \frac{P_{signal}}{P_{noise}} \tag{5.4}$$

where P_{signal} and P_{noise} are quantities proportional to the power of the pure auscultation signal and the pure noise signal respectively. If we denote $p[n]$ as the instantaneous output from the piezoelectric sensor for a given test N samples long, then the signal measure, P, for that test is given by

$$P = \frac{1}{N}\sum_{n=1}^{N} p^2[n] \tag{5.5}$$

Applying this equation to the pure auscultation signal and the pure noise signal, P_{signal} and P_{noise} were calculated to be 8.60 $mV^2/sample$ and 55.80 $mV^2/sample$ respectively. Accordingly, by Eq. (5.4), it is estimated that the SNR with the electronic stethoscope tested is approximately 0.015.

The poor SNR indicates that the noise corruption has enough power to completely mask the desired auscultation sounds. This is most clearly demonstrated by observing time waveforms of heart sound data from a healthy adult male subject acquired in both a quiet lab environment and in a mobile Black Hawk helicopter. With the first dataset corresponding to heart sounds acquired in a quiet environment, it is possible to clearly distinguish the periodic waveform created by the first and second heart sounds—closing of the atrial ventricular and semilunar valves respectively (see Figure 5-12).

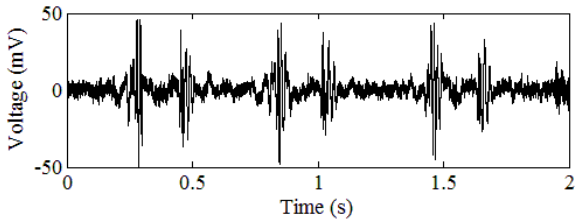

Figure 5-12: Measured piezo signal of heart sounds in a quiet lab

This can be sharply contrasted with data acquired during a routine helicopter flight (see Figure 5-13).

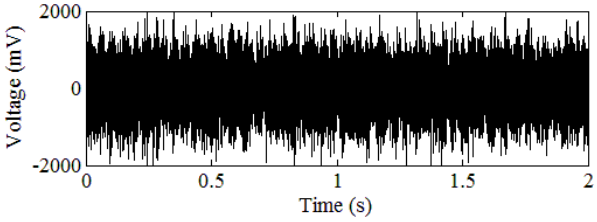

Figure 5-13: Measured piezo signal of heart sounds in a helicopter during flight

Here, it is evident that the even the most basic shape of the heart sounds is indiscernible amongst the high levels of ambient noise. Similarly, by looking at the frequency content of each signal as a function of time (i.e. its spectrogram), it is possible to note the large difference in measured signals in the quiet environment to that of the helicopter environment (see Figure 5-14 and Figure 5-15).

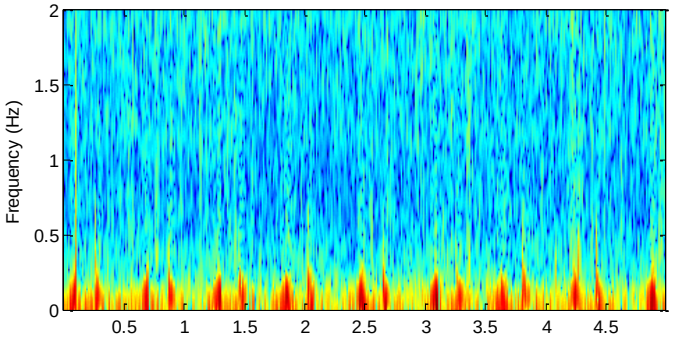

Figure 5-14: Spectrogram of measured heart sounds in a quiet lab

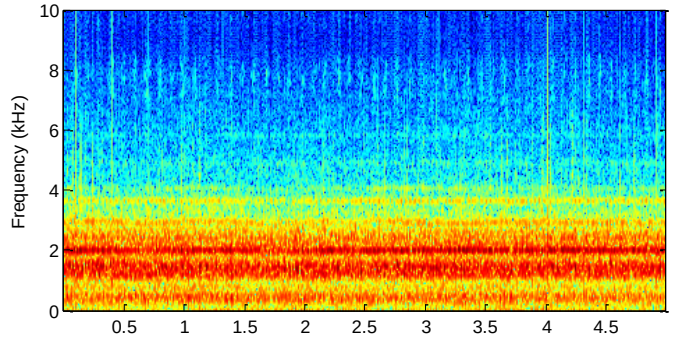

Figure 5-15: Spectrogram of measured heart sounds in a helicopter during flight

In addition to demonstrating that the heart sound is completely undetectable in the presence of the helicopter noise, the spectrogram reveals that the noise field is approximately constant—the frequency content of the noise does not vary considerably over time. This improves the prospect of successfully applying active noise cancellation methods.

5.2.5 *Primary Noise Corruption Source Identification*

After identifying the type, intensity, and spectral content of the noise present in a helicopter, the next objective was to characterize the nature of the relationship between these ambient noise sources and the noise that is directly sensed by an electronic stethoscope. Once a stethoscope has been placed against the skin of a patient's chest, back, etc., the path of each noise source drastically changes. Taking a closer look at the usage conditions, the following acoustic noise paths can be identified:

- A_1: Direct leakage at the user's ear
- A_2: Leakage through the stethoscope head, tubing, or binaurals
- A_3: Reflection and/or propagation along the chest of the patient and into the stethoscope

Similarly, two primary vibrational noise paths can be identified:

- V_1: Transmission through the patient and into the device
- V_2: Transmission through the physician/user and into the device

Each different noise path (acoustic and vibrational) has been illustrated in the schematic below (see Figure 5-16).

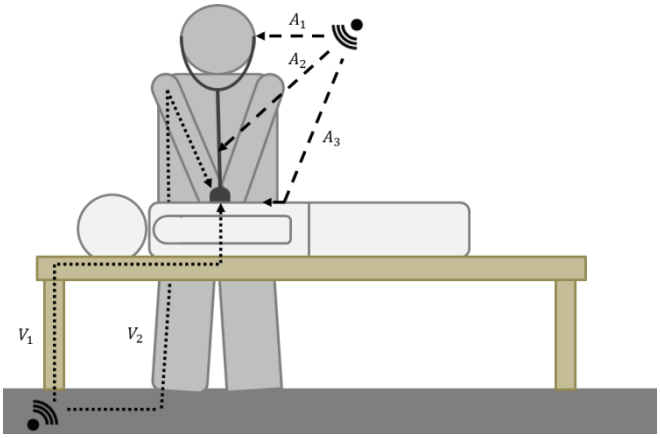

Figure 5-16: Schematic of environmental noise transmission paths

As the noise travels to the sensing element via these various paths, it undergoes distinct transformations. Depending on the nature of the transfer function and the ease with which noise is transmitted via a given path, each source may contribute differently to the specific noise corruption that has been found to interfere with auscultation. Although it is informative to understand all forms of noise irrespective of their contribution factor, in order to make advances in stethoscope design to better enable auscultation in such high noise environments, it is beneficial to narrow the investigation to only those noise sources that dominate corruption of the auscultation signal. In order to assess which noise sources required further consideration, the cross-correlation between the reference sensors on the stethoscope and the signal from the primary stethoscope sensor were calculated. The cross-correlation provides a quantifiable measure of how similar two waveforms are to one another. In this way, the reference sensors with higher correlation to the primary sensor signal can be identified as the larger contributors to corruption of the auscultation signals. Table 5-1 and Table 5-2 below summarize the cross-correlations calculated for the reference microphones and accelerometers respectively.

Table 5-1: Microphone and primary sensor signal correlation during helicopter flight

Device	Sensor Location	Raw Cross-Correlation ($x10^3$)
A	Internal	6.8
	Front	1.6
	Back	6.8
B	Left	3.1
	Right	4.6
	Top	7.8

Table 5-2: Accelerometer and primary sensor signal correlation during helicopter flight

Device	Axis	Raw Cross-Correlation ($x10^3$)
	X-Axis	9.0
A	Y-Axis	4.7
	Z-Axis	19.4
B	Z-Axis	23.9

For the microphone data, the highest cross-correlation values are seen to be with the Top, Back, and the internal MEMS microphones. This is most likely explained simply by the damping of signals obtained by the other microphones due to obstruction caused by placement of the test administrators hand during testing.

Each of the Z-axis accelerometers exhibits high levels of correlation with the primary piezoelectric sensor signal. When compared with the microphone, the correlation between the accelerometers and primary signal are nearly five times stronger than that between any one of the microphones and the primary signal. This suggests that the highest level of corruption to the auscultation signal obtained by the stethoscope's sensing element is caused by acceleration (i.e. vibrations) along the primary axis of the device (the Z-axis).

5.3 SIMULATED ACTIVE NOISE CANCELLATION

Based on the acquired information about the noise characteristics in a field environment, it is possible to assess methods by which this noise can be mitigated. Before beginning to investigate the performance of potential active noise reduction techniques, it is necessary to first present an overview of active noise cancellation and the surrounding principles.

5.3.1 *Least Mean Squares and Normalized Least Mean Squares Adaptive Filter*

Active Noise Cancellation refers generally to a class of algorithms relied on for the purpose of noise reduction. Although a wide variety of methods have been developed, each uses a primary signal and one or more noise reference signals. Here, we will focus on the case of a single reference sensor as shown in Figure 5-17.

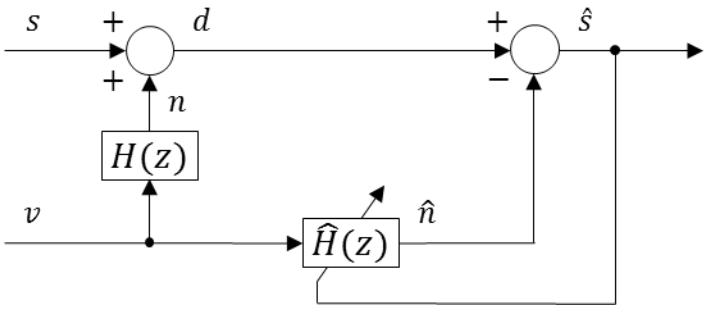

Figure 5-17: Active noise cancellation block diagram

As seen in the figure, the basic ANC model assumes that the primary signal, d, consists of the desired signal, s, and the transformation, n, of some additive noise, v, where the signal and noise are uncorrelated. Although in general the transformation of the noise can be both nonlinear and time-variant, the model assumes that this path is approximately linear. Therefore, by passing the noise reference input, v, through an estimate of this transformation, it is possible to create an estimate, $\hat{n}$, of the noise that is corrupting the desired signal contained in the primary input, d. Subsequently, by subtracting this estimate from the primary signal, an estimate, $\hat{s}$, of the desired signal can be generated. The key element to most ANC algorithms is the method employed to estimate this transformation. This is the distinguishing feature for most variations presented in literature.

Traditionally, a feedforward FXLMS adaptive algorithm has been relied on for many active noise cancellation applications. This is typically necessary due to the unknown secondary path between the control output and residual error. However, by using a fully electronic stethoscope, the secondary path is eliminated and the traditional Least Mean Square (LMS) or Normalized Least Mean Square (NLMS) can be employed. In this configuration, the primary input and noise estimate can be combined digitally whereby avoiding secondary path errors. Thus, the original ANC model presented in Figure 5-17 remains valid.

In the absence of secondary path errors, the performance of the filter is governed primarily by the quality of estimate, $\widehat{H}(z)$, for the original noise transformation, $H(z)$. If this transformation were known a priori, the solution would be trivial. However, this is typically a function of the specific operating conditions. For both the LMS and NLMS algorithms, the transformation is estimated by an N-tap transversal filter. For each, the tap-weights of the filter are estimated recursively based on instantaneous estimates of both the input signal autocorrelation and the cross correlation between the input and reference signal. If both the primary and noise signals are stationary, this will converge to the Wiener solution. The resulting equations governing the operation of the LMS algorithm can be seen as follows [91]:

$$\hat{n}(m) = \sum_{i=0}^{N-1} w_i(m)\, v(m-i) \tag{5.6}$$

$$\hat{s}(m) = d(m) - \hat{n}(m) \tag{5.7}$$

where the adaptive filter weights are updated with the following recursive equation

$$w_i(m+1) = w_i(m) - \mu\, \hat{s}(m)\, v(m-i) \tag{5.8}$$

for all $0 \leq i \leq N$. For the standard LMS algorithm, a constant step size μ determines the stability, rate of convergence, and misadjustment of the adaptive filter. A known drawback of this approach is its sensitivity to the power of the reference input signal. Thus, the choice of an adequate learning rate, μ, that guarantees stability of the algorithm may be difficult [91]. Specifically, convergence can be guaranteed only when the step size μ obeys

$$0 < \mu < \frac{1}{\lambda_{max}} \tag{5.9}$$

where λ_{max} is the largest eigenvalue of the reference signal autocorrelation matrix. To address this issue, the NLMS algorithm has been proposed with the following weight update equation [92, 93].

$$w_i(m+1) = w_i(m) - \frac{\tilde{\mu}}{\sum_{i=0}^{k-1} |v(m-i)|^2}\, \hat{s}(m)\, v(m-i) \tag{5.10}$$

$$\mu[m] = \frac{\tilde{\mu}}{\sum_{j=0}^{N-1} |v[m-j]|^2} \tag{5.11}$$

for all $0 \leq i \leq N$. Here, the learning rate has been replaced by a normalized time-varying step size which is a function of both the constant $\tilde{\mu}$ and the squared Euclidian norm (i.e. power) of the reference signal. In addition to mitigating the gradient noise amplification problem due to large input signals, the NLMS algorithm may exhibit a potential faster rate of convergence over the LMS algorithm for both uncorrelated and correlated input data [92, 94].

For both the LMS and NLMS algorithms, convergence is governed largely by the quality of the reference input signal. Optimal performance requires the reference signal to be highly correlated to the noise source and entirely uncorrelated to the desired signal. If either condition is violated the filter performance can degrade substantially.

5.3.2 *Active Noise Cancellation with Field Test Data*

Using the field data acquired during routine helicopter flight, it was possible to assess the performance of the active noise cancellation algorithms with the available reference measurements. One limitation of interest for ANC is the presence of uncorrelated noise in either the error or reference inputs. An accepted measure to assess the level of uncorrelated noise is referred to as coherence. Given an input, x, and an output (or measurement), y, the coherence is given by

$$\gamma_{xy}^2(f) = \frac{|S_{xy}(f)|^2}{S_{xx}(f)S_{yy}(f)} \tag{5.12}$$

where S_{xx} , S_{yy} , and S_{xy} are the power spectral densities of x and y and the cross power spectral density of x and y respectively [95]. As a function of frequency, the coherence demonstrates the fraction of y that can be related to x by a linear transversal filter. If x and y are perfectly related by a linear, time-invariant filter, then their coherence equals one. Therefore, for ANC to be successful, a large coherence is required. This relationship has been extended to use the coherence function as an estimate of the expected noise reduction in decibels resulting from ANC [96]. Letting the noise measurement, v, and primary signal measurement, d, serve as the input and output signals respectively, the estimated attenuation is given by

$$A(f) = -10\log_{10}\left[1 - \gamma_{vd}^2(f)\right] \tag{5.13}$$

Therefore, by using this equation it is possible to analyze the expected performance of ANC using a given reference signal. This assessment has been conducted with the reference microphone and accelerometer data acquired during helicopter testing (see Figure 5-18 and Figure 5-19).

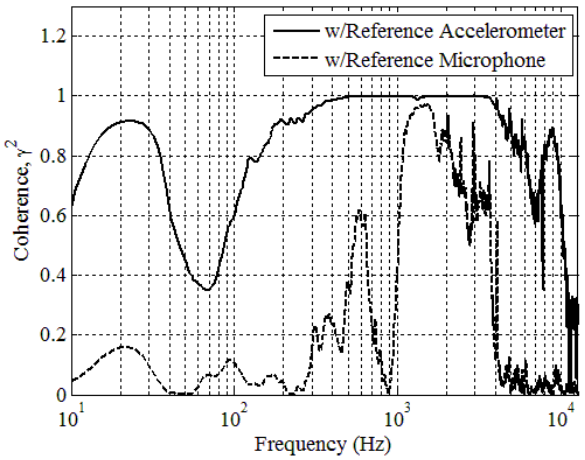

Figure 5-18: Reference microphone and accelerometer coherence with noise measurement at the stethoscope's primary piezo sensor

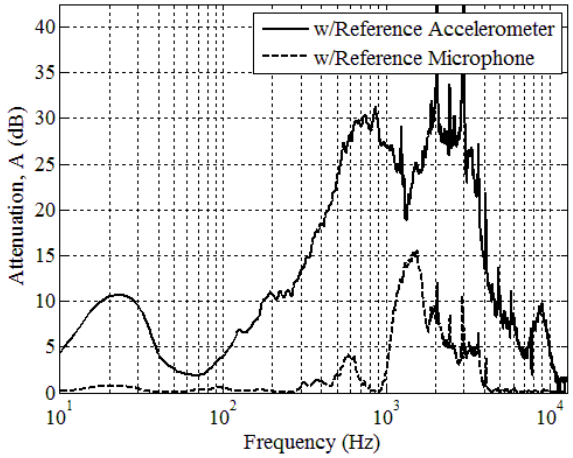

Figure 5-19: Estimated noise attenuation possible with active noise cancellation using the reference accelerometer and microphone signals respectively

Looking at the coherence in Figure 5-18, it is clear that the piezo signal is highly coherent with the accelerometer signal over a broad frequency range. Correspondingly, in Figure 5-19 the estimated attenuation demonstrates that by using an accelerometer based ANC system, considerable noise reduction can be achieved for a wide frequency range. Specifically, noise reduction is possible in a wider frequency range than has been demonstrated with the use of a reference microphone. As seen in Figure 5-19, there appears to be a slight drop in coherence between the accelerometer and piezo below 200 Hz. It is believed that by using a higher quality piezo and more carefully selecting the accelerometer position within the device this can be improved.

Analysis has been done on the effect of the signal-to-noise ratio as well as the effect of correlation between the reference sensors and the primary piezo signal. Objective measures of the ANC performance were calculated by implementing each algorithm on a mixed stethoscope signal. The signal was constructed by combining a pure heart sound recording (no noise disturbances) acquired with the stethoscope with a pure noise sound recording (no heart/lung sound). By using a known heart sound input, it was possible to compare the resulting estimate of the heart sound signal after active noise cancellation with the actual signal.

Using the method previously described, it was possible to determine the threshold signal-to-noise ratio for which the filter could accurately estimate the heart sound. This level is dependent on the reference sensor used. This dependence can be explained by the correlation level of the reference sensor to the input signal. For the quality of the reference accelerometer signal used in the initial investigation, it was concluded that the signal-to-noise ratio needs to be improved by at least a factor of three in order for the LMS filter to work as intended. Particularly good results are obtained when the signal-to-noise ratio is improved by a factor of ten. An example of the LMS filtering results using a reference accelerometer and an artificially improved signal-to-noise ratio can be seen in Figure 5-20.

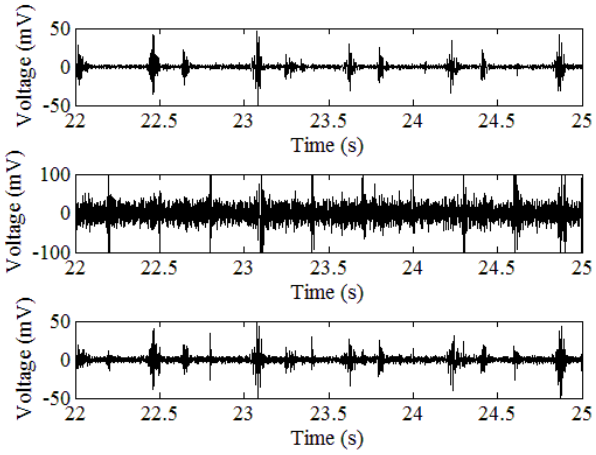

Figure 5-20: Accelerometer based ANC (a) desired original signal, (b) estimate after ANC with 0.015 input SNR, and (c) estimate after ANC with 0.154 input SNR

The filter accurately captures the characteristic peaks and valleys of the desired auscultation signal when the SNR is 0.154. This can be contrasted with the same analysis conducted with a reference microphone (see Figure 5-21).

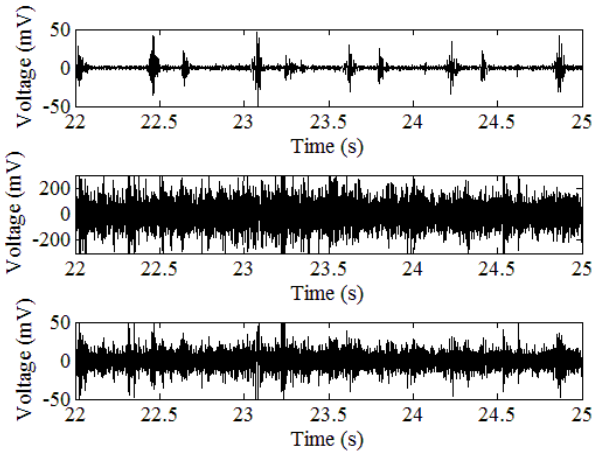

Figure 5-21: Microphone based ANC (a) desired original signal, (b) estimate after ANC with 0.015 input SNR, and (c) estimate after ANC with 0.154 input SNR

Here, it is clear that the low correlation between the reference microphone and the primary sensor prohibits the algorithm from accurately estimating the desired signal (both with and without an artificially improved SNR).

Understanding the limitations presented through this preliminary analysis, additional research was required in order to establish optimal reference sensor placement. Bearing in mind the higher correlation levels found for the accelerometer data, it is concluded that an accelerometer based ANC system will indeed outperform the results presented in literature using microphone based systems.

5.4 ACTIVE NOISE CANCELLATION EXPERIMENTAL RESULTS

5.4.1 *Experimental Test Platform*

Data from field testing clearly indicated that noise corruption during auscultation can be attributed to both air-borne acoustics and structural vibration. Thus, it is necessary to investigate the effect of noise contributions from each path. For this multi-path noise environment, a block diagram illustrating the signal paths for the original system and the ANC implementation is shown in Figure 5-22 below.

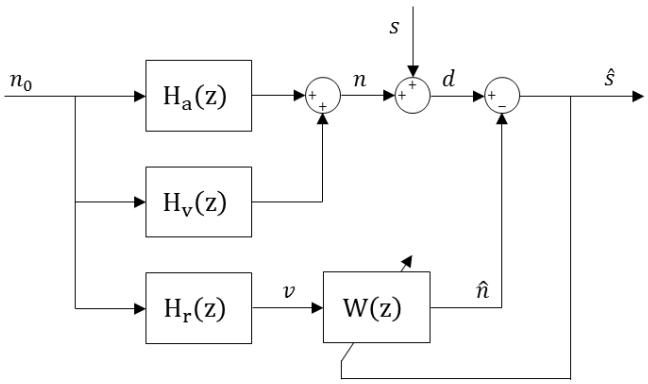

Figure 5-22: Dual noise path active noise cancellation block diagram

As shown in the figure, two independent noise paths have been identified for this application: (1) noise propagating acoustically through the environment to the sensor, H_a, and (2) vibrational noise traveling through the structure to the sensor, H_v. Collectively,

the sum of these two noise signals is regarded as the noise, n, which corrupts the desired signal. It is assumed that both noise components originate from the same source but undergo a different transformation (i.e. noise propagation path) prior to reaching the sensor. Although additional uncorrelated airborne and structure borne noise may exist in practice, for the purpose of this study they are assumed to be negligible and omitted.

In order to experimentally investigate the performance of the proposed active noise cancellation methods, a reliable experimental platform was required. For this purpose, a testbed was developed to provide acoustic and vibration stimuli representative of both ambient noise and patient auscultation signals.

The generation of patient noise was achieved by using a thorax simulator to create and transmit auscultation signals into the stethoscope. For the thorax simulator employed here, a Dayton Audio DAEXEXT weatherproof exciter has been imbedded into a Shore 10A Silicone rubber mold. By sending a voltage signal to the exciter, the thorax simulator is capable of reliably simulating chest sounds from 35-10,000 Hz. An illustration of the simulator assembly can be seen in Figure 5-23 below.

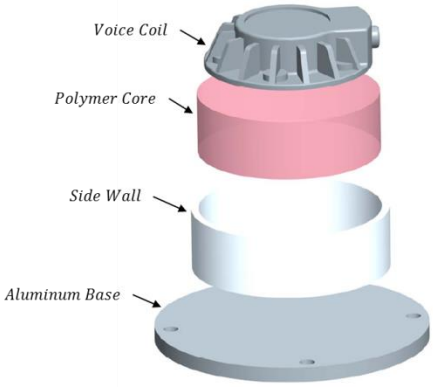

Figure 5-23: Thorax simulator configuration and assembly

When testing a stethoscope, the piezo sensor side of the device is placed on the surface of the thorax simulator. The nominal application pressure was held constant by allowing the stethoscope to rest using its own weight.

A Labworks ET-139 permanent magnet shaker was employed to generate the ambient vibration signal. Provided with a linear power amplifier (PA-138), the unit can deliver up to 17 lbf RMS random force in the frequency range from DC to 6,500 Hz. Additionally, the unit is capable of providing up to 20 g peak acceleration. The frequency range and acceleration levels are more than sufficient to accurately reproduce the desired vibration signal.

The ambient audio signal has been created by using a pair of Fostex PM0.5n speakers. Equipped with both a low frequency woofer and a high frequency tweeter, the speakers can deliver a flat frequency response (+/- 2dB) from 50 Hz to 20 kHz.

In order to provide a reliable reference signal of the ambient noise, the test platform has been fitted with both a reference accelerometer and microphone. The single-axis accelerometer (Measurement Specialties 805M1) is rigidly mounted to the base of the thorax simulator in-line with its active axis. This location was specifically selected because it provides a reliable measure of the vibration input provided by the shaker without being influenced largely by the patient sounds generated by the thorax simulator. The microphone (Knowles Electronics 21994-000) was suspended above the shaker assembly and positioned in-line with the speakers.

A schematic of the testbed with both input and output devices clearly identified can be seen in Figure 5-24.

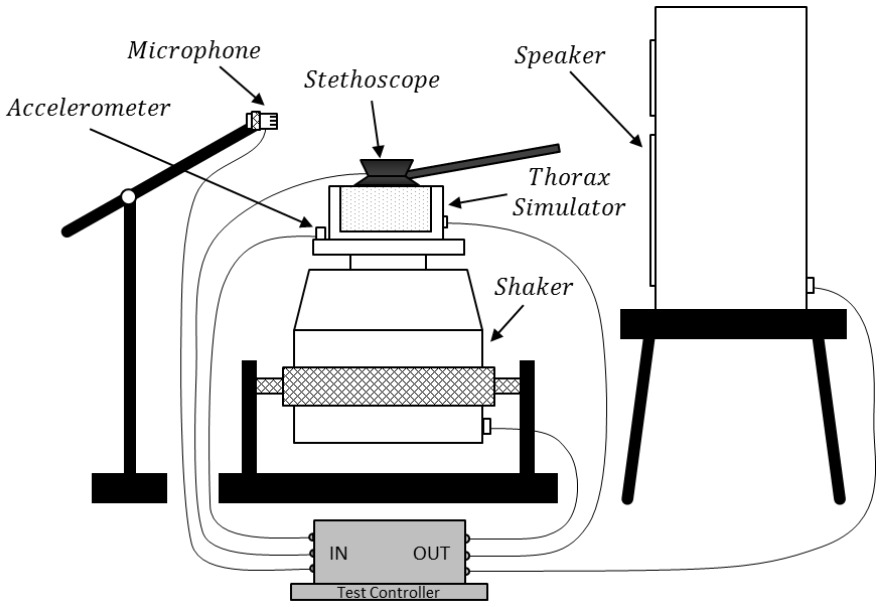

Figure 5-24: Schematic of active noise cancellation experimental testbed

As shown in the figure, a centralized test controller has been implemented to coordinate the input and output signals during each test. Specifically, a National Instruments CompactRio chassis (NI cRIO-9074) with an analog output (NI 9264) and analog input (NI 9205) module has been used to generate and acquire the test signals. A constant sampling rate of 25 kHz has been used for all results presented.

5.4.2 *Comparison of Accelerometer and Microphone based Active Noise Cancellation*

When comparing the performance of ANC using an accelerometer reference sensor to that obtained when using a reference microphone, the origin and transmission of the noise into the stethoscope transducer is critical. In order to demonstrate the relative effectiveness of each reference sensor and their dependence on the nature of the noise source, a benchtop experiment was conducted. The stethoscope was stimulated with white noise from both the speaker and shaker simultaneously. However, the power of the noise signal distributed to each was varied. When the majority of the noise was transmitted via the shaker, it would be expected that the accelerometer would provide a higher quality reference signal over the microphone and vice-versa when the majority

was transmitted via the speakers. Before testing, both the speaker and shaker levels were calibrated to create an equivalent 0.3 Vrms response signal at the stethoscope's piezo sensor. Subsequently, the relative power level was varied between the two ambient noise sources in 25% increments (e.g. 25% shaker power, 75% speaker power) while maintaining an overall constant signal-to-noise ratio. Both the desired signal sent through the thorax simulator and the ambient noise signal were 40 Hz to 2 kHz bandlimited white noise.

The correlation of each signal estimate, $\hat{s}$, to the desired signal, s, was obtained to compare the resulting performance under each testing condition. The desired signal was taken as the measurement signal from the stethoscope transducer obtained when no ambient noise was introduced. If the correlation is calculated in a sliding fashion—for the past 1000 samples at each time-step—it is possible to observe both the convergence and steady-state performance of each estimate. Accordingly, the sliding correlation at each time-step was calculated with the following equation,

$$r_{s\hat{s}}[m] = \frac{\sum_{i=0}^{1000}(s[m-i]-\bar{s}[m])(\hat{s}[m-i]-\hat{\bar{s}}[m])}{\sum_{i=0}^{1000}(s[m-i]-\bar{s}[m])^2 \sum_{i=0}^{1000}(\hat{s}[m-i]-\hat{\bar{s}}[m])^2} \tag{5.14}$$

where

$$\bar{s}[m] = \frac{1}{1000}\sum_{i=0}^{1000} s[m-i] \tag{5.15}$$

$$\hat{\bar{s}}[m] = \frac{1}{1000}\sum_{i=0}^{1000} s[m-i] \tag{5.16}$$

When the noise power is distributed evenly between the two exciters, the following behavior was observed for ANC implemented with the reference accelerometer and microphone (see Figure 5-25, Figure 5-26, and Figure 5-27).

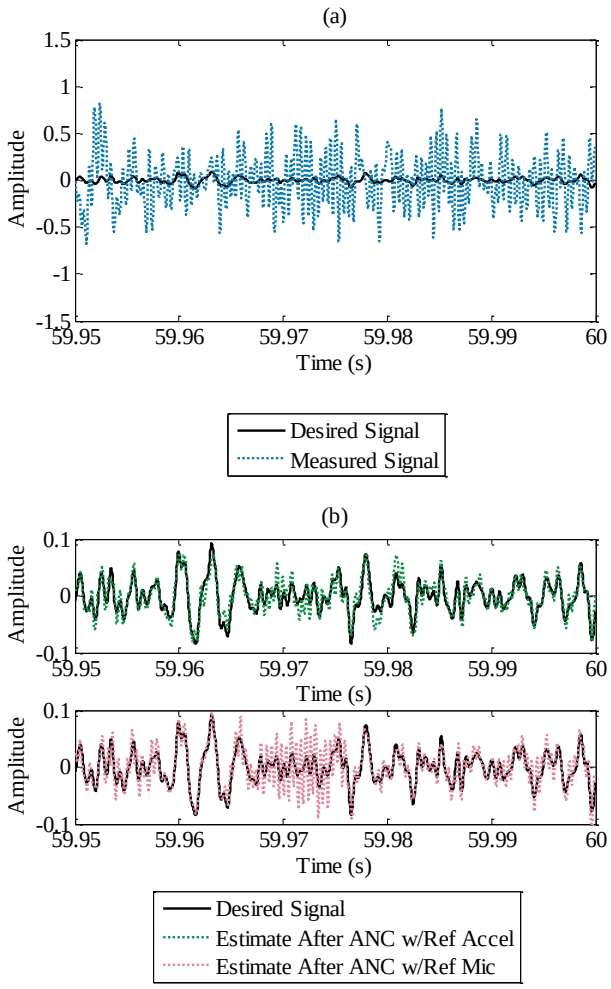

Figure 5-25: Time series data of (a) original noise corrupted measurement signal and (b) estimate of desired signal after accelerometer and microphone based ANC in bandlimited white noise environment with 50% acoustic and 50% vibration noise

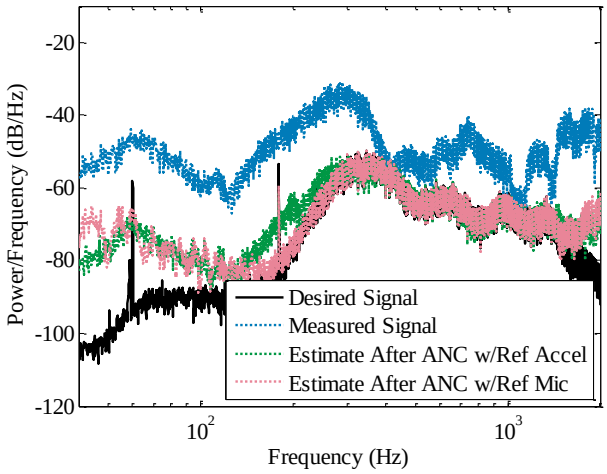

Figure 5-26: Power spectral density of signal estimates after accelerometer and microphone based ANC with 50% acoustic and 50% vibration noise

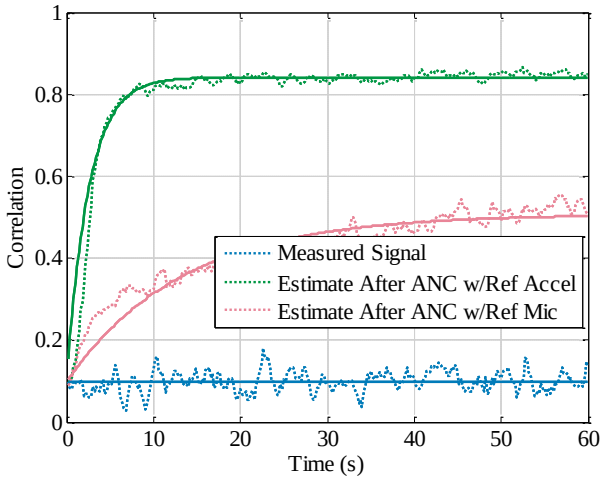

Figure 5-27: Sliding correlation raw data (dotted) and best fit line (solid) for accelerometer and microphone based ANC with 50% acoustic and 50% vibration noise

As shown in the figure of the sliding correlation (Figure 5-27), a first order exponential saturation function of the form

$$c = a\left(1 - e^{-t/\tau}\right) + c_0 \tag{5.17}$$

was fit to each data set with nonlinear least squares regression. The estimated curve makes it possible to clearly quantify the transient and steady-state performance. From the regression line, the steady-state correlation is given by the sum of the constant coefficients

$$c_{ss} = a + c_0 \tag{5.18}$$

and the approximate convergence time—time for the correlation to reach 98% of the steady-state value—is given by

$$t_{ss} = -\tau \ln(0.02) \tag{5.19}$$

For the varying ambient noise source power distributions, the steady state correlation and approximate convergence time values are provided respectively in Table 5-3 and Table 5-4.

Table 5-3: Signal estimate mean steady-state correlation to desired signal after optimal Wiener filter and active noise cancellation with LMS adaptive filter

Method	Reference Signal	Shaker Power % / Speaker Power %				
		100 / 0	75 / 25	50 / 50	25 / 75	0 / 100
Original signal (before filtering)	-	0.1016	0.1022	0.1007	0.0969	0.0867
Optimal solution from Wiener filter	Accelerometer	0.9346	0.9180	0.8865	0.7950	0.0834
	Microphone	0.0388	0.9499	0.8818	0.8118	0.7380
LMS adaptive filter (ANC)	Accelerometer	0.9114	0.8850	0.8414	0.7488	0.0928
	Microphone	0.0930	0.6109	0.5077	0.4476	0.4080

Table 5-4: Signal estimate steady-state convergence time (in seconds) after active noise cancellation with LMS adaptive filter

Reference Signal	Shaker Power % / Speaker Power %				
	100 / 0	75 / 25	50 / 50	25 / 75	0 / 100
Accelerometer	6.305	8.810	9.894	11.011	-
Microphone	-	40.592	52.421	58.459	61.888

When vibrations were the sole noise source present, it is clear that the reference accelerometer provided superior active noise cancellation performance than the microphone. After processing the data with the ANC algorithm, the accelerometer ANC

estimate had a 91% correlation with the desired signal. As the acoustic noise level was gradually increased (and vibration levels decreased), the quality of the accelerometer based active noise cancellation estimate gradually decreased. When the vibrational noise was eliminated altogether and the noise source was purely acoustic, the microphone provided a superior estimate.

An interesting trend can be observed for the case of microphone based active noise cancellation. As a larger ratio of noise was provided acoustically, it would be anticipated that the microphone based estimates would improve. However, the Wiener filter solution and ANC estimates both demonstrate the opposite trend. For the noise power ratios presented, the greatest microphone based estimate was obtained when 75% of the noise originated in the form of vibrations and only 25% originated as acoustics. In order to explain this data, further analysis was conducted. Looking at the power spectral density of the ANC estimates using the microphone reference sensor, it was discovered that the microphone based estimate fails to converge to the desired signal in the high frequency range. Specifically, in a narrow band of frequencies it appears that a large resonance dominates the estimate. Physically, this is explained by the presence of acoustic resonance within the room where testing was conducted. As noise from the speaker passes over the stethoscope, it bounces back off the walls and ceiling of the experimental room and returns to the stethoscope. This noise no longer passes first through the microphone and then to the stethoscope. Thus, the causal relationship necessary for the reference sensor is compromised. Considerable care was taken to minimize the reflection noise in the test environment, but in all real-world applications and field environments this effect may be present.

Keeping in mind this observed behavior, for tests conducted with the reference microphone, special care was taken to ensure that the microphone was positioned between the noise source and stethoscope. This guarantees that the path between this reference measurement and the noise corruption at the piezo is predominantly causal—the reference sensor measures the noise signal before it reaches the piezo. During the

course of testing, it was found that the performance of the adaptive algorithm was very sensitive to changes in this condition. In order to clearly illustrate this effect, the 100% speaker (0% shaker) test was conducted with the microphone placed at three distinct locations with reference to the speaker location: (1) ahead of the stethoscope, (2) in-line with the stethoscope, and (3) behind the stethoscope. A schematic of the microphone placement can be seen in Figure 5-28, and the resulting active noise cancellation performance is reported in Table 5-5.

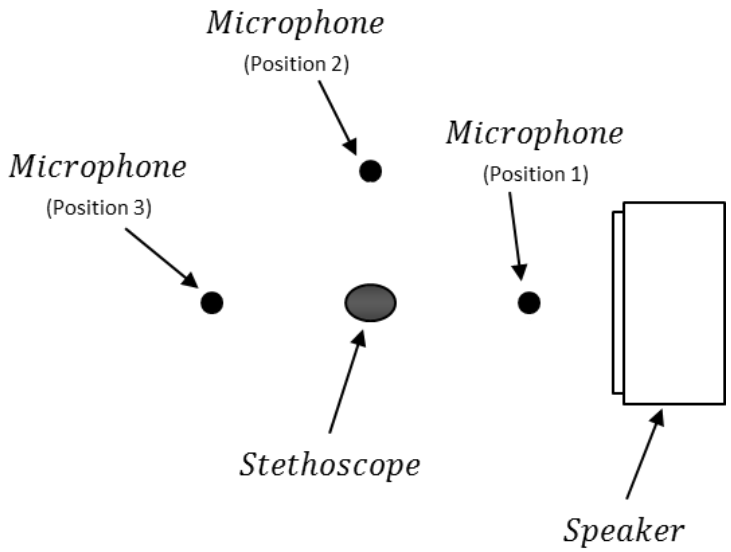

Figure 5-28: Microphone position relative to stethoscope and speaker during active noise cancellation tests

Table 5-5: Signal estimate mean steady-state correlation to desired signal and steady-state convergence time (in seconds) after active noise cancellation with LMS adaptive filter using a microphone with varying positions

Microphone Position	Steady-State Correlation	Convergence Time (s)
1: Ahead of stethoscope	0.8819	15.064
2: In-line with stethoscope	0.8572	13.486
3: Behind stethoscope	0.2867	17.737

The degradation of signal quality observed when the microphone is not positioned "upstream" from the piezo presents a difficult challenge for its use in real-world

environments. As ambient acoustic noise is commonly omnidirectional, a single reference sensor may not be adequately configured to simultaneously mitigate noise from multiple directions. In a controlled environment, the microphone can be positioned optimally to minimize contributions from the dominant noise source, but often this information is not known a priori in real world environments and the requirement for such careful set-up could create an increased burden on the user. Alternatively, it may be possible to rely on the use of a microphone array in place of a single reference sensor. Using a combination of signals from each reference, the noise from multiple sources can be eliminated. However, this can considerably increase the computational complexity of the proposed solution, and configuring a device with such reference sensors so as to avoid obstruction by the user may be difficult.

5.4.3 *Active Noise Cancellation in a Simulated Black Hawk Helicopter Environment*

Using the experimental platform, it was possible to simulate the ambient environment present in a Sikorsky UH-60 Black Hawk helicopter from field data obtained during a routine flight. The acoustic and vibration signal were taken directly from measured data in the field.

In order to guarantee a close agreement between the simulated and actual helicopter environment, the frequency content of each reference signal was calibrated with the reference accelerometer and microphone. Differences between the actual and simulated reference sensor frequency content levels were accounted for with drive signal equalization. Specifically, the frequency response of the drive signal used for the shaker and speaker were adjusted to achieve the desired output power spectral density at the reference accelerometer and microphone respectively. Shown in Figure 5-29 is a comparison of the power spectral density of signals from a UH-60 Black Hawk helicopter and the power spectral density of signals from the simulated environment.

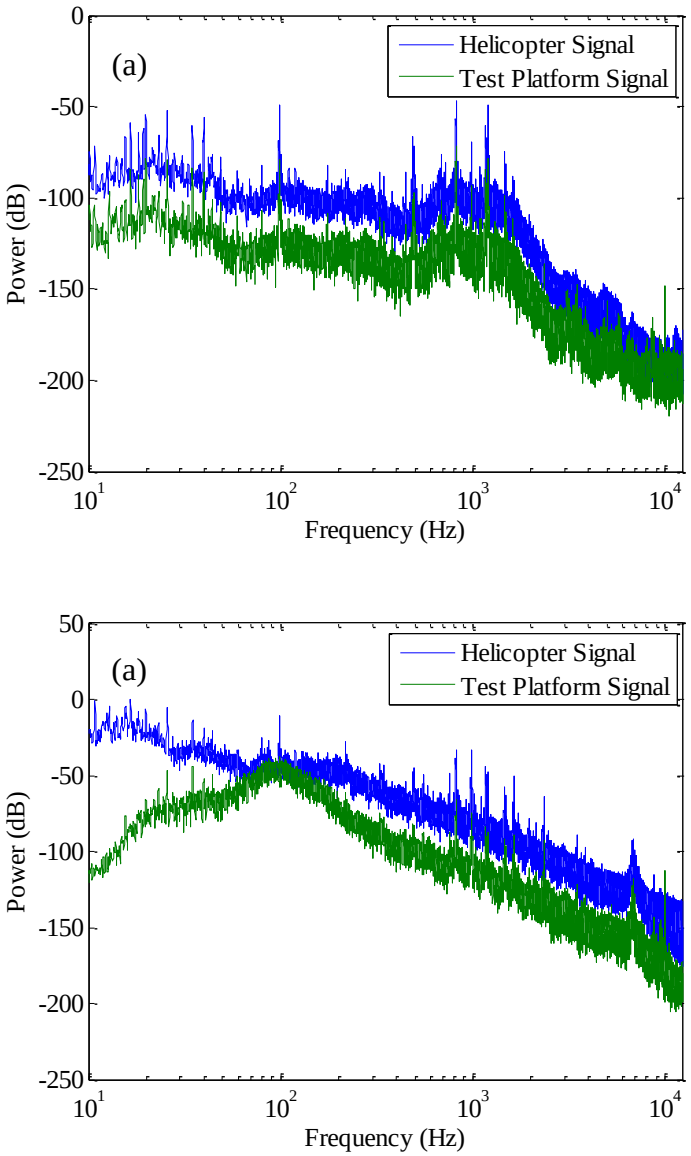

Figure 5-29: Reference (a) accelerometer and (b) microphone frequency response in a simulated UH-60 Black Hawk helicopter environment

Above approximately 200 Hz, the frequency content of both the simulated and real environment are well matched. Below 200 Hz, only the shaker is able to provide the required energy to reproduce the specified environment. The speakers provide some low frequency signal, but in general it falls below the desired ambient signals.

The overall acoustic and vibration level were calibrated to those levels experienced at the stethoscope from in-flight data. These levels correspond to the on-board sensor readings obtained from the retro-fitted electronic stethoscope used during field tests. Since some of the noise energy is dissipated or obstructed prior to reaching the stethoscope, these noise levels are lower than the pure ambient sensor readings. For the microphone data, this level is considerably reduced due to a reduced effect of wind. The ambient microphone was positioned higher in the cabin, and since the cabin windows were open during each test, a large portion of the measurements contain a significant level of noise due to localized airflow.

Calibration was also conducted on the auscultation signal sent from the thorax simulator. A clean heart sound from a healthy adult male which was recorded with the commercially available model 3200 electronic stethoscope was employed. No additional (built-in) filtering was implemented to preserve the original frequency content of the reproduced signal. However, the signal amplitude was adjusted to ensure that the rms level observed at the piezo agreed with those from field testing in the quiet environment. The resulting signal-to-noise ratio at the stethoscope transducer closely matches that obtained during in-flight auscultation.

After conducting testing in the simulated environment, the active noise cancellation algorithm was implemented in post-processing with both the reference microphone and reference accelerometer data. For initial estimates, a constant filter length of $N = 3000$ was used. The step size for each adaptation algorithm was set to 1/100th of $1/\lambda_{max}$ for the given reference sensor which was being used. This guaranteed that the filter would be stable and minimize the misadjustment level. Accordingly, the Least Mean Squares adaptive algorithm produced the following signal estimates (see Figure 5-30).

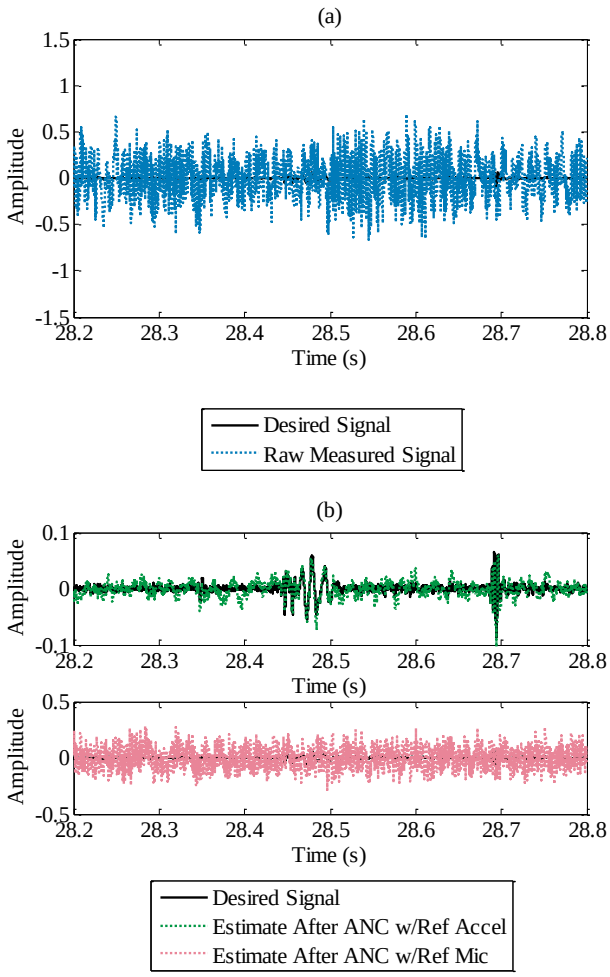

Figure 5-30: Time series data of (a) original noise corrupted measurement signal and (b) estimate of desired signal

The estimate from accelerometer based active noise cancellation can be seen to have produced a very good estimate of the desired signal. Whereas the desired signal is completely indiscernible in the raw measurements, the signal estimate after processing successfully captures all the peaks and valleys of the heart sound. Conversely, the microphone based ANC estimate still contains a high level of noise. The overall level of noise has been reduced, but the heart signal is still indistinguishable. If we look at the power spectral density of each estimate, it is possible to see the performance of each estimate in the different frequency ranges (see Figure 5-31).

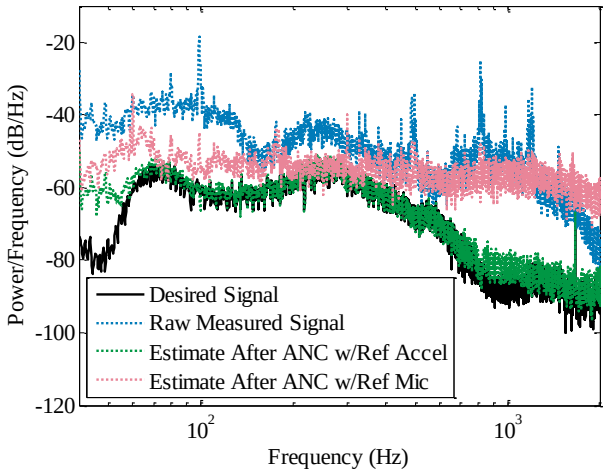

Figure 5-31: Power spectral density of signal estimates after accelerometer and microphone based ANC in a simulated UH-60 Black Hawk helicopter environment

Here, it is obvious that at all frequencies the accelerometer based active noise cancellation has outperformed the microphone based alternative. By subtracting the power spectral density of the estimated signals from the original noise contaminated signal, it is possible to examine exactly the level of noise reduction achieved at each frequency (see Figure 5-32)

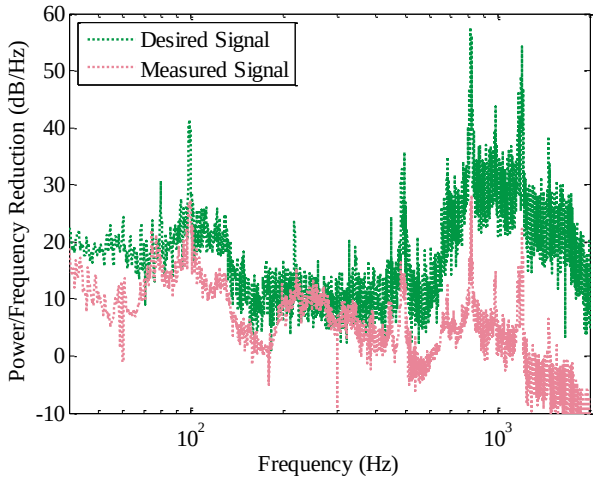

Figure 5-32: Noise reduction after accelerometer and microphone based ANC in a simulated UH-60 Black Hawk helicopter environment

The accelerometer based active noise cancellation was able to achieve 20dB reduction below 150 Hz, approximately 10 dB reduction from 150-700Hz, and nearly 30dB reduction from 700Hz-1kHz.

5.5 CONCLUSIONS

With current stethoscope technology, auscultation is not possible in most patient transportation environments due to high levels of ambient noise. In a UH-60 Sikorsky Black Hawk helicopter, the elevated noise levels are manifested in both acoustic and vibrational components. Due to the severe levels of this noise and its broadband nature, none of the current methods published in literature are adequate to enable auscultation. Previous studies have relied on the use of a reference microphone which is incapable of successfully capturing the structurally transmitted noise components. Data collected from field testing has demonstrated that a reference accelerometer, on the other hand, is much better correlated with the disturbance noise corrupting the stethoscope's signal. Thus, a reference accelerometer is better suited for active noise cancellation in this application.

Although ANC based on the accelerometer used during preliminary testing was able to achieve high levels of noise reduction over a broad frequency range, the existing design was inadequate. Additionally, these findings were limited by the quality of reference sensors employed. Based on theory and experimental data, the ideal reference accelerometer must be heavily correlated to the original noise source but must not be corrupted due to leakage of the desired signal. For this, an external accelerometer can be implemented. By placing the reference sensor away from the auscultation site, the required noise reference can be obtained without capturing the chest sounds.

Simulating the Black Hawk helicopter vibration and acoustic noise with an experimental test platform, the benefits of accelerometer based active noise cancellation have been presented. In the frequency range critical for the measurement of heart and lung sounds, the proposed system was capable of providing an estimate with approximately 94% correlation to a pure signal which would have been obtained in the absence of noise.

Whereas a microphone based system must overcome shortcomings due to acoustic resonance and an omni-directional noise field, the accelerometer reference signal has been found to have very few limitations in this regard.

By combining this active noise cancellation approach with passive acoustic shielding at the binaurals of the stethoscope, it will be possible to enable successful auscultation for the first time in such a military aircraft.

Bibliography

[1] A. Roguin, "Rene Theophile Hyacinthe Laennec (1781-1826): the man behind the stethoscope," *Clinical Medicine & Research,* vol. 4, no. 3, pp. 230-235, 2006.

[2] F. Dalmay, M. T. Antonini, P. Marquet and R. Menier, "Acoustic properties of the normal chest," *European Respiratory J.,* vol. 8, no. 10, pp. 1761-1769, 1995.

[3] S. Reichert, R. Gass, C. Brandt and E. Andres, "Analysis of respiratory sounds: State of the art," *Clinical Med.: Circulatory, Respiratory, and Pulmonary Med.,* vol. 2, pp. 45-58, 2008.

[4] H. Pasterkamp, S. S. Kraman and G. R. Wodicka, "Respiratory sounds: advances beyond the stethoscope," *Amer. J. Respir. Crit. Care Medicine,* vol. 156, no. 3, pp. 974-987, 1997.

[5] R. L. Wilkins and J. E. Hodgkin, Fundamentals of lung and heart sounds, St. Louis: Mosby, 2004.

[6] N. Gavriely, Y. Palti and G. Alroy, "Spectral characteristics of normal breath sounds," *J. Applied Physiology,* vol. 50, no. 2, pp. 307-314, 1981.

[7] N. Gavriely, M. Nissan, A.-H. E. Rubin and D. W. Cugell, "Spectral characteristics of chest wall breath sounds in normal subjects," *Thorax,* vol. 50, no. 12, pp. 1292-1300, 1995.

[8] P. Arnott, G. W. Pfeiffer and M. E. Tavel, "Spectral analysis of heart sounds: relationships between some physical characteristics and frequency spectra of first and second heart sounds in normals and hypertensives," *J. Biomedical Eng.,* vol. 6, no. 2, pp. 121-128, 1984.

[9] M. E. Tavel, Clinical phonocardiography and external pulse recording, Chicago: Year Book Medical, 1985.

[10] N. Hayashi, "Detection of pneumothorax visualized by computer analysis of bilateral respiratory sounds," *Yonago Acta Medica,* vol. 54, no. 4, pp. 75-82, 2011.

[11] M. Munakata, H. Ukita, I. Doi, Y. Ohtsuka, Y. Masaki, Y. Homma and Y. Kawakami, "Spectral and waveform characteristics of fine and coarse crackles," *Thorax,* vol. 46, no. 9, pp. 651-657, 1991.

[12] D. Callahan, J. Waugh, G. A. Mathew and W. M. Granger, "Stethoscopes: What are we hearing?," *Biomed. Instrumentation Tech.,* vol. 41, no. 4, pp. 318-323, 2007.

[13] G. Zenk, *Stethoscopic Detection of Lung Sounds in High Noise Environments,* West Lafayette, IN: Purdue University, 1994.

[14] P. Y. Ertel, M. Lawrence, R. K. Brown and A. M. Stern, "Stethoscope acoustics. II. Transmission and filtration patterns," *Circulation,* vol. 34, no. 5, pp. 899-909, 1966.

[15] C. S. Hampton and A. Chaloner, "Which stethoscope?," *British Med. J.,* vol. 4, no. 5576, pp. 388-390, 1967.

[16] L. S. Zun and L. Downey, "The effect of noise in the emergency department," *Academic Emergency Medicine,* vol. 12, no. 7, pp. 663-666, 2005.

[17] D. Groom, "The effect of background noise on cardiac auscultation," *Amer. Heart J.,* vol. 52, no. 5, pp. 781-790, 1956.

[18] L. H. Brown, J. E. Gough, D. M. Bryan-Berg and R. C. Hunt, "Assessment of breath sounds during ambulance transport," *Ann. Emergency Medicine,* vol. 29, no. 2, pp. 228-231, 1997.

[19] M. Buelow, "Noise level measurements in four Phoenix emergency departments," *J. Emergency Nursing,* vol. 27, no. 1, pp. 23-23, 2001.

[20] D. W. Johnson, R. J. Hammond and R. E. Sherman, "Hearing in an ambulance paramedic population," *Ann. Emergency Medicine,* vol. 9, no. 11, pp. 557-561, 1980.

[21] T. G. Price and G. L. Jane, "Changes in hearing acuiity in ambulance personnel," *Prehospital Emergency Care,* vol. 2, no. 4, pp. 308-311, 1998.

[22] T. B. Pasic and T. J. Poulton, "The hospital-based helicopter: a threat to hearing," *Arch. Otolaryngology,* vol. 111, no. 8, pp. 507-508, 1985.

[23] T. Harms, J. Mateer and H. Hepp, "Noise exposure for aeromedical crew members and considerations for auditory risk," *J. Air Medical Transport,* vol. 9, no. 9, p. 76, October 1990.

[24] D. C. Gasaway, "Noise levels in cockpits of aircraft during normal cruise and considerations of auditory risk," *Aviation Space Environmental Medicine,* vol. 57, no. 2, pp. 103-112, 1986.

[25] R. C. Hunt, D. M. Bryan, V. S. Brinkley, T. W. Whitley and N. H. Benson, "Inability to assess breath sounds during air medical transport," *J. Amer. Medical Assoc.,* vol. 265, no. 15, pp. 1982-1984, 1991.

[26] G. L. Zacharias, A. X. Miao, J. A. Moore, R. D. Collier and M. Asdigha, "Active noise cancellation stethoscope," Charles River Analytics, Cambridge, MA, 1993.

[27] J. P. Tourtier, E. Fontaine, S. Coste, S. Ramsang, P. Schiano, M. Viaggi, N. Libert, X. Durand, C. Chargari and M. Borne, "In flight auscultation: comparison of electronic and conventional stethoscopes," *Amer. J. Emergency Medicine,* vol. 29, no. 8, pp. 932-935, 2011.

[28] J. S. Fleeter and G. R. Wodicka, "Auscultation of heart and lung sounds in high-noise

environments using adaptive filters," *J. Acoust. Soc. Amer.,* vol. 104, no. 3, p. 1781, 1998.

[29] P. A. Cain, W. A. Ahroon and D. Greenburg, "An assessment of acoustic and electronic stethoscope performance in the UH-60 noise environment," U.S. Army Aeromedical Research Laboratory, Fort Rucker, AL, 2002.

[30] T. J. Poulton, D. W. Worthington and T. R. Pasic, "Physiologic chest sounds and helicopter engine noise," *Avaiation Space Environmental Medicine,* vol. 65, no. 4, pp. 338-340, 1994.

[31] B. Orten, "Auscultation apparatus". U.S. Patent 6512830, 28 Jan 2003.

[32] P. Nelson and S. Elliot, "Active Control of Sound," *Physics Today,* vol. 46, no. 1, p. 75, 1993.

[33] S. Kuo and D. Morgan, Active Noise Control Systems: Algorithms and DSP Implementations, New York: John Wiley & Sons, 1995.

[34] C. Fuller, S. Elliot and P. Nelson, Active Control of Vibration, San Diego: Academic, 1996.

[35] C. Hansen and S. Snyder, Active Control of Noise and Vibration, London: E&FN Spon, 1997.

[36] B. Widrow, J. R. Glover, J. M. McCool, J. Kaunitz, C. S. Williams, R. H. Hearn, J. R. Zeidler, E. Dong and R. C. Goodlin, "Adaptive noise cancelling: principles and applications," *Proc. IEEE,* vol. 63, no. 12, pp. 1692-1716, 1975.

[37] A. Suzuki, C. Sumi, K. Nakayama and M. Mori, "Real-time adaptive cancelling of ambient noise in lung sound measurements," *Medical and Biological Eng. and Comput.,* vol. 33, no. 5, pp. 704-708, 1995.

[38] S. E. Schmidt, H. Zimmermann, J. Hansen, H. Moller, D. Hammershoi and J. Struijk, "The chest is a significant collector of ambient noise in heart sound recordings," in *Comput. Cardiology,* Krakow, Poland, 2012.

[39] S. B. Patel, T. F. Callahan, M. G. Callahan, J. T. Jones, G. P. Graber, K. S. Foster, K. Glifort and G. R. Wodicak, "An adaptive noise reduction stethoscope for auscultation in high noise environments," *J. Acoustic Soc. of Amer.,* vol. 103, no. 5, pp. 2483-2491, 1998.

[40] F. Belloni, D. D. Giustina, M. Riva and M. Malcangi, "A new digital stethoscope with environmental noise cancellation," in *Proc. 12th WSEAS Int. Conf. Math. and Comput. Methods Sci. Eng.*, Stevens Point, 2010.

[41] L. Y. Wang, H. Zheng, H. Wang and G. Yin, "Multi-sensor lung sound extraction via time-shared channel identification and adaptive noise cancellation," in *Proc. IEEE Conf. on Decision and Control*, Bahamas, 2004.

[42] Z. Han, H. Wang, L. Wang and G. George, "Time-shared channel identification for adaptive noise cancellation in breath sound extraction," *J. Control. Theory Applicat.*, vol. 2, no. 3, pp. 209-221, 2004.

[43] H. Tang, T. Li and T. Qiu, "Noise and disturbance reduction for heart sounds in cycle-frequency domain based on nonlinear time scaling," *IEEE Trans. Biomed. Eng.*, vol. 57, no. 2, pp. 325-333, 2010.

[44] H. Tang, T. Li, Y. Park and T. Qiu, "Separation of heart sound signal from noise in joint cycle frequency–time–frequency domains based on fuzzy detection," *IEEE Trans. Biomed. Eng*, vol. 57, no. 10, pp. 2438-2447, 2010.

[45] G.-C. Chang and Y.-F. Lai, "Performance evaluation and enhancement of lung sound recognition system in two real noisy environments," *Comp. Methods Programs Biomed.*, vol. 97, no. 2, pp. 141-150, 2010.

[46] K. Pandia, S. Ravindran, R. Cole, G. Kovacs and L. Giovangrandi, "Motion artifact cancellation to obtain heart sounds from a single chest-worn accelerometer," in *IEEE Int. Conf. Acoust. Speech and Signal Process.*, Dallas, 2010.

[47] H. Greenberger, "Vibration isolation mount for a stethoscope chestpiece, and methods of using same". U.S. Patent 5,883,339, 16 Mar. 1999.

[48] F. A. Bilan, "Floating ballast mass active stethoscope or sound pickup device". U.S. Patent US 2009/0211838 A1, 27 Aug. 2009.

[49] R. Y. Cusson, "Resonant chamber sound pick-up". U.S. Patent 6,587,564 B1, 1 Jul. 2003.

[50] T. Drummond, H. Carim and C. Oster, "Stethoscope with frictional noise reduction". U.S. Patent 7,806,226 B2, 5 Oct. 2010.

[51] 3M, "3M Littmann Stethoscopes," 2015. [Online]. Available: http://www.littmann.com/wps/portal/3M/en_US/3M-Littmann/stethoscope/stethoscope-catalog/catalog/~/3M-Littmann-Electronic-Stethoscope-Model-Black-Tube-27-inch-3200BK27?N=5932256+4294958300&rt=d. [Accessed 11 October 2015].

[52] P. D. Welsby, G. Parry and D. Smith, "The stethoscope: some preliminary investigations," *Postgraduate Medical J.*, vol. 79, no. 923, pp. 695-698, 2003.

[53] R. L. Watrous, D. M. Grove and D. L. Bowe, "Methods and results in characterizing electronic stethoscopes," in *Computers in Cardiology*, Memphis, 2002.

[54] A. Manuel, J. Formolo and D. Penney, "Comparison of the acoustic properties of six popular stethoscopes," *J. Acoust. Soc. Amer.*, vol. 91, no. 4, pp. 2224-2228, 1992.

[55] K. Riederer, "Frequency response of stethoscopes," in *Proc. Nordic Acoust. Meeting*,

Stockholm, 1998.

[56] H. Mansy, R. Sandler, I. Royston and D. Jones, "Testing sensors for body surface vibration measurements," in *Proc. First Joint BMES/EMBS Conf.*, Atlanta, 1999.

[57] T. Royston, X. Zhang, H. Mansy and R. Sandler, "Modeling sound transmission through the pulmonary system and chest with application to diagnosis of a collapsed lung," *J. Acoust. Soc. Amer.*, vol. 111, no. 4, pp. 1931-1946, 2002.

[58] G. Wodicka, S. Kraman, G. Zenk and H. Pasterkamp, "Measurement of respiratory acoustic signals: effect of microphone air cavity depth," *Chest,* vol. 106, no. 4, pp. 1140-1144, 1994.

[59] S. S. Kraman, "Trasmission of lung sounds through light clothing," *Respiration,* vol. 75, no. 1, pp. 85-88, 2008.

[60] N. Motosh, "Determination of joint stiffness in bolted connections," *J. of Manufacturing Sci. Eng.*, vol. 98, no. 3, pp. 858-861, 1976.

[61] R. Juvinall and K. Marshek, Fundamentals of Machine Component Design, 3rd ed., New York: John Wiley & Sons, 1991, p. 184.

[62] W. Voigt, "Ueber innere Reibung fester Körper, insbesondere der Metalle," *Ann. Phys.,* vol. 283, no. 12, pp. 671-693, 1892.

[63] S. A. Prasad, Q. Gallas, S. Horowitz, B. Homeijer, B. V. Sankar, L. N. Cattafesta and M. Sheplak, "Analytical electroacoustic model of a piezoelectric composite circular plate," *AIAA J.*, vol. 44, no. 10, pp. 2311-2318, 2006.

[64] R. W. Brockett and M. D. Mesarovic, "The reproducibility of multivariable systems," *J. Math. Anal. Applicat.*, vol. 11, no. 1, pp. 548-563, 1965.

[65] M. K. Sain and J. L. Massey, "Invertibility of linear time-invariant dynamical systems," *IEEE Trans. Automat. Control,* vol. 14, no. 2, pp. 141-149, 1969.

[66] S. P. Singh, "A note on inversion of linear systems," *IEEE Trans. Automat. Control,* vol. 15, no. 4, pp. 492-493, 1970.

[67] S. P. Panda, L. M. Silverman, M. K. Sain and J. L. Massey, "Comments on "Inversion of multivariable linear systems"," *IEEE Trans. Automat. Control,* vol. 15, no. 4, pp. 489-491, 1970.

[68] A. S. Willsky, "On the invertibility of linear systems," *IEEE Trans. Automat. Control,* vol. 19, no. 3, pp. 272-274, 1974.

[69] S.-H. Wang and E. J. Davison, "A new invertibility criterion for linear multivariable systems," *IEEE Trans. Automat. Control,* vol. 18, no. 5, pp. 538-539, 1973.

[70] R. W. Brockett, "Poles, zeros, and feedback: State space interpretation," *IEEE Trans. Automat. Control,* vol. 10, no. 2, pp. 129-135, 1965.

[71] L. M. Silverman, "Properties and application of inverse systems," *IEEE Trans. Automat. Control,* vol. 13, no. 4, pp. 436-437, 1968.

[72] P. Dorato, "On the inverse of linear dynamical systems," *IEEE Trans. Syst. Sci. Cybern.,* vol. 5, no. 1, pp. 43-48, 1969.

[73] J. L. Massey and M. K. Sain, "Inverses of linear sequential circuits," *IEEE Trans. Comput.,* Vols. C-17, no. 4, pp. 330-337, 1968.

[74] P. A. Orner, "Construction of inverse systems," *IEEE Trans. Automat. Control,* vol. 17, no. 1, pp. 151-153, 1972.

[75] L. M. Silverman, "Inversion of multivariable linear systems," *IEEE Trans. Automat. Control,* vol. 14, no. 3, pp. 270-276, 1969.

[76] P. J. Moylan, "Stable inversion of linear systems," *IEEE Trans. Automat. Control,* vol. 22, no. 1, pp. 74-78, 1977.

[77] Y. Guan and M. Saif, "A novel approach to the design of unknown input observers," *IEEE Trans. Automat. Control,* vol. 36, no. 5, pp. 632-635, 1991.

[78] S.-H. Wang, E. J. Davison and P. Dorato, "Observing the states of systems with unmeasurable disturbances," *IEEE Trans. Automat. Control,* vol. 20, no. 5, pp. 716-717, 1975.

[79] P. Kudva, N. Viswanadham and A. Ramakrishna, "Observers for linear systems with unknown inputs," *IEEE Trans. Automat. Control,* vol. 25, no. 1, pp. 113-115, 1980.

[80] M. Hou and P. C. Muller, "Design of observers for linear systems with unknown inputs," *IEEE Trans. Automat. Control,* vol. 37, no. 6, pp. 871-875, 1992.

[81] S.-K. Chang, W.-T. You and P.-L. Hsu, "Design of general structured observers for linear systems with unknown inputs," *J. Franklin Institute,* vol. 334B, no. 2, pp. 213-232, 1997.

[82] M. Darouach, M. Zasadzinski and S. J. Xu, "Full-order observers for linear systems with unknown inputs," *IEEE Trans. Automat. Control,* vol. 39, no. 3, pp. 606-609, 1994.

[83] M. Corless and J. Tu, "State and input estimation for a class of uncertain systems," *Automatica,* vol. 34, no. 6, pp. 757-764, 1998.

[84] C.-S. Liu and H. Peng, "Inverse-dynamics based state and disturbance observers for linear time-invariant systems," *J. Dynamic Syst. Meas. Control,* vol. 124, no. 3, pp. 375-381, 2002.

[85] T. Floquet, C. Edwards and S. K. Spurgeon, "On sliding mode observers for systems with unknown inputs," *Int. J. Adapt. Control Signal Process.,* vol. 21, no. 8-9, pp. 638-656, 2007.

[86] F. Zhu, "State estimation and unknown input reconstruction via both reduced-order and high-order sliding mode observers," *J. Process. Control,* vol. 22, no. 1, pp. 296-302, 2012.

[87] 3M Health Care, "Brochure for 3M Littmann Model 3200," [Online]. Available: http://multimedia.3m.com/mws/mediawebserver?mwsId=SSSSSuH8gc7nZxtUnY_xNx_1evUqe17zHvTSevTSeSSSSSS--&fn=70-2010-7238-9.pdf. [Accessed 18 December 2013].

[88] 3M Health Care, "3M Littmann Electronic Stethoscope Model 3200 User Manual," [Online]. Available: http://multimedia.3m.com/mws/mediawebserver?mwsId=SSSSSufSevTsZxtUnY_Z4x_9evUqevTSevTSevTSeSSSSSS--&fn=34-8703-7468-2_EN.pdf. [Accessed 18 December 2013].

[89] U.S. Army, "U.S. Army Fact Files," [Online]. Available: http://www.army.mil/factfiles/equipment/aircraft/blackhawk.html. [Accessed 10 May 2013].

[90] Department of the Army, "Army Helicopter Internal Load Operations - Field Manual No. 55-450-2," 5 June 1992. [Online]. Available: http://usacac.army.mil/cac2/doctrine/CDM%20resources/manuals/fm/fm55_450_2.pdf. [Accessed 30 December 2013].

[91] S. Haykin, Adaptive Filter Theory, 4 ed., Prentice Call, 2002.

[92] J. Nagumo and A. Noda, "A learning method for system identification," *IEEE Trans. Automat. Control,* vol. 12, no. 3, pp. 282-287, 1967.

[93] A. Albert and L. Gardner, Stochastic Approximation and Non-Linear Regression, Cambridge: MIT Press, 1967.

[94] S. Douglas and T. Meng, "Normalized data nonlinearities for LMS adaptation," *IEEE Trans. Signal Process.,* vol. 42, no. 6, pp. 1352-1365, 1997.

[95] C. Clifford, "Coherence and time delay estimation," *Proc. IEEE,* vol. 75, no. 2, pp. 236-255, 1987.

[96] S. Kuo and D. Morgan, "Active noise control: a tutorial review," *Proc. IEEE,* vol. 87, no. 6, pp. 943-973, 1999.